A THEORETICAL INVESTIGATION OF GAS-SURFACE SCATTERING PHENOMENA VIA A SEMICLASSICAL APPROACH

By

CHARLES BRYAN SMITH

Bachelor of Science
West Texas State University
Canyon, Texas
1975

Master of Science
West Texas State University
Canyon, Texas
1978

Submitted to the Faculty of the
Graduate College of the
Oklahoma State University
in partial fullfillment of
the requirements for
the Degree of
DOCTOR OF PHILOSOPHY
December, 1984

A THEORETICAL INVESTIGATION OF GAS SURFACE SCATTERING PHENOMENA VIA A SEMICLASSICAL APPROACH

Thesis Approved:

Leonel M. Raff
Thesis Adviser

Paul N. Westhaus

George S. Weiss

J. Paul Devlin

Norman N. Durham
Dean of the Graduate College

ACKNOWLEDGEMENTS

I would like to express my thanks to the following people who served as members of my advisory committee: Drs L. M. Raff, P. A. Westhaus, J. P. Devlin, and G. S. Dixon. As Chairman, Lionel Raff was extremely helpful and patient. I would especially like to thank Paul Westhaus who was willing to discuss difficulties associated with the research problem as well as other unrelated special topics.

I sincerely appreciate financial support from the Chemistry Department and Graduate College in the form of teaching assistantship, awards, and fellowships. I would also like to acknowledge a summer fellowship from CONOCO, and the National Science Foundation for providing financial support during one year in this study through a research fellowship.

I would like to extend thanks to my friends during my stay in graduate school who provided friendship and much encouragement. In particular, my thanks go to Gary Dean, Gary Ritzhaupt, Roger and Suzie Wilson, Drs John Bowen, Mahendra Jani, Neil Purdie, Dave Martin, Hugh Richardson, and Raji Viswanathan.

TABLE OF CONTENTS

LIST OF TABLES

LIST OF FIGURES

Figure Page

CHAPTER I

HISTORICAL ASPECTS OF GAS-SURFACE SCATTERING

A. Introduction

For many years gas-solid interactions have been of interest. Since the lift and drag of objects in flight are governed by gas-solid interactions, the early interest in these interactions was stimulated by problems concerned with space flight (1,2). Many other processes are particluarly dependent upon the energy-transfer occurring in gas-solid interactions. Such processes include heterogeneous nucleation, oxidation, corrosion, vapor deposition of metals in thin films, growth of crystals at low saturation (3), sound propogation in rarefied gases (4), free molecule recovery temperatures (5), and effusion from Knudsen cells(6). Gas-solid phenomena are important in reactions involving heterogeneous catalysis. A type of gas-solid interaction has even been employed in the construction of semiconductor circuit devices via ion implantation. Surface diffusion and desorption are also areas of recent interest that are dependent upon gas surface interactions.

It is clearly important to obtain an understanding on a

microscopic level of the interaction of atoms or molecules with solid surfaces. Consequently, low-energy molecular-beam scattering by solid surfaces has become an important tool for studying properties of lattice vibrations associated with the topmost atomic layer of a solid. Indeed, study of elastic diffraction intensities has already demonstrated the power of the technique to observe structural features on clean or adsorbate-covered surfaces. Cardillo and Becker observed the the diffraction of helium atoms from a Si(100) surface (7) and a Si(111) 7x7 surface (8). Cantini, Boato, and Colella (9,10) have observed the presence of charge density waves in the diffraction pattern of helium atoms scattered at a 1T-TaS_2 surface. Rieder and Engel have investigated the diffraction of helium from a hydrogen saturated Ni(100) surface (11). Information concerning the gas-surface interaction potential can be obtained through the observation of selective adsorption resonances. Derry, Wesner, Carlos, and Frankl scattered ^{3}He and ^{4}He from graphite to obtain the binding energies of the selectively absorbed states. These results were used to determine semiempirical potential parameters (12). Boato, Cantini, Guidi, Tatarek, and Felcher studied the H-graphite and D-graphite systems and determined bound-state resonances from which an interaction potential was formulated (14). The study of the inelastic scattering of thermal atoms has suggested that surface phonons play an important role in gas-surface interactions. Horne and Miller studied the He-

LiF system and found that the interaction was dominated by single Rayleigh phonons near the specular angle (15). Brusdeylins, Doak, and Toennies, studied the same He-LiF system at lower energies and greater resolution and corroborated those results (16). Brusdeylins, Doak, and Toennies, in further studies, addressed dispersion of the phonons (17).

B. Interaction Potentials

The interaction between a gas atom and a solid surface has usually been represented by a pairwise interaction potential function between the gas atom and each atom of the solid surface. The interaction potential is most commonly an interatomic, rather than intermolecular, interaction. Interactions between polyatomic gas molecules and a surface have been developed as an expression that ignores the internal degrees of freedom of the polyatomic gas or as a superposition of the interactions of the constituent atoms of the polyatomic molecule with the atoms of the surface. So the concept of an interatomic potential is fundamental to the study of gas-surface phenomena. One must also consider the importance of the interactions between the atoms of the solid itself; these are just as important.

Relatively little is known about the precise nature of interatomic potentials, but it is possible to deduce some important information about the form of the potentials. It is known that atoms separated by "large" distances attract

one another, while atoms separated by smaller distances repel one another. One of the most common forms of interaction-potential functions is shown in Figure 1. This is the potential energy of two atoms whose centers are separated by a distance 'R'

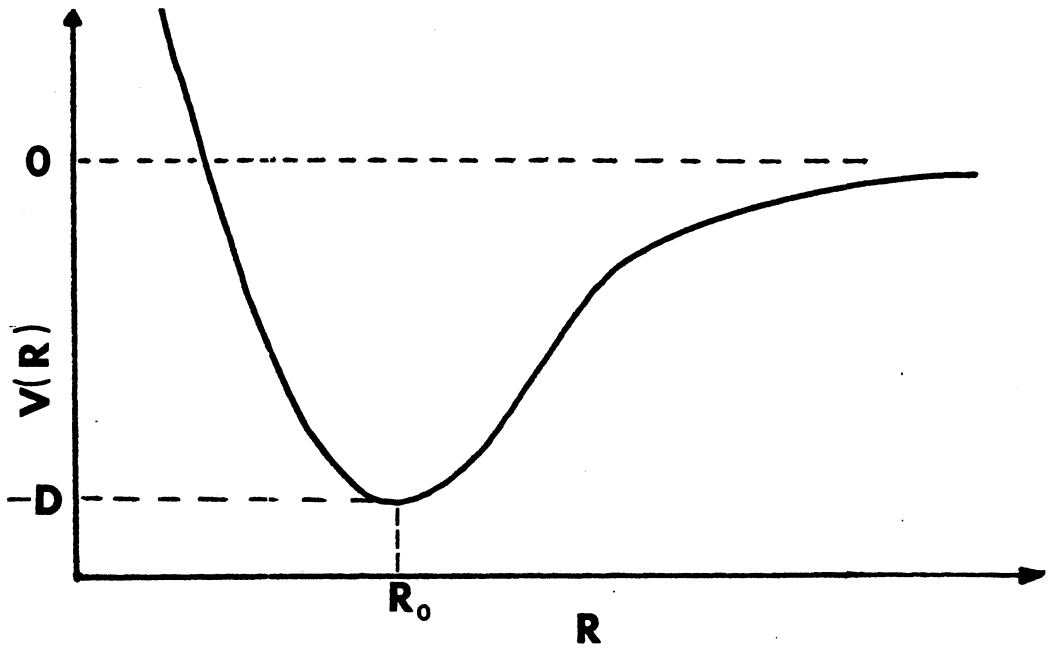

Figure.1. Typical Potential Energy Function

The longest range interaction energies between two neutral atoms are generally believed to be inverse sixth-power attractive, and can be expressed

$$V(r) = -C_6/r^6 \qquad r/r_0 >> 1 \qquad (1)$$

where C_6 is a positive constant. This is generally the leading term of an expansion of the van der Waals energy

given by

$$V(r) = -C_6/r^6 - C_8/r^8 - C_{10}/r^{10} \quad . \; . \; . \qquad (2)$$

As previously mentioned, short-range interactions give rise to repulsive potentials. These repulsive interactions can be thought of as being due to overlapping of electronic clouds. This repulsive potential can be expressed as a combination of exponential functions. At intermediate range, the Morse potential given by

$$V(r) = D\{\exp(2a(r_0-r))-2\exp(a(r_0-r))\} \;, \quad r/r_0 \cong 1, \qquad (3)$$

is believed to be adequate. This potential is most useful in the range $r/r_0 = 1$ where it gives a good correlation of experimental spectroscopic data on the vibrational energy-states of diatomic molecules. Some of the simple empirical potential functions that have found use in theoretical (18) calculations are described in the following sections.

1. Morse Potential

The Morse potential combines an exponential repulsive part with an exponential attractive part. It has the form

$$V(r) = D\{X^2 - 2X\} \qquad (4)$$

where

$$X = \exp\{a(r_0-r)\} \qquad (5)$$

This potential is particularly attractive for theorists

because the associated quantum mechanical wave functions and matrix elements are analytically expressible, and certain associated classical-mechanical equations-of-motion can be solved exactly.

2. Lennard-Jones 6-12 Potential

The Lennard-Jones potential expresses the long-range attractive contribution to the potential as an inverse sixth-power term, and retain a Morse-like form. The Lennard Jones potential has the form

$$V_{LJ}(R) / D = (R_0/R)^{12} - 2(R_0/R)^6 \qquad (6)$$

The well-depth D and the equilibrium separation R are the only adjustable parameters. Although this potential has only two adjustable parameters, it has a significant fault in that the associated quantum mechanical wave functions cannot be expressed analytically.

3. Sutherland Potential

The Sutherland potential is constructed upon the premise that the repulsive forces are so strong that they can be represented by an infinite potential wall.

$$V_S(r)/D = \infty \quad r < r_0$$

$$V_S(r) / D = -(r_0/r)^m \quad r > r_0 \; m > 0 \qquad (7)$$

The potential is shown in Figure 2. The Sutherland

potential can also be expressed in an exponential form. This is often preferable since the associated wave functions are analytically expressible.

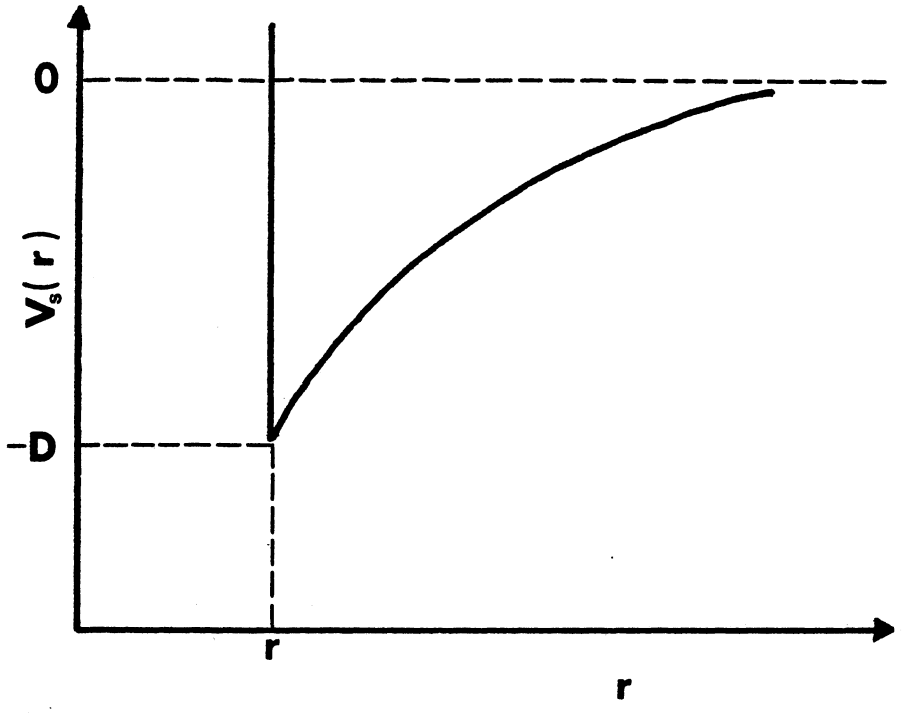

Figure 2 Sutherland Potential

4. Square-Well Potential

The Square-Well potential (Figure 3) has been found particularly useful in quantum mechanical calculations because the associated wave functions are simple sine and exponential functions. The repulsion is made infinite at r = epsilon. This is really unrealistic, but the potential

still gives useful quantum results.

$$V_{sw}(r) = \infty \qquad r < \xi$$

$$V_{sw}(r) = -D \qquad \xi < r < \zeta \tag{8}$$

$$V_{sw}(r) = 0 \qquad r > \zeta$$

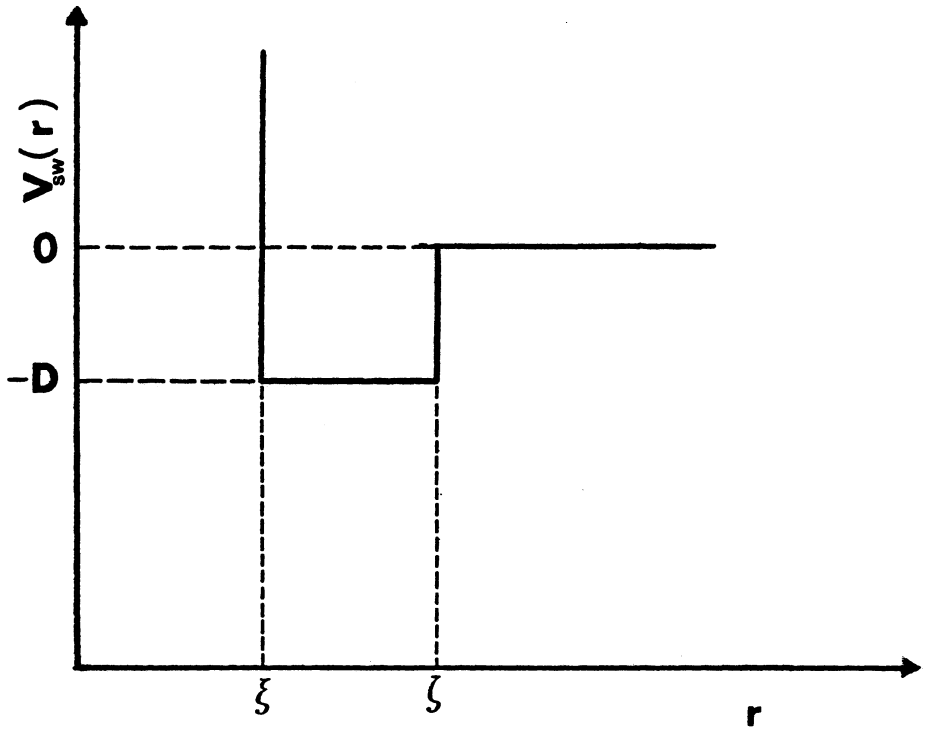

Figure 3. Square-Well Potential

5. Hard-Sphere Potential

The Hard-Sphere potential (Figure 4) is a square wave potential having zero well depth. This potential is useful in quantum mechanical calculations where bound states are unimportant.

$$V_{HS}(r) = \infty \qquad r < \xi$$

$$V_{HS}(r) = 0 \qquad r > \xi \tag{9}$$

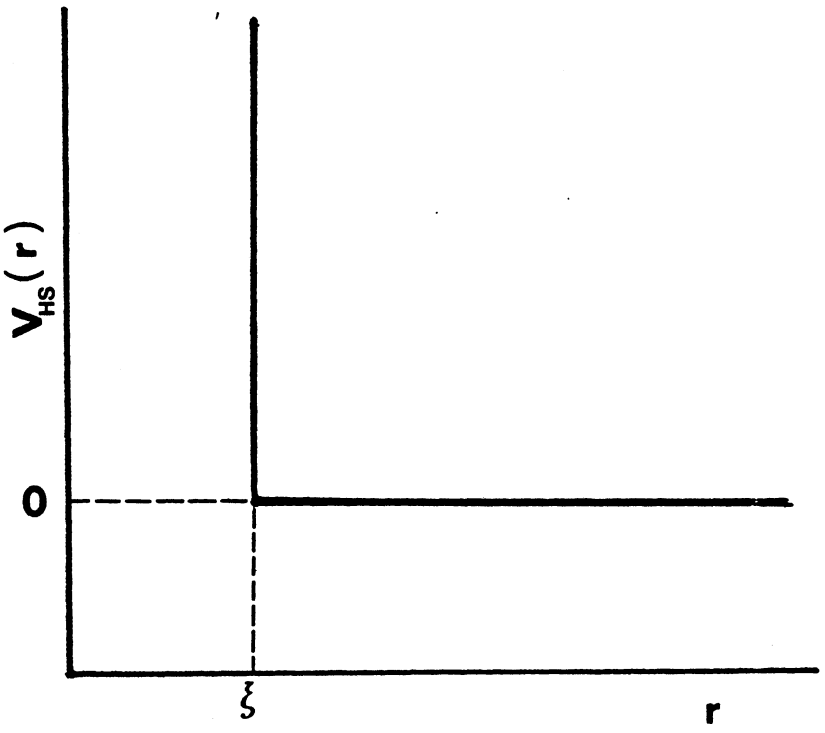

Figure 4. Hard-Sphere Potential

C. Classical Models

Modern classical theory of gas-solid interactions began with the one-dimensional lattice models of Cabrera (19) and Zwanzig (20). These were expanded to three-dimensional models by Goodman (21) and Chambers and Kinzer (22). In these theories, it was necessary to restrict the motion of the gas atom to one dimension, and to require that the atoms of the solid be initially stationary. The first successful three-dimensional classical trajectory calculations of gas atoms scattered by a solid surface were those of Oman and coworkers (23,24). They employed a Monte Carlo procedure. These early works were very important to the development of the theory; from these studies blossomed the concepts of thermal and structural scattering (25) and classical rainbow scattering (23). Unfortunately, the Monte Carlo methods had severe limitations due to their time-consuming nature and the complexity of the expressions. Logan and Stickney (26) applied a flat surface assumption in conjunction with some exact closed-form results from Goodman's one-dimensional box calculation to effect a new model. This model was the first of the "cubes" models, and was referred to as the hard-cube model. Later versions of the cube models combined a realistic variation of the gas-surface interaction normal to the surface, a nonzero surface temperature, and a characteristic vibration temperature. These were called the soft-cube models (27). The cube models were useful for correlation of large amounts of

experimental data when confined to the thermal regime, but they could not really give an acceptable description of gas-surface scattering. Recently, Adelman and Doll (28) have modified Zwanzig's one-dimensional model, combined it with the general Langevin formalism of Kubo (29) and Mori (30), and developed a generalized Langevin equation approach. The model was first used by Stelle (31) in the classical calculation of scattering of gas atoms from a crystal lattice. In this model, the interaction was described by a square-well attractive term plus a hard-wall repulsion. This was called the Corrugated Hard-Wall model.

The cube models are both applied in the thermal scattering regime. In the thermal scattering regime, the incident gas-atom energy is sufficiently small, and the radius parameter is sufficiently large, to allow the effective interaction surface to be considered relatively flat. In some theories, the interaction in the solid and the gas-surface interaction are modelled separately, but the hard-cube model is a composite of a model of the solid surface with model of a gas-surface interaction potential.

In the hard-cube models, the gas atom is treated as a rigid elastic sphere. The surface is represented by an ensemble of hard cubes having a Boltzman distribution of velocities at the surface temperature. The surfaces are flat, as the "cubes" suggests, and do not change the tangential motion of an incident gas atom. The tangential motion of the cubes can therefore be ignored. The cubes are

confined to move back and forth in a rigid "box" with constant speed. The idea is to allow the cube to move as a free particle during a collision, thereby allowing the use of the hard-sphere potential. This implies that the collision mechanics reduce to those of a one-dimensional "box-model"(32). The gas atoms are allowed one collision with one of the cubes. Therefore, only very light atoms are considered (mass of the gas atom to mass of the solid atom ratio μ is << 1). This model is very useful because it is analytically solvable and gives results that are qualitatively consistent with many experimental trends.

Two approaches have been used with the hard-cubes model. Both of these methods determine the velocity distribution for gas and surface atoms (the scattering distribution). One approach (34,35) gives the scattering distribution in closed form; the other determines it by numerical integration (26).

In the Soft-Cubes model, a stationary potential well is added, and the cube is attached to a rigid wall by a spring. The impulsive repulsion potential is replaced by an exponential repulsion. The frequency of the mass-spring system is made dependent upon the characteristic temperature of the vibration. The characteristic temperature is assumed to be that for surface vibrations. The variable parameters are the potential well-depth and the characteristic surface vibration temperature. The Soft-Cubes model therefore employs a slightly more realistic viewpoint than the Hard-

Cubes model.

In the simpler "cubes" models of gas-surface scattering, the surface is represented by an array of cubes. The cubes may be bound by springs to the substrate or regarded as free particles. In either case, the crystaline structure of the surface and that of the bulk solid are ignored. One classical model which includes a specific crystaline structure is the three-dimensional mass-spring infinite-lattice model. This treatment is an expansion of the one- and two-dimensional lattices. Generally, in lattice models, the crystal lattice has been assumed to consist of movable mass points connected to movable masses or fixed atoms by harmonic springs. An interaction potential is chosen, such as a Morse potential, to operate between the gas atom and each movable lattice atom.

In the generalized Langevin equation approach, the equations of motion for the incident gas atom and the atoms of the one-dimensional chain 'surface' are reduced to two equations of motion. The incident gas atom is considered to interact strongly with the first chain atom through a chosen interatomic potential but is not allowed to couple with the remaining portion of the chain. The atom-chain scattering is thereby reduced to a two-body collision process involving the incident atom and a simple harmonic oscillator. Adelman and Doll (36) have expanded this approach to include many-body or lattice effects. The method is restricted to consideration of scattering from harmonic lattices. Only

coordinates of the incident gas atom and the surface atoms directly struck appear explicitly. The remaining atoms of the lattice are treated as a harmonic heat bath. The effect of the heat bath upon the collision is described by a friction kernel and a Gaussian random force appearing in the generalized Langevin equation. The generalized Langevin equations are solved by employing a stochastic technique.

The developments of Adelman and Doll were closely followed by their application to the calculation of energy transfer and sticking probabilities. Such a calculation has been performed by Nitzan, Shaggard, and Tully (37). The calculations were found to be in good agreement with the quantum calculations of Lennard-Jones, Devonshire and Strachan (38). In Tully's work, the question of constructing an accurate interaction potential for a realistic system was not addressed. A simple model potential was employed to describe the interaction between gas atom and primary surface atoms.

D. Quantum Approaches

The first quantum theory of gas-surface scattering was Jackson's theory (39) of accommodation coefficients. This theory considered the one-dimensional interaction of a gas atom with an Einstein model of a solid. This work was followed by others of Zener (40,41), Jackson and Mott (42,43), and Lennard-Jones and Devonshire (44-47). These early theories have been found to be unsatisfactory due to

their basis in the first-order distorted-wave Born approximation. The gas-surface interaction has been found to be too strong to be adequately described with this approximation. Later quantum theories of Cabrera, Celli, Goodman, and Manson (48) eliminated this approximation.

The quantum theoretical methods of recent interest are those of Tsuchida (49), Wolken (50), and Cabrera, Celli, Goodman, and Manson(48). The close coupling-formulations of Wolken, and of Tsuchida, consist essentially of the numerical integration of a set of equations

$$d^2\Psi_G/dz^2 + k_{Gz}^2\Psi_G = (2M_g/\hbar^2)\sum_{G'} V_{(G-G')}\Psi_{G'} \qquad (10)$$

using the boundary conditions

$$\Psi_G(z\rightarrow\infty) = 0 : \quad G \neq F \qquad (11)$$

Here k_{Gz}^2 is the square of the normal component of the wave vector of the gas atom when the gas atom is in the state denoted by the reciprocal lattice vector G. The reciprocal lattice vectors forming the subset of G for which $k_{Gz}^2 > 0$ are denoted by F. This expression can be derived from a less imposing Schrodinger equation

$$\left[\partial^2/\partial x^2 + \partial^2/\partial y^2 + \partial^2/\partial z^2 + k_i^2 - (2M_g/\hbar^2)V(r)\right](r) = 0 \qquad (12)$$

In equation (12), $\Psi(r)$ is the wave function for the gas atom. The Cabrera, Celli, Goodman, and Manson method requires the solution of a set of integral equations derived

from its T-matrix formalism. The exact solution of the atom-surface scattering problem involves the solution and coupling of Equations (13-17):

$$t_{fi} = (f|U|s) + \sum_{\{n_{mb}\}}\sum_{K_b}\sum_{K_{bz}} (E_i - E_b)^{-1} (f|U|b)t_{bi} + \sum_{\{n_{mc}\}}\sum_{K_c} P\int dE_{cz}\,(E_i - E_c)^{-1}\,\rho_c\,(f|U|c)t - i\pi \left\{ \sum_{\{n_{mc}\}}\sum_{K_c} \rho_c (f|U|c)t_{ci} \right\}_{E_c=E_i}, \quad (13)$$

where t_{fi} is an element of the 'reduced T-matrix'. E_b represents the energy of one of the bound states, E_c represents the energy of a continuum state, and E_i is the initial energy of the state. ' P ' indicates the principal part of the integral. The $\{n_{mi}\}$'s represent the densities of the respective states. The final, specular, bound, and continuum stationary-state eigenfunctions of the gas-solid interaction Hamiltonian 'U' are represneted by f,s,b, and c respectively.

$$|T_{fi}|^2 = |\, t_{fi} + (i/2\pi\rho_s)\,\delta(f,s)\,|^2 \quad (14)$$

$$P(k_f;k_i) = (2\pi L_z M_g/\hbar^2\, k_{sz}) \sum_{\{n_{mf}\}}\sum_{\{n_{mi}\}} \rho_n((n_{mi}))\,|T_{fi}|^2\,\delta(E_f - E_i) \quad (15)$$

$P(k_f;k_i)$ is the scattering probability from an initial state k_i to a final state k_f . k_f is the magnitude of the final scattering state momentum and k_{sz} is the magnitude of the normal component of momentum of the gas atom at the surface.

$$d^2P/dE_f\,d\Omega_f = L_x L_y L_z^2\, M_g^2\, k_f/4\pi^2\,\hbar^4\, k_{sz}\ x$$

$$\sum_{\{n_{mf}\}}\sum_{\{n_{mi}\}}\rho_n(\{n_{mi}\})|T_{fi}|^2\delta(E_f - E_i). \qquad (16)$$

$$P_f = P_f(\{n_{mf}\},\{n_{mi}\}) = 4\pi^2\rho_f\,\rho_s|T_{fi}|^2 \qquad (17)$$

'P_f' represents the intensity of the scattered beam 'f'. '$P_f(\{n_{mi}\})$' is the probability denstiy function of initial phonon states.

Both the close-coupling formulation and the CCGM method are exact. The close-coupling calculations require no approximations with the exception of the specification of the gas-solid interaction potential. The coupled differential equations are solved using some numerical scheme. The CCGM method does employ a slight approximation in that a good portion of the expression derived from the T-matrix formalism is neglected (P is set equal to zero). The CCGM calculation does possess an advantage over the close-coupling method in that the close-coupling calculations require about ten times more computer time than the CCGM method.

Experimental data can be correlated with predicted values of the CCGM or close-coupling formalisms. Expressions relating the experimental scattering intensities to scattering probabilities have been derived (51). Other expressions describing the location of lobular maxima have been obtained (52) and shown to give favorable results upon use of experimental data (53). Also, the dependence of the average scalar momentum of the incident gas atom upon the scattered angle has been described (54), and compares well

with experiment.

E. Semiclassical Models

Some of the most successful gas-surface methodologies have combined classical with quantal approaches. These are referred to as semiclassical methods. In these, one portion of the problem is treated by classical means while the remaining portion is treated quantum mechanically. One of the early treatments of this type was that of Doll (55). In his work, explicit expressions for diffraction intensities were obtained from classical trajectory data. Doll applied this approach to the study of the (He-LiF) system obtaining results comparable to quantum mechanical calculations (56). Kumamoto and Silbey (57) suggested that the path of a gas atom could be determined in the usual classical trajectory manner. From the trajectory, an effective surface Hamiltonian could be derived and the time-dependent Hartree approximation applied. Masel, Merrill, and Miller used a semiclassical methodology to study Ne scattering from W(112). They were mainly interested in the affects caused by closely packed and highly periodic surfaces (58). Drolshagen and Heller (59) have employed a formulation in which the incident gas atom is represented by a superpostion of Gaussian wave packets. The wave packets were propagated along paths determined from classical trajectories. The scattering information was then obtained by projecting the final-state wave-functions onto known asymtotic states. The

wave packets were scattered from surfaces possessing particular imperfections (such as steps, corrugations, and corrugations with adsorbed atoms). Grote and Depristo (60) introduced a method in which the gas atom-to-surface distance was treated as classical variable; the remaining coordinates of the gas atom were treated quantum mechanically. The coordinates treated quantally are particularly important for determining diffraction intensities. Few of the semiclassical approaches have included consideration of surface atom motion, the studies of Raff and Agrawal (61) and Kumamoto and Silbey (57) being the exceptions. Generally, the surfaces have been assumed to be stationary with very periodic translational symmetry.

The study of gas-surface interactions has been shown to be both very active and important. As such, several reviews and texts on the subject are available (18,62-69).

The quantum mechanical procedures mentioned previously are quite involved. The somewhat simpler semiclassical approaches have achieved much success. In the model developed by Raff and Agrawal (61), an incident gas atom in the form of a quantum mechanical wave packet is scattered from a classical surface consisting of three moving lattice sites connected by harmonic springs. The motion of the wave packet is coupled to the motion of the lattice by a forced-oscillator approximation that yields a time-varying Lennard-Jones interatomic potential. Although a Lennard-Jones potential was employed, other interatomic potentials could

have been used. The time evolution of the wave packet was computed using the method of Askar and Cakmak (70), which employs the second-order difference method of Harmuth to integrate the Schrodinger equation (71).

F. Application

The purpose of this work is to expand the gas-surface scattering treatment of Agrawal and Raff (61) to a full three-dimensional consideration of lattice-atom motion and to apply the model to a real system. The treatise will consider in-plane scattering of the incident gas atoms. The solid surface will be represented by nine movable mass points which interact with to all nearest neighbor atoms by harmonic potentials. In the initial calculation, the gas atom and surface atoms will be assigned masses of one and twenty atomic mass units, respectively. It will be possible to vary the masses of the lattice atoms as well as the mass of the incident atom. This feature is desired to allow the treatment to be altered from that of a pure lattice to that of an alkalai halide salt, one possessing impurities, or a lattice with adsorbates. The positions of the moving lattice atoms will be determined in a classical fashion from Hamilton's equations of motion. The time-dependent potential employed will again be a Lennard-Jones (6,12) potential. The scattering will be treated by the time-dependent wave packet method of Askar and Cakmak (70) employing the time-dependent scheme of Harmuth (71). The

effects resulting from varying the incidence angle, incident particle velocity and mass, surface-particle mass, and crystal orientation will be calculated and compared with previous 2D results and, where possible, with experimental data. Values of the Debye-Waller factors will be determined with the expression employed by Weinberg (72) and compared with experimental and theoretical values(73).

In Chapter II, the semiclassical 3D model is formulated. In Chapter III, the results of the model applied to a simple hypothetical system are given and compared to results obtained in a previous 2D study (61) and to actual experimental data. In Chapter IV the model is employed to investigate the (He/LiF) interaction and the results are compared with experimental data and with previous theoretical results. All results are summarized and suggestions for future theoretical work in the area of gas-surface interactions are included in Chapter V.

CHAPTER II

FORMULATION

A. Introduction

In this chapter a semiclassical model for the study of interactions of a gaseous particle with a clean surface is formulated. The gas atom is taken to be a two-dimensional quantum mechanical wave packet incident upon a classical surface. The surface is assumed to be an ensemble of nine moving lattice sites set into motion from an initial (100) lattice geometry. The motion of the surface atoms is assumed to be unperturbed by the incident gaseous-atom wave packet. The final-state wavefunctions are calculated as a function of incidence angle, average incident kinetic energy, and surface temperature. The final-state wavefunction can be transformed into momentum space to obtain the velocity distribution of the scattered wave packet. The final-state wavefunctions also yield the scattered intensities as a function of scattering angle. The scattering intensities can then be determined as a function of average incident kinetic energy, incident angle, and surface temperature. Theoretically, the scattering intensities can also be obtained as a function of gaseous-atom mass, lattice-atom mass, lattice geometry, lattice

identity, and lattice purity.

Section B outlines the mathematical formulation for the determination of lattice-atom motion. Section C gives that for the propagation of the wave packet. Section D outlines the formulation for determination of the average exiting kinetic energy, the probability current density, the exiting velocity distribution, and the Debye-Waller factor.

B. Mathematical Formulation of Lattice-Atom Motion

The lattice, shown in Figure 5, is made up of nine moving lattice sites arranged in the geometry of a (100) plane. The moving lattice sites interact with all nearest neighbor sites by harmonic potentials. The moving lattice sites are assinged a mass M while the stationary sites are assumed to have infinite mass.

The orientation of the fixed sites will depend upon the surface in question. In the model, only the (100) crystal plane was considered. In Figure 5, the movable lattice sites are represented by the large open circles while the large and small darkened circles represent fixed sites in and below the x-y plane, respectively. It can be readily seen that the (100) plane possesses 60 pairwise harmonic potentials. The total potential for the lattice will be assumed to be the sum of these 60 pairwise interactions.

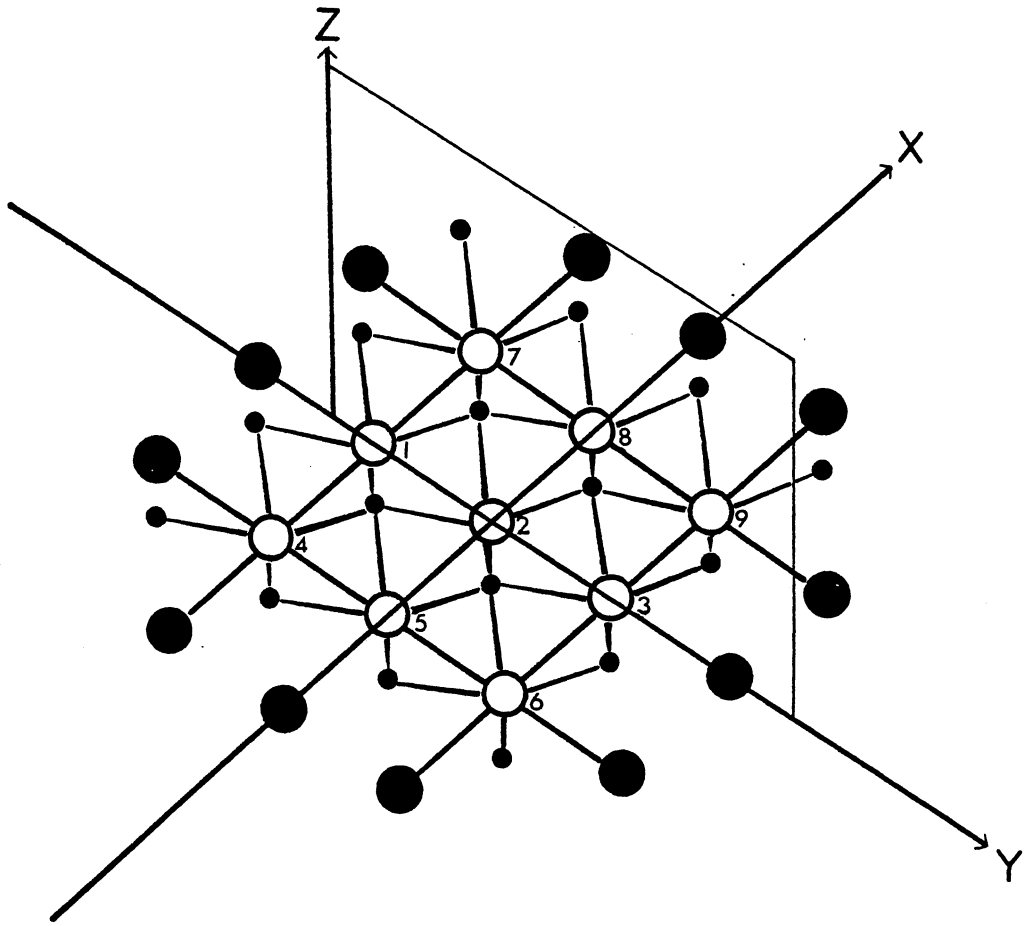

Figure 5. Model Atomic Arrangement

$$V_{lattice} = V_{(y,z)} = \sum_{i=1}^{60} V_i^H \quad , \tag{18}$$

where

$$V_i^H = (k/2)(R_i - Re)^2 \quad . \tag{19}$$

R_i represents the interparticle distance in the harmonic pair potential indicated as V_i^H, Re is the equilibrium lattice spacing, and k is the lattice force constant. The lattice motion is then determined from Hamilton's equations:

$$\partial H/\partial P_{xi} = P_{xi}/M_i = \dot{X}_i \, , \tag{20}$$

$$\partial H/\partial P_{yi} = P_{yi}/M_i = \dot{Y}_i \, , \tag{21}$$

$$\partial H/\partial P_{zi} = P_{zi}/M_i = \dot{Z}_i \, , \tag{22}$$

$$\partial V/\partial X_i = -\dot{P}_{xi} \, , \tag{23}$$

$$\partial V/\partial Y_i = -\dot{P}_{yi} \, , \tag{24}$$

$$\partial V/\partial Z_i = -\dot{P}_{zi} \, , \tag{25}$$

for i = 1,2,3, . . .,9.

The 3D Hamiltonian has the form:

$$H = 1/2 \sum_i \{ P_{xi}^2 + P_{yi}^2 + P_{zi}^2 \}/M_i + V_{lattice} \, . \tag{26}$$

The motion of the lattice sites is determined by solving the 54 coupled differential equations given in (20-25). In order to solve these equations, all of the initial positions and momenta must be specified. The

initial lattice positions are given by:

$$X_1 = X_2 = X_3 = 0 , \tag{27}$$

$$X_4 = X_5 = X_6 = -Re , \tag{28}$$

$$X_7 = X_8 = X_9 = Re , \tag{29}$$

$$Y_8 = Y_2 = Y_5 = 0 , \tag{30}$$

$$Y_9 = Y_3 = Y_6 = Re , \tag{31}$$

$$Y_7 = Y_1 = Y_4 = -Re , \tag{32}$$

$$Z = 0 \text{ for } i=1,2,3, \ldots .9 . \tag{33}$$

The initial lattice momenta selection is performed as follows:

$$P_{xi} = \{2M_i k_b T_S\} \quad (-1)^{r_j} , \tag{34}$$

$$P_{yi} = \{2M_i k_b T_S\} \quad (-1)^{r_j'} , \tag{35}$$

$$P_{zi} = \{2M_i k_b T_S\} \quad (-1)^{r_j''} , \tag{36}$$

for $i=1,2,3, \ldots 9$.

k_b is Boltzman's constant, T_S is the surface temperature and r_j , r_j' , and r_j'' are random integers uniform on the interval (0,1). The initial position coordinates place the lattice atoms at their equilibrium positions so that all the energy is kinetic. The initial momenta equipartition the lattice energy, $3k_bT_S$, into the three available momentum components of each moving lattice atom.

A fourth order Runge-Kutta method with minimum error bounds was chosen to solve the system of differential equations (74). For a dependent variable specified by y at time t and y at the previous time step $t-h$, h being the integration step size, the necessary iterative equations are:

$$y = y + 0.17476028k - 0.55148066k + 1.20553560k + 0.11718478k \quad . \tag{37}$$

If the expression for y is $y = f(t,y)$, then the expressions for the k are:

$$k = hf(t , y) \quad , \tag{38}$$

$$k = hf(t + 0.4h, y + 0.4k) \quad , \tag{39}$$

$$k = hf(t + 0.45573725h, y + 0.29697761k + 0.15875964k) \quad , \tag{40}$$

and

$$k = hf(t + h, y + 0.21810040k - 3.05096516k + 3.83286476k) \, . \tag{41}$$

The integration step size was determined by the step-size necessary for accurate propagation of the gas atom-wave packet and will be discussed in Section C.

C. Mathematical Formulation of Wave Packet Propagation

The incident atomic beam is represented by a wave

packet $\Psi(y,z,t)$ that moves along the plane formed by the surface normal and the incident velocity vector. This is taken to be the (y-z) plane. The wave packet is evolved through the time-varying potential set up by the moving lattice sites by employing the explicit integration method of Harmuth (71) as expanded to two dimensions by Askar and Cakmak (70). In this procedure, the wave function moves through time subject to the Schrodinger equation:

$$H\Psi(y,z,t) = i\hbar\, \partial\Psi(y,z,t)/\partial t \quad . \qquad (42)$$

The behavior of $\Psi(y,z,t)$ can be approximated by

$$\Psi^{n\pm1}_{(y,z)} = \exp(\mp i\,\Delta t H/\hbar)\,\Psi^{n}_{(y,z)} \quad , \qquad (43)$$

where Δt represents the time increment used to evolve the wave packet from t = nΔt to t = (n+1)Δt and so on. The Hamiltonian is given by

$$H = -(\hbar^2/2m)\{\partial^2/\partial y^2 + \partial^2/\partial z^2\} + V(z,y,Q) \quad . \qquad (44)$$

The interaction potential at a point (y,z) is dependent upon the instantaneous positions of all of the lattice atoms. These positions are represented by 'Q' in Eq. (44). 1 (y,z,t) is computed over a rectangular grid in (z,y) space. The total interaction potential at a point (y,z) on the grid of potential values due to the i-th lattice atom is assumed to have the form

$$V(y,z,Q) = \sum_i V_i \quad (y,z,X_i^L, Y_i^L, Z_i^L) \qquad (45)$$

for i = 1,2,3, . . . 9. V_i is assumed to be the Lennard-

Jones (6,12) potential given by

$$V_i = 4\epsilon\{(\sigma/r)^{12} - 2(\sigma/r)^{6}\} \quad , \qquad (46)$$

where ϵ and σ represent the potential well depth and the equilibrium distance between the gaseous atom and a given lattice atom respectively. In Equation (43) the exponential can be expanded in a Taylor series giving

$$\exp(-i\Delta tH/\hbar) = 1 - i\Delta tH/\hbar + \ldots \qquad (47)$$

Truncation of the series after the first two terms gives

$$\exp(-i\Delta tH/\hbar) = 1 - i\Delta tH/\hbar \quad . \qquad (48)$$

Substitution of (48) into (43) yields

$$\Psi_{[j,k]}^{n+1} = \{1 - i\Delta tH/\hbar\}\,\Psi_{[j,k]}^{n} \quad , \qquad (49)$$

where

$$\Psi_{[j,k]}^{n} = \Psi(y_j, z_k, t_n) \quad , \qquad (50)$$

and $\Psi_{[j,k]}$ denotes the value of $\Psi(y,z,t_n)$ at a grid point (j,k) and time t . Substitution of (43) into (44) gives

$$\Psi_{[j,k]}^{n+1} = \{1 - (i\Delta t/\hbar)(-\hbar^2/2m(\partial^2/\partial y^2 + \partial^2/\partial z^2) + V)\}\,\Psi_{[j,k]}^{n} \quad . \qquad (51)$$

The second-order derivatives can be approximated by

$$\partial^2\Psi/\partial z^2 = (\Psi_{j+1,k} + \Psi_{j-1\,k} - 2\Psi_{j,k})/\Delta z^2 \quad , \qquad (52)$$

and

$$\partial^2\Psi / \partial y^2 = (\Psi_{j+1,k} + \Psi_{j-1,k} - 2\Psi_{j,k})/\Delta y^2 , \quad (53)$$

where z and y are the grid spacings along the z and y directions, respectively. Substitution of (52) and (53) into (51) and rearrangement yields

$$\Psi_{j,k} = \Psi_{j,k} - 2i \{ [2(\alpha_1 + \alpha_2) + V_{j,k} t/\hbar] \Psi_{j,k} - \alpha_1(\Psi_{j+1,k} + \Psi_{j-1,k}) - \alpha_2(\Psi_{j,k+1} + \Psi_{j,k-1}) \} , \quad (54)$$

where

$$\alpha_1 = \Delta t\hbar/2m(\Delta y)^2 , \quad (55)$$

and

$$\alpha_2 = \Delta t\hbar/2m(\Delta z)^2 . \quad (56)$$

The initial wave packet $\Psi(y,z,0)$ was chosen so that its Fourier transform yielded a momentum distribution that approximates that present in an actual atomic beam. For the case of an atomic hydrogen beam incident upon a 3D surface at an angle θ_i and lying in the plane formed by the incident velocity vector and the surface normal, the initial wave packet is given by

$$\Psi(y,z,0) = \Psi(y,z) = G(q_1)F(q_2), \quad (57)$$

where

$$q_1 = z \cos\theta_i + y \sin\theta_i , \quad (58)$$

and

$$q_2 = y \cos\theta_i + z \sin\theta_i \,, \tag{59}$$

with

$$Z = z - z_0 \text{ and } Y = y - y_0 \tag{60}$$

where (z_0, y_0) are the coordinates of atom 2 in the surface (See Figure 5).

D. Mathematical Formulation of the Final Average Kinetic Energy, Momentum Distribution, Current Density, and Debye-Waller Factor

1. Final Average Kinetic Energy

From the final scattered wave packet $\Psi(y,z,\infty)$, all information desired can be derived. The average exiting kinetic energy ,$\langle E_e \rangle$, can be obtained from

$$\langle E_e \rangle = \iint \Psi^*(y,z,\infty) \{(-\hbar^2/2m(\partial^2/\partial y^2 + \partial^2/\partial z^2))\} \Psi(y,z,\infty)\, dydz. \tag{61}$$

As in Section C, the second derivatives of the wave function or its complex conjugate are approximated with second difference methods; the integrals are evaluated using Simpson's rule integration.

2. Energy Distribution

The scattered wave packet data beyond the range of the lattice potential is used to obtain the energy distribution. In this region the total energy is kinetic. The energy

distribution data can be obtained from the Fourier transform of $\Psi(y,z,\infty)$, as was described in Section C. The momentum distribution, $\Theta(k_z,k_y)$, is given by:

$$\Theta(k_z,k_y) = (2\pi)^{-1/2}\int_Y\int_Z \exp\{-i(k_z z+k_y y)\}\ \Psi(z,y)dzdy. \quad (62)$$

Separation of this expression into real and imaginary portions gives

$$\Theta_R(k_z,k_y) = (2\pi)^{-1}\int_Y\int_Z \{\ \Psi_R(z,y)\cos(k_z z+k_y y) + \Psi_I(z,y)\sin(k_z z+k_y y)\}dzdy\ , \quad (63)$$

and

$$\Theta_I(k_z,k_y) = (2\pi)^{-1}\int_Y\int_Z \{\ \Psi_I(z,y)\cos(k_z z+k_y y) - \Psi_R \sin(k_z z +k_y y)\}dzdy\ . \quad (64)$$

The probability that the z component of momentum lies in the range $\hbar k_z \leq P_z \leq (k_z+dk_z)\hbar$ while the y component of the momentum lies in the range $\hbar k_y \leq P_y \leq (k_y+dk_y)\hbar$ is equal to $/\theta(k_z,k_y)/^2\ dk_z dk_y$. Transforming the momentum distribution,

$$P(k)dk = \int_{\Theta_k:0}^{\Theta_k:2\pi} /\theta(k,\Theta_k)/^2 k dk d\Theta_k, \quad (65a)$$

to a distribution of energies, we have

$$P(E_k)dE_k = h^{3/2}m\int_{\Theta_k:0}^{\Theta_k:2\pi} /\theta(E_k,\Theta_k)/^2 dE_k d\Theta_k, \quad (65b)$$

where $P(E_k)dE_k$ is the probability that the energy lies in the range $E_k \leq E \leq E_k+dE_k$, with

$$E_k = \hbar^2 k^2 /2m\ , \quad (66)$$

$$\Theta(k,\theta_k) = \Theta(k_Z, k_Y) \quad , \tag{67}$$

$$k = \{k_Z^2 + k_Y^2\}^{1/2} \quad , \tag{68}$$

and

$$\Theta_k = \tan^{-1} \{k_Y/k_Z\} \quad . \tag{69}$$

3. Current Density

The probability current density is given by

$$\bar{S} = (\hbar/2mi)\{\Psi^* \bar{\nabla} \Psi - (\bar{\nabla} \Psi^*)\Psi\} \tag{70}$$

The components of S are:

$$S_Z = (\hbar/m)\{\Psi_R \partial\Psi_I/\partial z - \Psi_I \partial\Psi_R/\partial z\} \quad , \tag{71}$$

and

$$S_Y = (\hbar/m)\{\Psi_R \partial\Psi_I/\partial y - \Psi_I \partial\Psi_R/\partial y\} \quad . \tag{72}$$

The angular distribution of the scattered wave packet can then be determined via

$$\Theta_i = \Theta_{\text{scattered}} = \tan^{-1} (S_Z/S_Y) \tag{73}$$

The intensity over a particular interval $(\theta_i - \theta^*)$ is given by

$$I(\theta_j) = \sum_i (\Psi^* \Psi)_i \, P(\theta_j) \quad , \tag{74}$$

where the summation runs over all lattice points on the integration grid and $P(\theta_j) = 1$ if θ_i obtained from Eq. (73) lies in the range $\theta_j < \theta_i < \theta_j + \Delta\theta$ and $P(\theta_j) = 0$

otherwise. Resolution to $\Delta\Theta$ values of less than 5^{o} brought about spurrious results. Examples of the data produced are given in Chapter III.

4. Debye-Waller Factor

The Debye-Waller Factor was calculated employing, with slight variation, equation (1) from Weinberg's paper on helium scattering form solid surfaces (72). There, the Debye-Waller factor is defined to be:

$$DWF = \exp\{-Q_{\perp}^{2} \langle u_{\perp}^{2} \rangle / \hbar^{2}\} \ . \qquad (75)$$

In Eq. (75), '$Q_{\perp}$' is defined as the momentum transfer of the scattered atom orthogonal to the surface. $\langle u^{2}_{\perp} \rangle$ is the mean square displacement of the surface atoms orthogonal to the surface plane. The expression employed in the present work has a slightly different, but totally analogous form:

$$DWF = \exp\{-\langle Q^{2}_{\perp} \rangle \langle u^{2}_{\perp} \rangle / \hbar^{2} \} \ . \qquad (76)$$

Here, $\langle Q^{2}_{\perp} \rangle$ is the average square momentum transfered from the scattered wave packet in a direction perpendicular to the surface. This direction in the proposed model is the z-direction. $\langle Q^{2}_{\perp} \rangle$ is then expressed as:

$$\langle Q^{2}_{\perp} \rangle = \{ \langle p^{2}_{z} \rangle^{1/2}_{t:\infty} - \langle p^{2}_{z} \rangle^{1/2}_{t:0} \}^{2} \ , \qquad (77)$$

where $\langle p^{2} \rangle_{t:0}$ is the negative of the average square momentum component in the z direction of the initial wave packet and $\langle p^{2} \rangle_{t:\infty}$ is the average square momentum component

in the z direction of the scattered wave packet. $\langle p_z^2 \rangle_{t:\infty}$ and $\langle p_z^2 \rangle_{t:0}$ are obtained from

$$\langle p^2_z \rangle_{t:0} = \iint \Psi^*(y,z,0)\{(\hbar/i)^2 (\partial/\partial z)^2\} \Psi(y,z,0)\, dzdy \ , \quad (78)$$

and

$$\langle p^2_z \rangle_{t:\infty} = \iint \Psi^*(y,z,\infty)\{(\hbar/i)^2 (\partial/\partial z)^2\} \Psi(y,z,\infty)\, dzdy \ . \quad (79)$$

The direction of $p_{z\,t:0}$ is opposite that of $p_{z\,t:\infty}$ and therefore, the respective signs will also be opposite. This causes the terms in Equation (77) to be additive. Here again, the second derivatives can be evaluated by second difference methods and the integrals obtained using Simpson's Rule.

CHAPTER III

MODEL

A. Introduction

In this chapter, the specifics of the 3D model and results obtained will be presented. Initially, a short description of the particulars of the gas-surface interaction potential, the wave packet chosen, and the results obtained are given. The results are then compared with those obtained from the two-dimensional work of Raff and Agrawal (61), with the results of other theoretical models, and with experimental data. The effects of surface temperature upon the final-state wave function and average energy transfer is discussed. The effects of surface temperature, average incident energy, and incident angle upon the final-state energy and momentum distributions, the current density, and Debye-Waller factor are then addressed. An energy accommodation coefficient is determined and its behavior with incident energy and surface temperature is described.

B. Potential

As described in Chapter III, Equation 46 gives the Lennard-Jones (6,12) potential chosen for use in the model

calculation. The gas and lattice atoms are assigned masses of 1.008 and 20.18 amu, respectively. The σ and ϵ parameters employed in the LJ(6,12) potential are estimated using the combination rule given by

$$\epsilon_{H\text{-}Ne} = (\epsilon_H * \epsilon_{Ne}) \tag{80}$$

and

$$\sigma_{H\text{-}Ne} = (1/2)(\sigma_H + \sigma_{Ne}) \tag{81}$$

The Lennard-Jones parameters are given in Table I (75).

TABLE I

LENNARD-JONES PARAMETERS

Molecule or Atom	σ(Å)	ϵ/k (K)
H	2.708	37.0
Ne	2.764	40.2

The resultant Lennard-Jones parameters are σ = 2.74 A and ϵ/k = 38.5 K. The initial interaction potential, in the yz plane, is shown in Figure 6.

C. Model Wave Packet

The wave packet chosen for the model calculation is given by

$$G(q_1) = \exp(-ik_0 q_1)\sin(q_1 - q_1^0)\,\Delta k \;/(q_1 - q_0)(\pi \Delta k)^{1/2}. \tag{82}$$

$F(q_2)$ was chosen to be

$$F(q_2) = \begin{cases} (2\varepsilon)^{-1/2}, & \text{for}(-a \le q_2 \le a), \\ 0, & \text{for } q_2 > a \text{ or } q_2 < -a, \end{cases} \tag{83}$$

where

$$a = \{Re / 2.0 + \Delta y\}\cos\theta_i . \tag{84}$$

Here, Re is the equilibrium lattice spacing.

The Fourier transform of $G(q)$ is

$$g(k) = \begin{cases} \exp(ikq_1^0)/(2\Delta k)^{1/2}, & \text{for}(k_0 - \Delta k) \le k \le (k_0 + \Delta k) \\ 0, & \text{for } k > (k_0 + \Delta k), \text{ or } k < (k_0 - \Delta k). \end{cases} \tag{85}$$

From Equation (85) it is seen that $G(q_1)$ has a square distribution in momentum space. $F(q_2)$ is a square wave packet in q_2 space with a width of 2a. The initial wave

packet therefore corresponds to a classical trajectory case of a gaseous atom impinging upon the surface with an equal probability that the aiming points lie along a line in the (y,z) plane, a distance Re/2 on either side of atom 2 in Figure 5. Figure 7 shows the configuration space over which $\psi(y,z,t)$ is evolved. This is a 12 x 26 Å grid in (y,z) space. An equispaced mesh of grid points with $\Delta z = \Delta y =$ 0.2 Å is employed with $\Delta t = 4 \times 10^{-16}$ sec. Outside this configuration space, the potential is assumed to be infinite. The size of this space was found to be adequate except for incident angles of 60° when portions of the scattered probability density reached the edges of the grid long before the majority of the interaction had taken place. The initial location of the wave packet is taken to be $q_1^o =$ 8Å. This distance is large enough to place a majority of the initial wave packet outside the range of the gas-surface interaction potential. Integrated probabilities are determined at intervals of 25 time steps yielding an average probability of 1.0174. The integration scheme for the model case is therfore believed stable and accurate due to the consevation of probability. Perspective plots showing the initial- and final-state probability densities for normal incidence and T_S = 1500 K are shown in Figures 8 and 9. Figures 10 and 11 show the initial and final-state probability densities for 30° incidence, and Figures 12 and 13 show the same for 45° incidence. Figure 14 shows the level curves of the initial probability density for normal

incidence and T_s = 1500 K. Figure 15 shows the level curves of the final-state probability density. The presence of centers of high probability density is very evident.

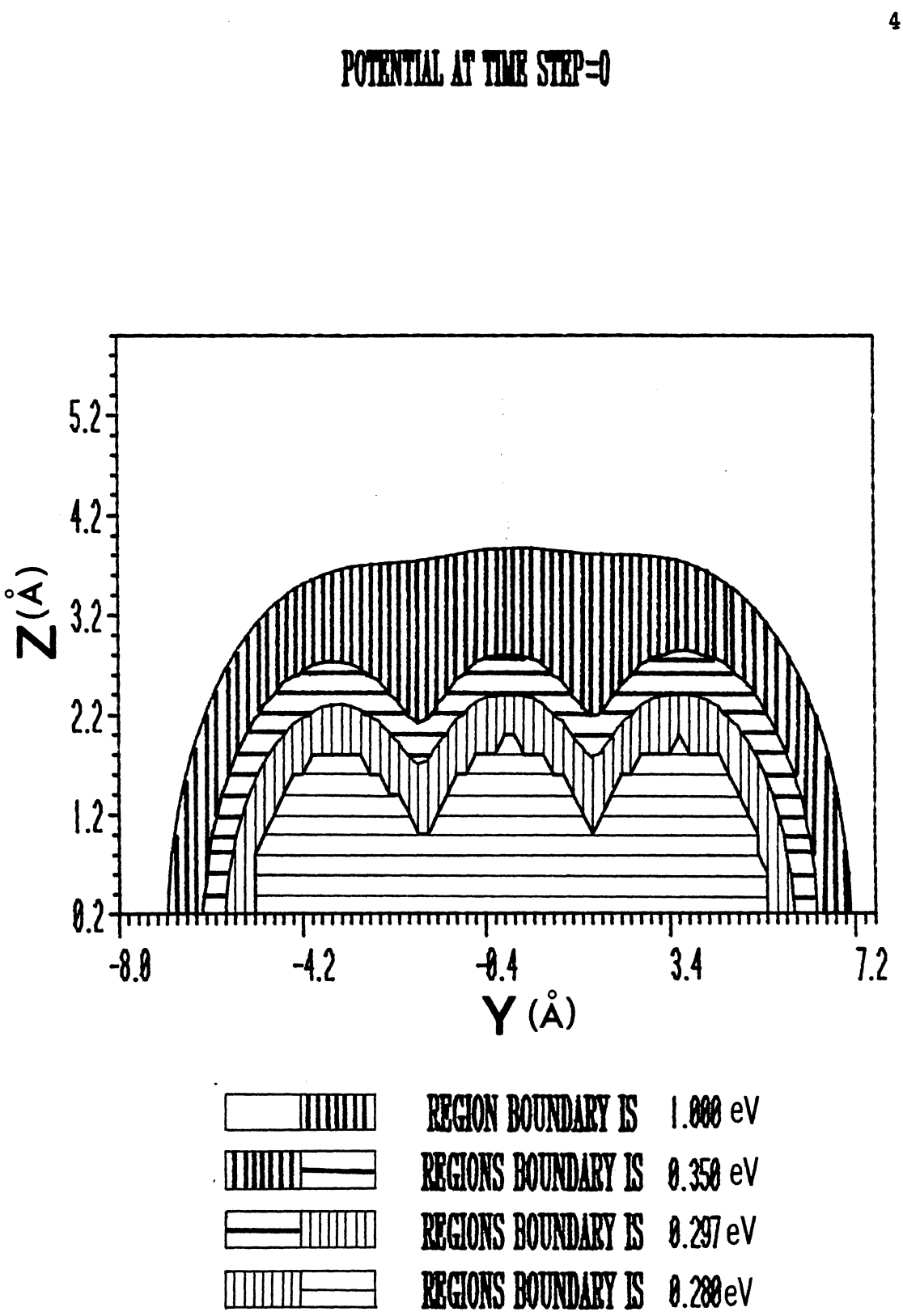

Figure 6. Model Potential

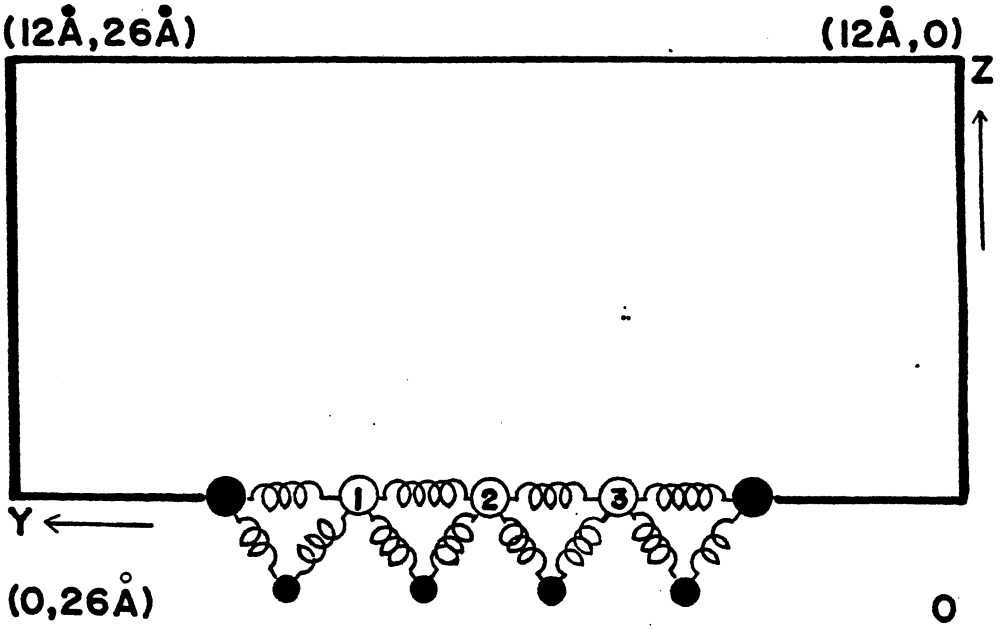

Figure 7. Configuration Space for $\Psi(y,z,t)$

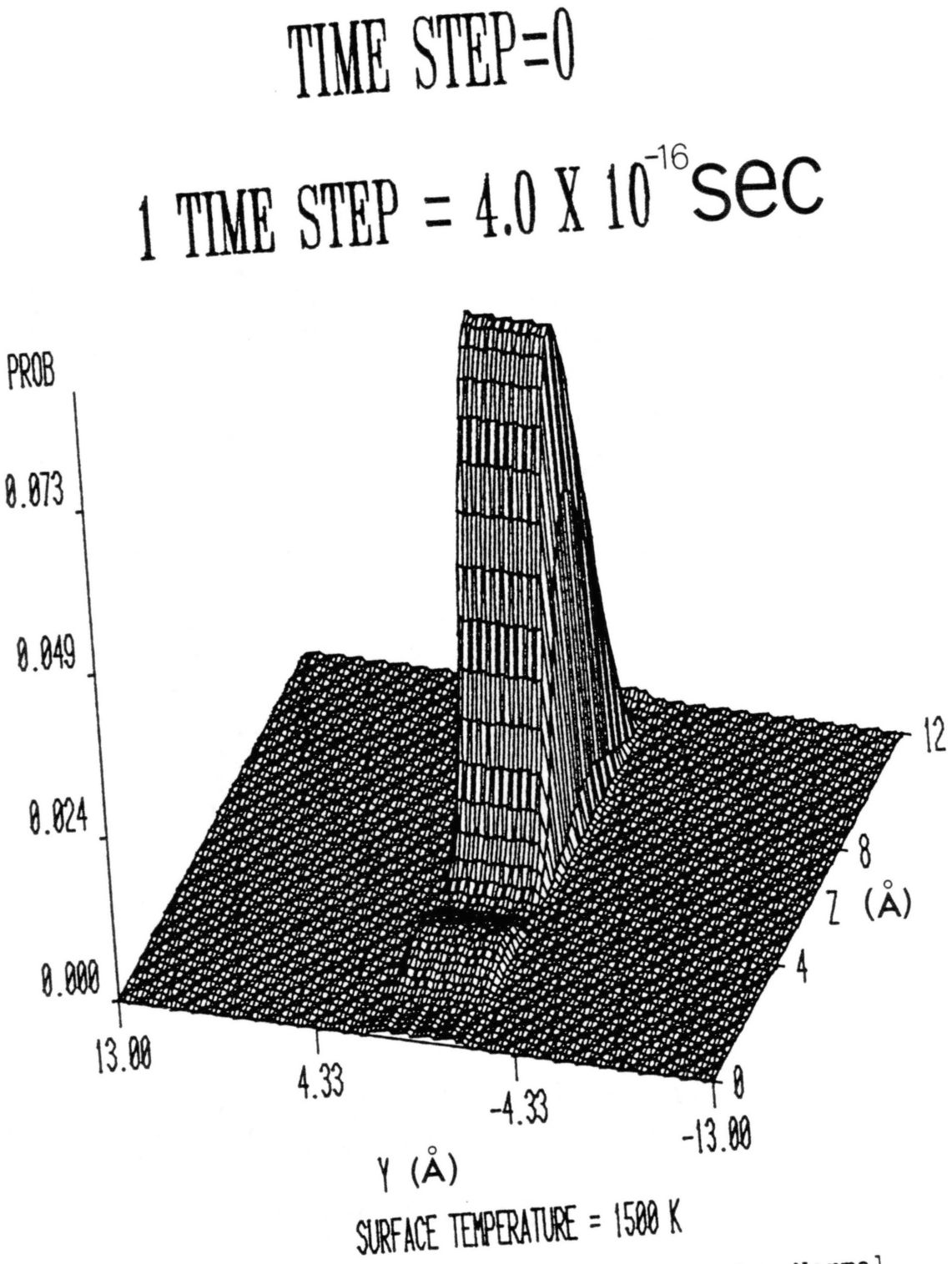

Figure 8. Initial Probability Density for Normal Incidence

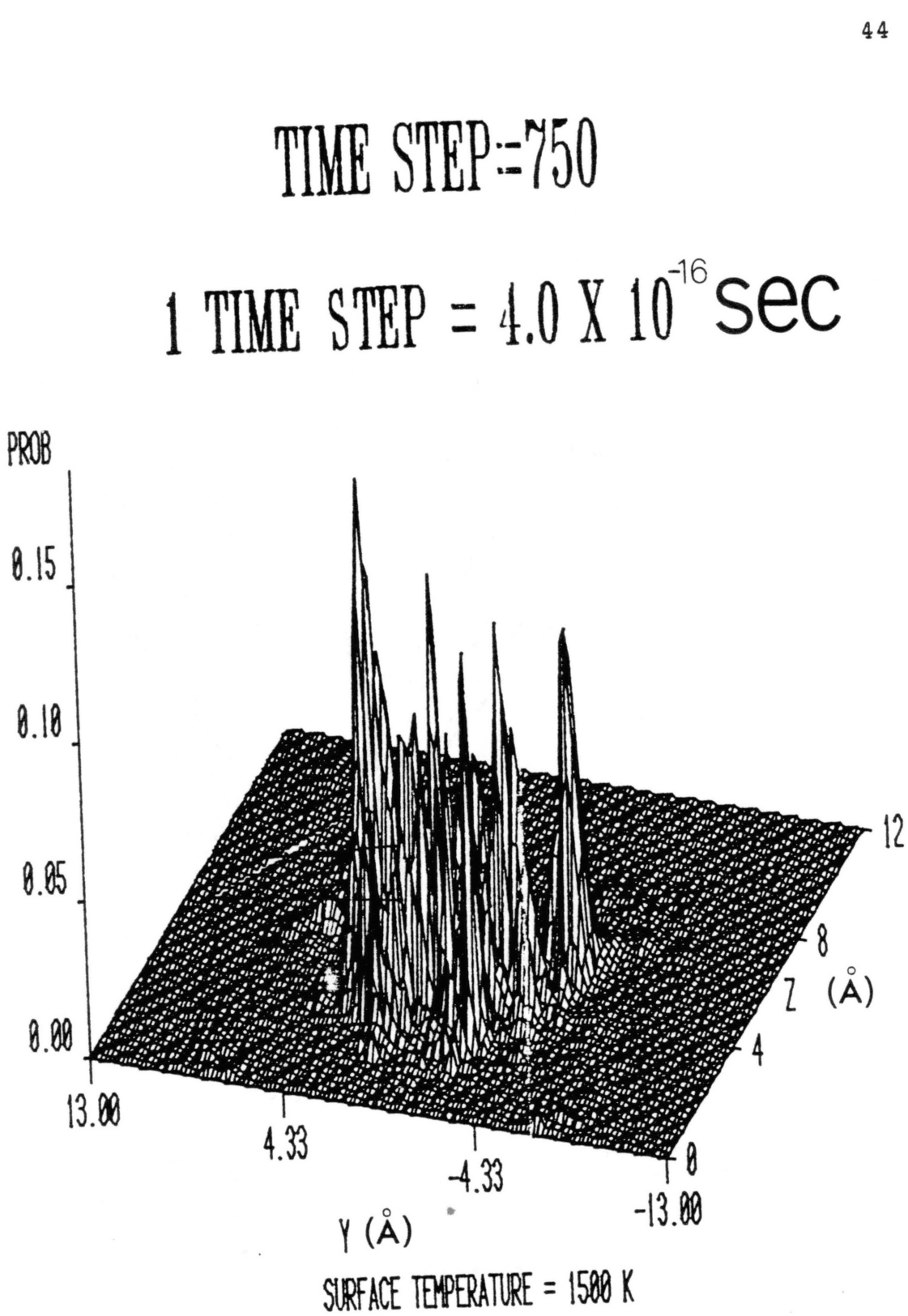

Figure 9. Final-State Probability Density for Normal Incidence

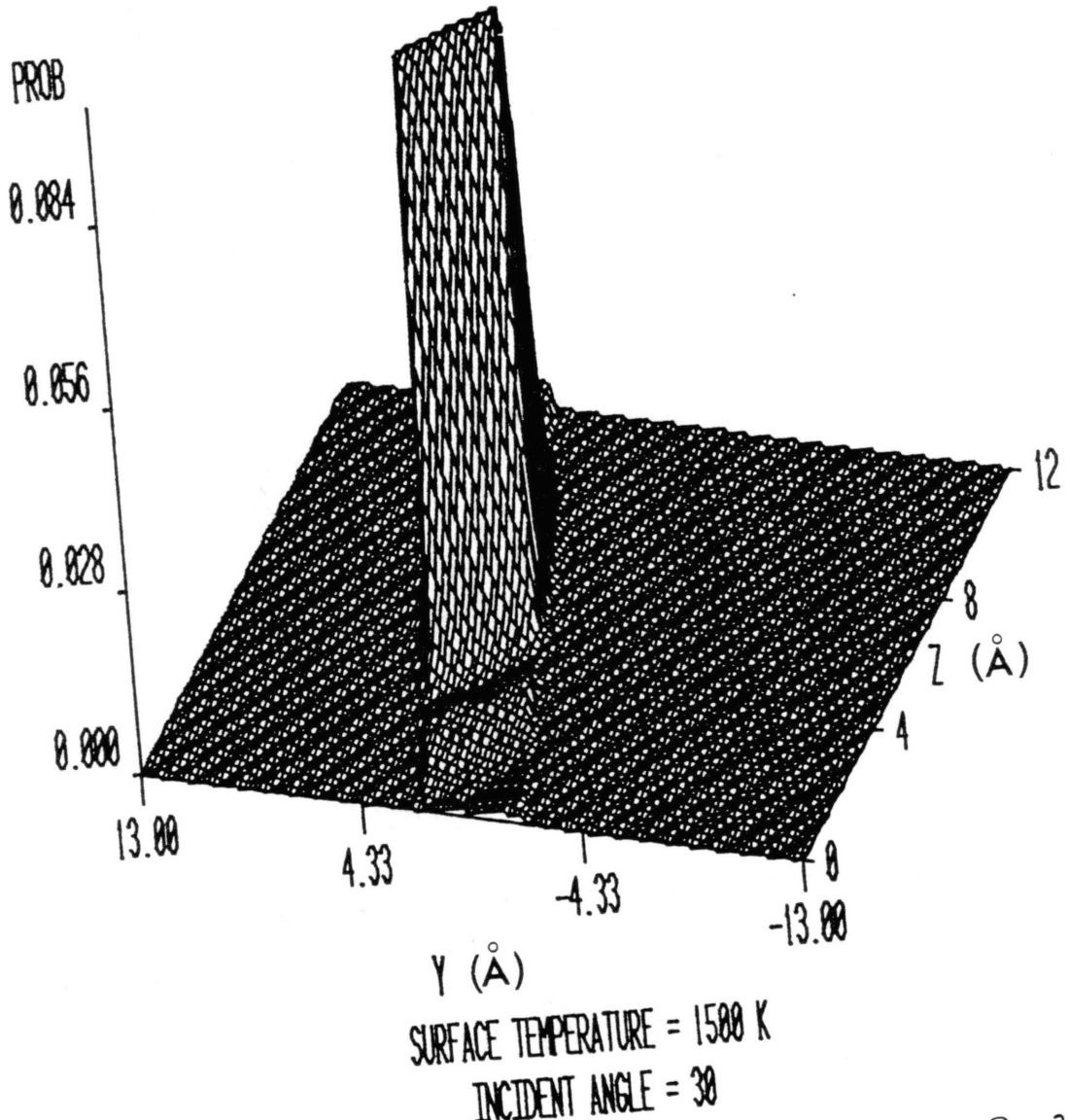

Figure 10. Initial Probability Density for $\Theta_i = 30°$.

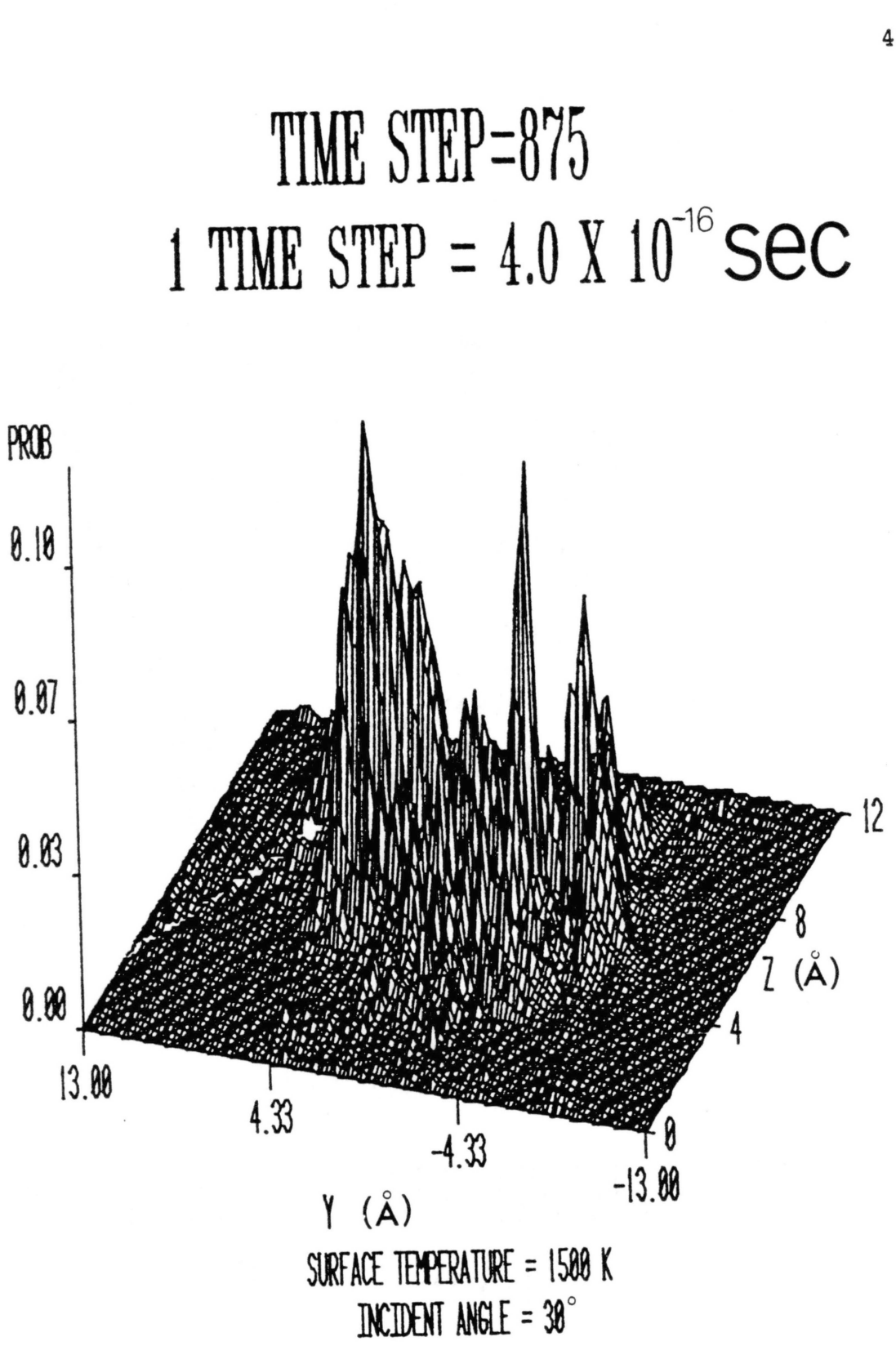

Figure 11. Final-State Probability Density for $\Theta = 30°$.

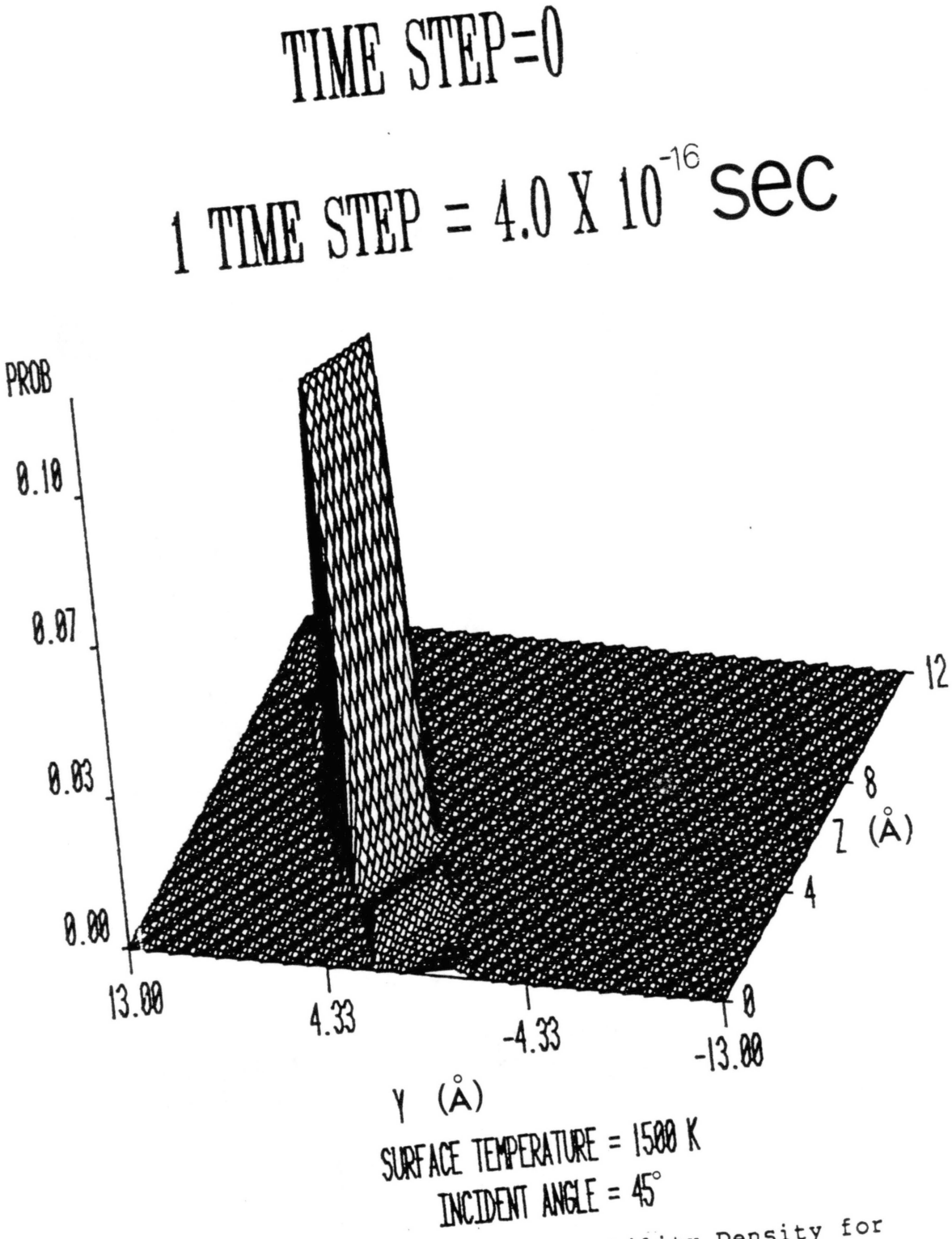

Figure 12. Initial Probability Density for $\Theta_i = 45°$.

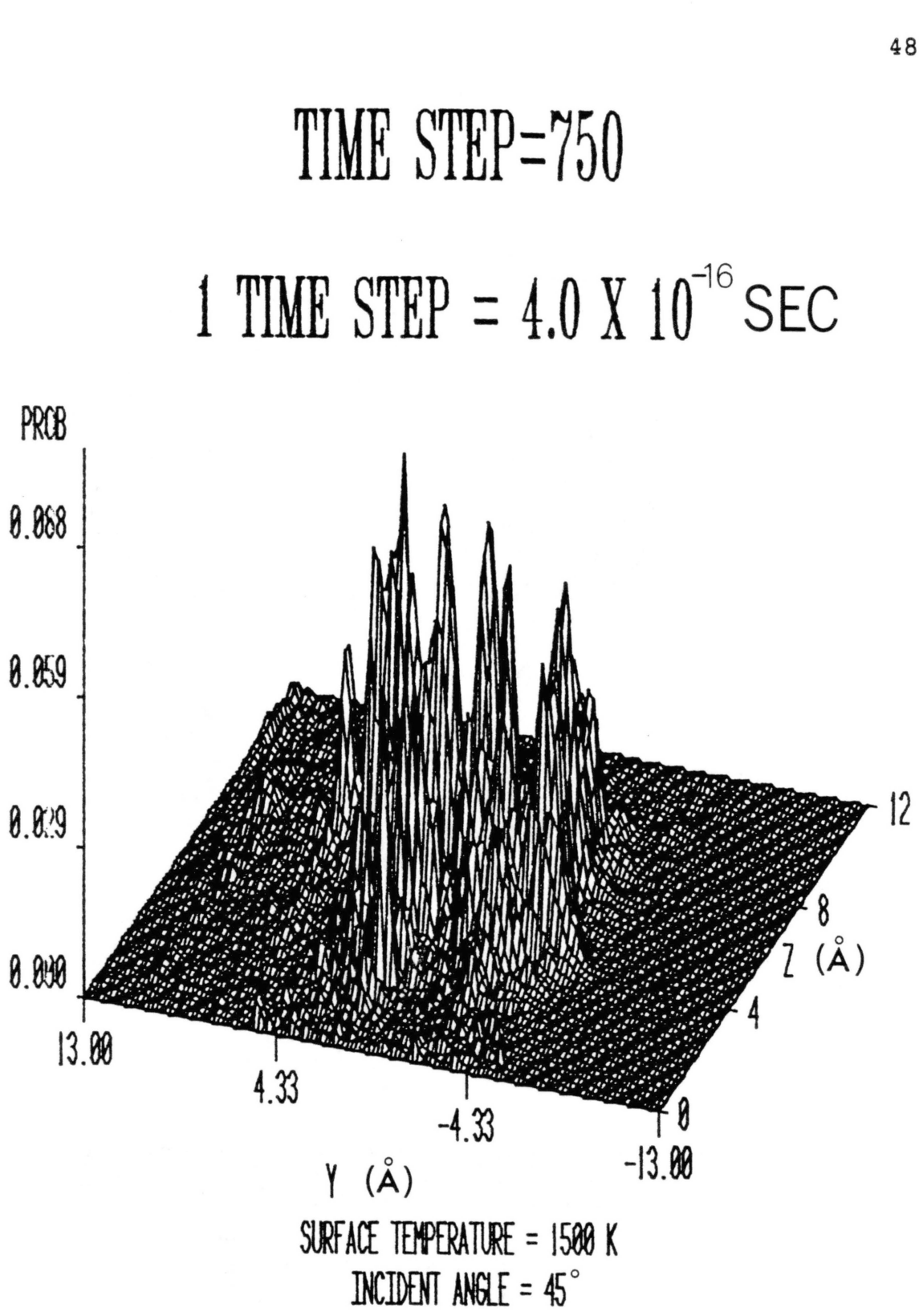

Figure 13. Final-State Probability Density for $\Theta_i = 45°$.

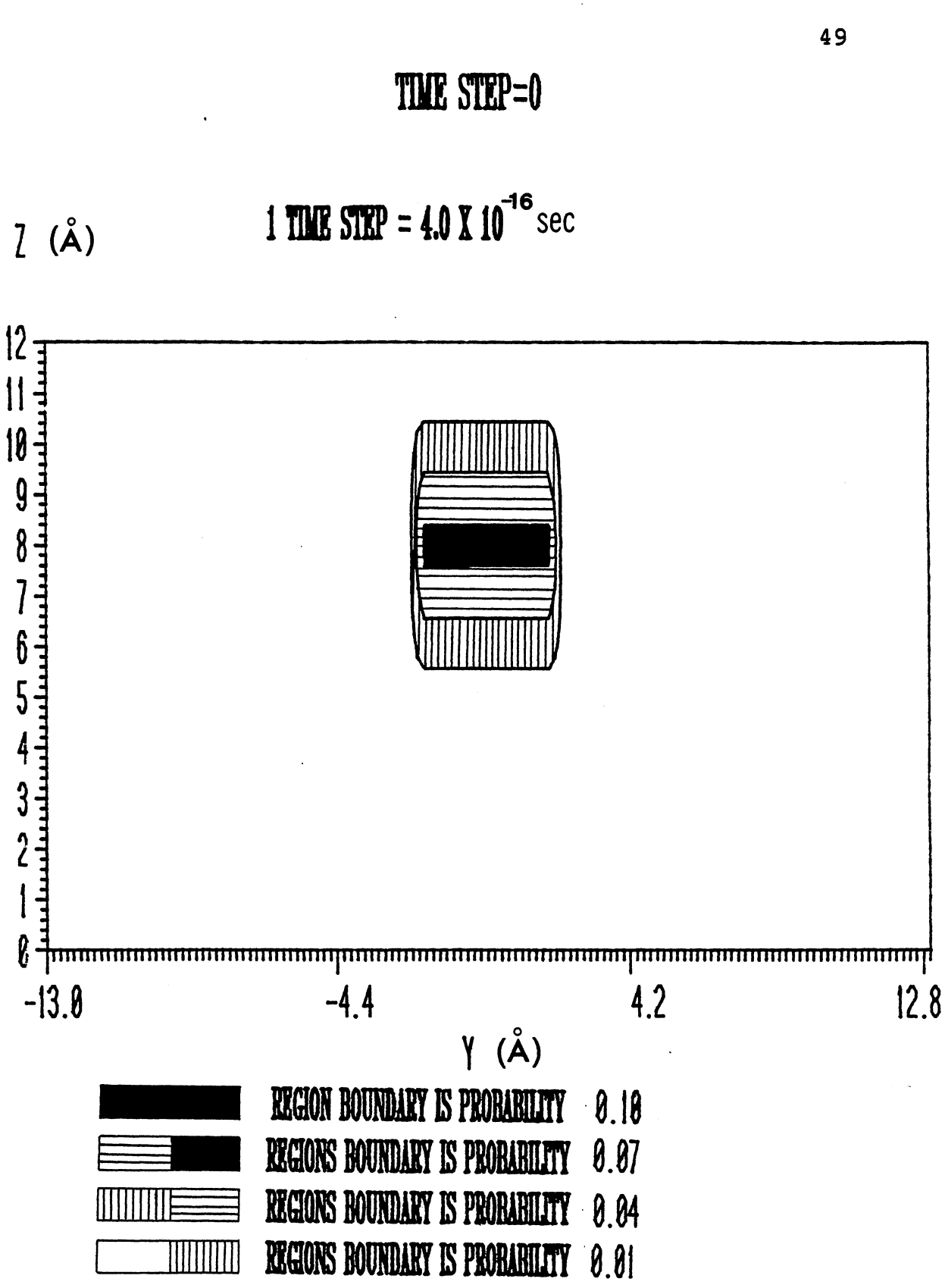

Figure 14. Level Curves of Initial Probability Density for Normal Incidence and T_s = 1500 K.

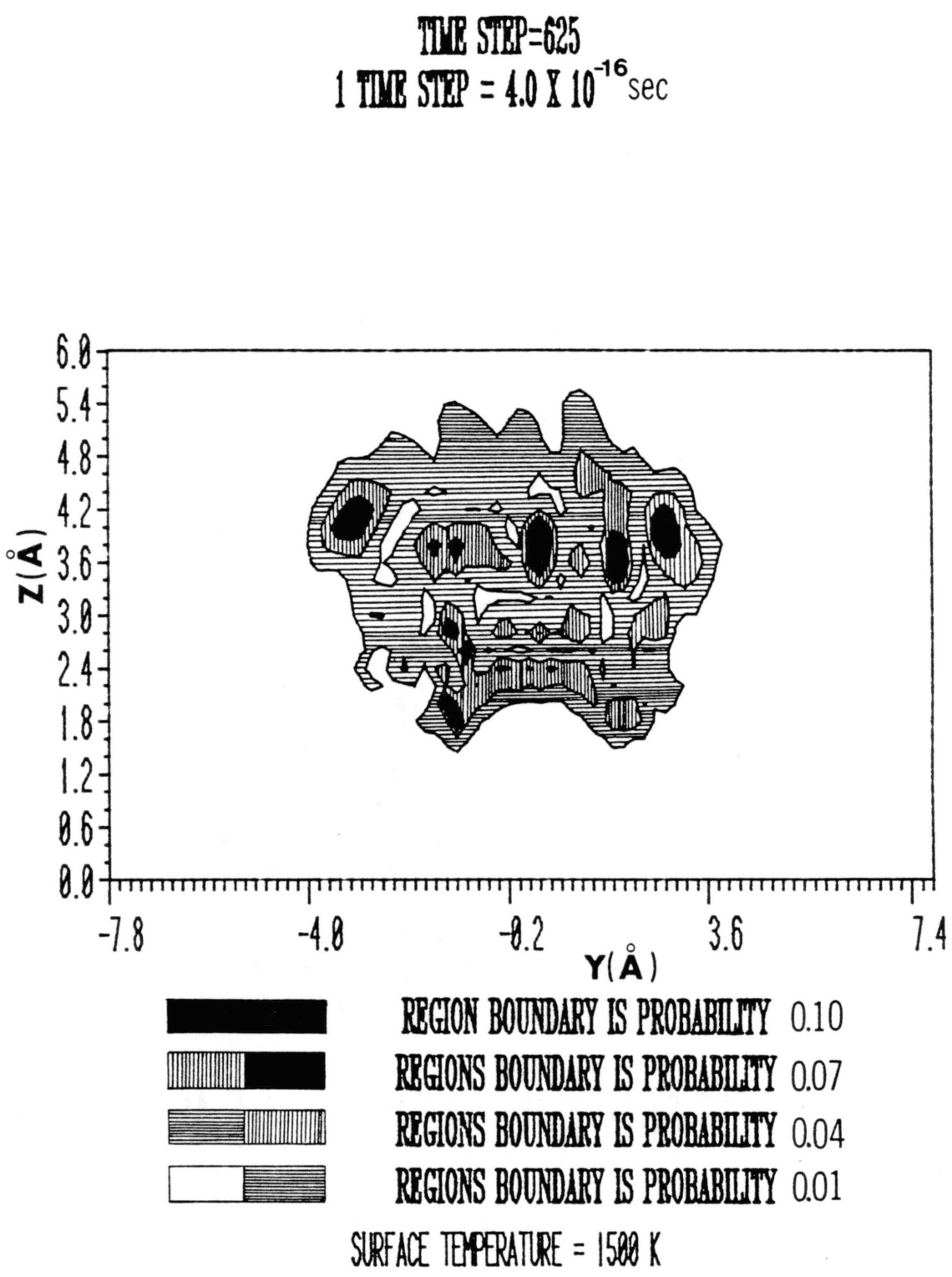

Figure 15. Level Curves of Final-State Probability Density for Normal Incidence and T_S = 1500 K.

D. Energy Transfer

Figures 16-18 show the variation of the average exiting kinetic energy of the gas atom, $\langle E_e \rangle$, with surface temperature, T_S , for normal, 30°, and 45° incidence. The triangles represent the results obtained in the 2D model (61) while the pluses show the data found upon expansion to a 3D model surface. The values predicted by the 3D model are generally shifted to higher energies. This is attributed to the presence of more energy in the lattice. In the 3D model, there are 9 atoms each having $3kT_S$ energy. The 2D model gives energy to a 3-atom lattice vibrating in a symmetric stretching mode. The lattice atoms have four times as much energy per atom in the 3D model as in the 2D model, and there are three times as many atoms. A shift to greater energy transferred in the 3D model is then not unexpected. Figure 19 shows the variation of the $\langle E_e \rangle$ with average incident kinetic energy, $\langle E_i \rangle$, for normal incidence, and Figure 20 shows the variation of the reduced $\langle E_e \rangle$ with reduced $\langle E_i \rangle$. In each case, the energy values are reduced by a factor $2kT_S$. The behavior shown in Figures 16-20 is qualitatively very similar to that found by Janda, Hurst, Becker, Cowin, Auerbach, and Wharton (76) in their measurements of Ar atoms scattered from W. The rest of the data are suggestive of inelastic scattering characterized by a linearly proportional relationship between $\langle E_e \rangle$ and both $\langle E_i \rangle$ and T_S. Similar behavior was found to occur for the Ar/W system when the scattering was determined via "hard-

cube" and "hard-sphere" impulsive models (77,78). Figure 21 shows the variation of $\langle E_e \rangle / 2kT_S$ with $\langle E_i \rangle / 2kT_S$ pridicted by the "hard-cube" model for several mass ratios, where the mass ratio, μ , is the ratio of the mass of the gas atom to the mass of a surface atom. The data for $\mu = 1/3$, 1/5, and 1/7 were taken from the data of Barker and Auerbach (77). Figure 21 alsc shows data produced by the present calculations. The $\mu = 1/20$ line in Figure 21 is extended by a dashed line to allow visual comparison with the results of the "hard-cube" calculation.

As an aid in interpreting the energy transfer data, energy transfer coefficients and accommodation coefficients were determined in the manner described by Lorenzen and Raff (79). The energy transfer coefficient, α_E , is determined using

$$\alpha_E = (\langle E_i \rangle - \langle E_e \rangle)/\langle E_i \rangle . \qquad (86)$$

The energy accommodation coefficient, EAC, is determined from

$$EAC = \alpha_E/\{(2k_b T_S/\langle E_i \rangle) - 1\} . \qquad (87)$$

Figure 22 shows the variation of α_E with $\langle E_i \rangle$ for T_S = 1500 K and normal incidence. This behavior is qualitatively similar to that found in the classical 3D calculation (75). Figure 23 shows the variation of α_E with T_S for $\langle E_i \rangle$ = .089 eV. A decrease in α_E is observed for higher surface temperatures. This is also qualitatively

similar to that found in the classical 3D calculation. Figure 24 shows the variation of α_E with Θ_i for surface temperatures of 300,800, and 1500 K. The magnitude of α_E is seen to decrease upon increased incident angle. This behavior is indicative of less energy transferred upon increased incident angle and mimics the behavior of the classical 3D model. In the classical 3D model, where the surface temperature is 0 K, energy transfer can only be from the gas to the surface, and the magnitude of the energy transferred diminishes. In the present 3D calculation, the amount of energy transferred also diminishes with increased incident angle. In the classical model, it was discovered that the curvature of the potential-energy contours decreased in going from a 2D model to a 3D model. The same behavior should occur here in spite of the use of a Lennard-Jones potential instead of a Morse potential. The energy transfer from the parallel momentum components was observed to become much smaller in the classical calculation. In this treatise, a decrease in $\langle E_e \rangle$ in Equation (86) will cause an increase in α_E . In the classical 3D model, the decrease in $\langle E_e \rangle$ yields a decrease in α_E. In both cases however, the amount of energy transferred decreases with increasing incident angle. Figures 25 and 26 show the variation of the EAC with T_S and with $\langle E_i \rangle$, respectively, for normal incidence. Figures 27 and 28 show the variation of the EAC with T_S for $\Theta_i = 30^\circ$ and $\Theta_i = 45^\circ$, respectively. The EAC shows the hyperbolic form expected from Eq. (87).

The initial momentum distribution of the model wave packet having $<E_i>$ = .089 eV and perpendicular incidence upon the surface is shown in Figure 29. The small shoulder immediately to the right of the main peak between 7 and 9 momentum units is due to the fact that the distribution of the momentum conjugate to the q_2 coordinate is not square. The final-state momentum distribution for normal incidence, $<E_i>$ = .089 eV, and T_S = 1500 K, obtained from Equation 65b is given in Figure 30. The momentum distribution can be transformed into a distribution of energies as shown in Figure 31. The energy spacings here are .02 eV or multiples of .02 eV and are shown in Table II. This energy difference corresponds to a frequency of about 5.00×10^{12} sec^{-1} . The associated time period is found to closely approximate the time period necessary for a classical particle, having the mass of a hydrogen atom and average incident energy of .089 eV, to cross the interaction potential well and return.

The bond distance between any two of the moving lattice sites is a periodic function. This periodic function can be "understood" by expanding it into a Fourier series such as

$$f(x) \cong 2 \sum_{j=0}^{\infty} |\hat{f}(j)| \cos(\theta_j + jx) . \qquad (88)$$

In this way f(x) has been represented by a sum or superpositon of simple harmonic oscillations. The j-th motion is given by

$$2|\hat{f}(j)|\cos(\theta_j + jx) ,$$

where the amplitude is given by $2|\hat{f}(j)|$, the frequency is given by $j/2\pi$ and the phase angle by θ_j . The sequence of

the squares of the coefficients is called the power spectrum. A plot of the power spectrum for one of the lattice bonds at T_S = 1500 K is shown in Figure 32. The frequencies in the plot have been converted to cm^{-1} . The spectrum is characterized by the prevalence of a quartet of peaks of similar shape and diminishing intensity at intervals of approximately 81 cm^{-1} . The power spectrum for T_S = 300 K was found to be virtually identical to that at T_S= 1500 K. The spacings between the quartets correspond to about one half the frequency associated with the energy spacings between the maxima of the energy distribution. A correlation between the spacings of the energy distribution and the lattice frequencies occurs for the 3D model as was found in the 2D model (61). Energy transfer then occurs when the time that the gas atom spends in the interaction potential well matches a two-phonon process of the lattice. Figures 33 and 34 show the final-state momentum distributions for $\langle E_i \rangle$ = .094764 eV, $\Theta_i = 30^\circ$, T_S = 1500 K, and $\langle E_i \rangle$ = .096647 eV, $\Theta_i = 45^\circ$, T_S = 1500 K, respectively. Figures 35-37 show the corresponding final-state momentum distributions for incident angles of 0°, 30° , and 45° , respectively, but for a surface temperature of 300 K.

TABLE II.

PEAK POSITIONS AND ENERGY SPACINGS FOR ENERGY DISTRIBUTION

Peak Position (eV)	Spacing (eV)
.036	
	.018
.054	
	.040
.094	
	.023
.117	
	.044
.161	
	.050
.211	
	.034
.245	
	.046
.291	
	.024
.315	
	.060
.375	
	.027
.402	
	.038
.440	

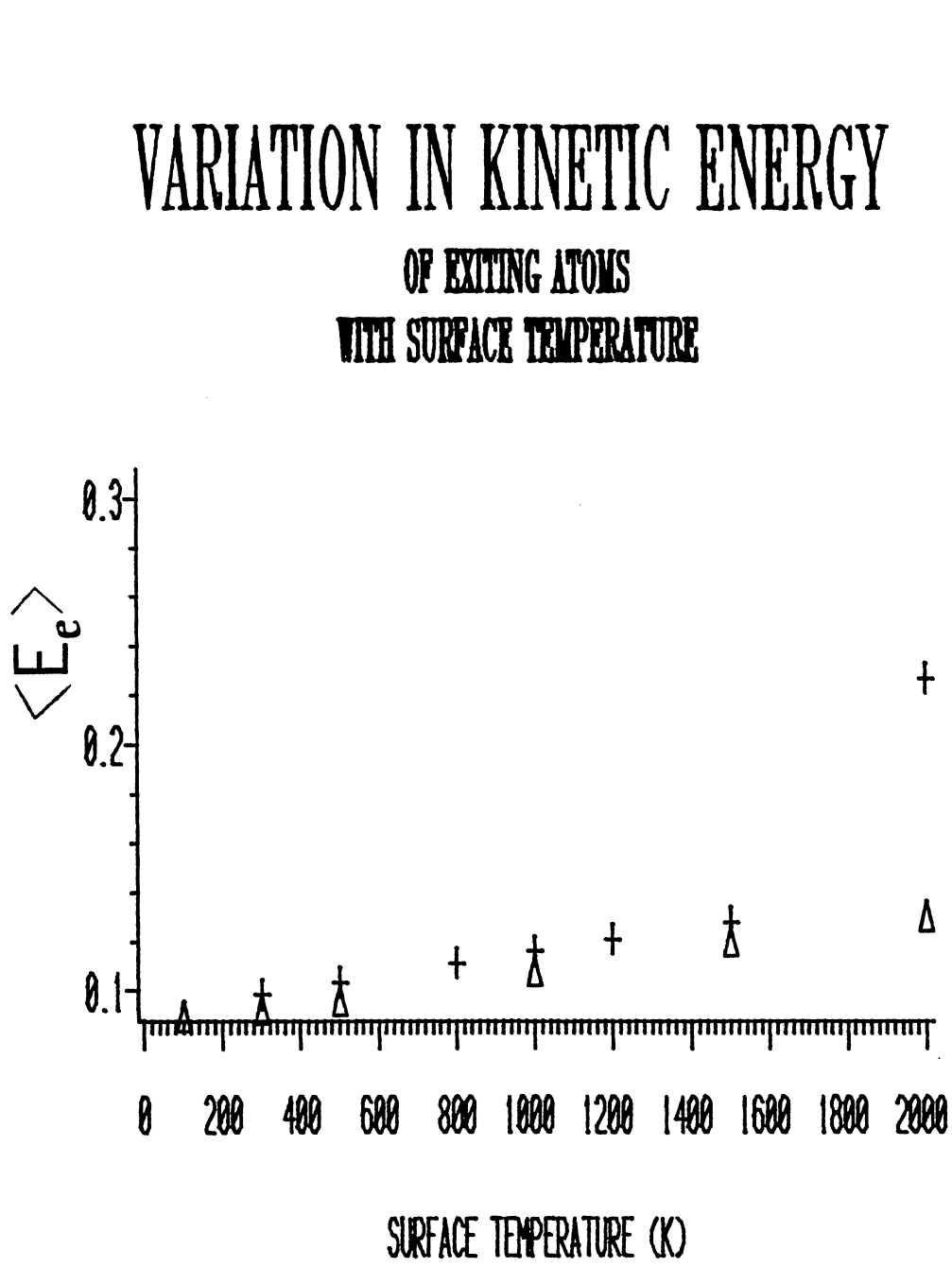

Figure 16. Variation of $\langle E_e \rangle$ with T_s for $\Theta_i = 0^\circ$.

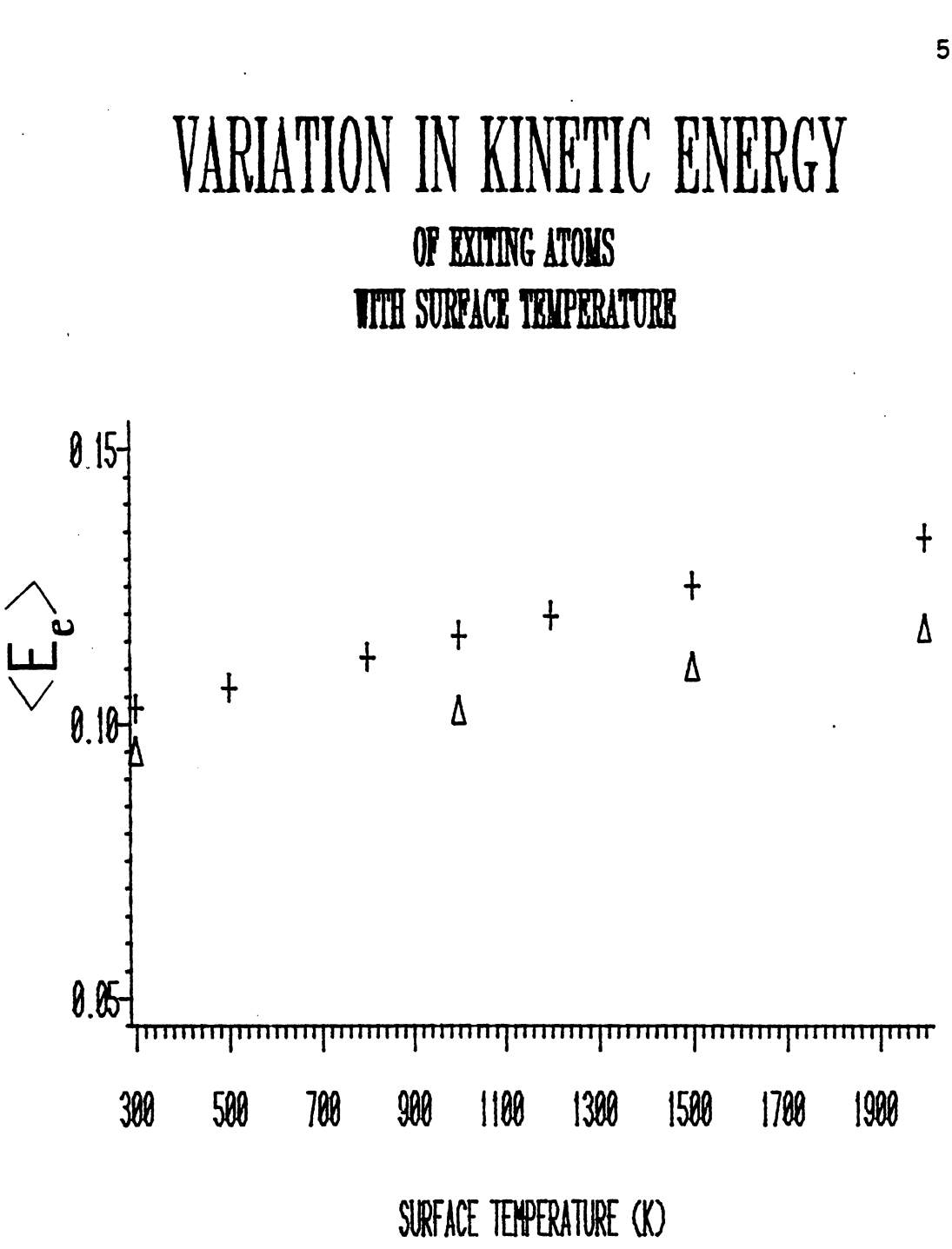

Figure 17. Variation of $\langle E_e \rangle$ with T_s for $\Theta_i = 30^\circ$.

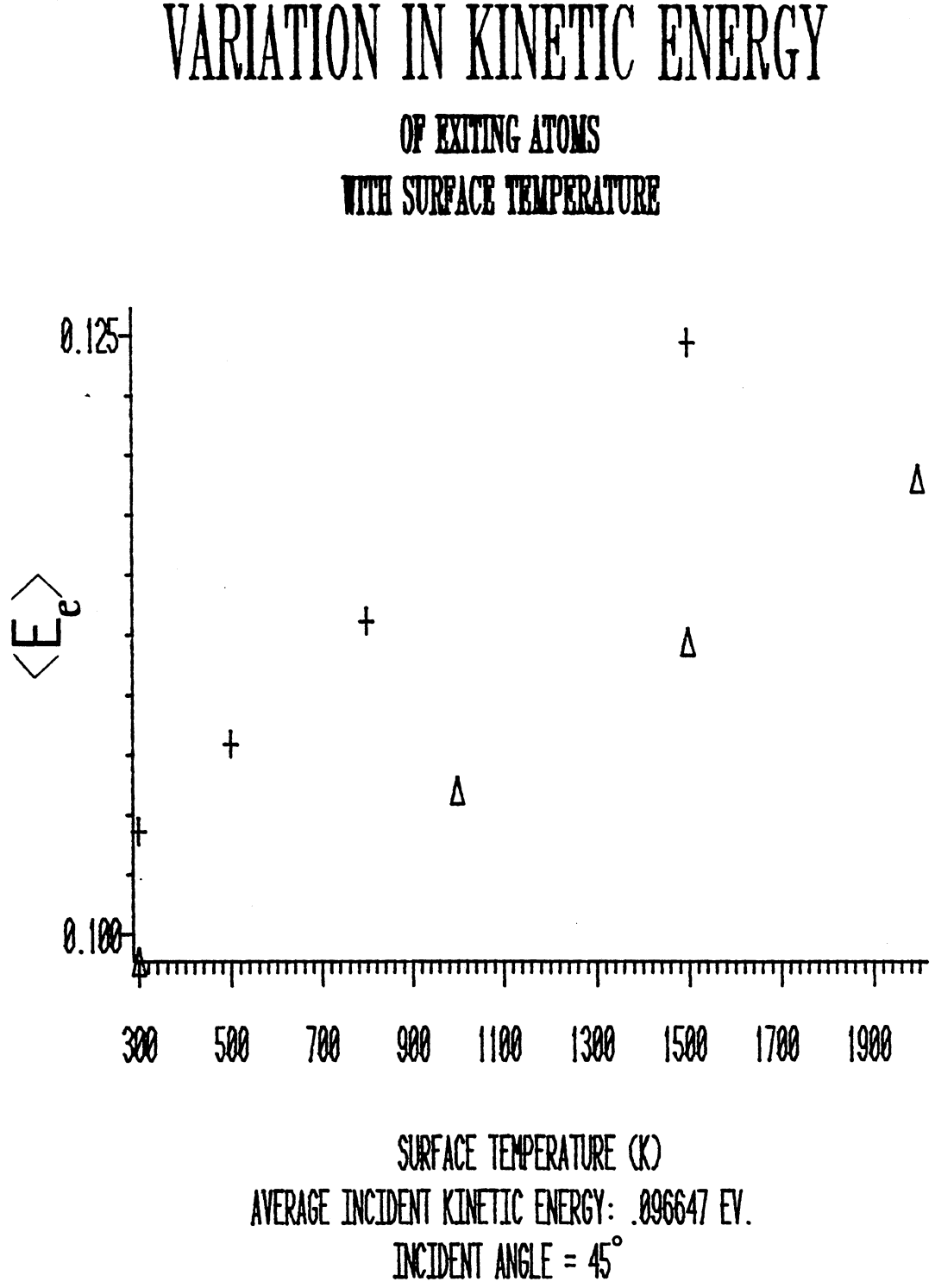

Figure 18. Variation of $\langle E_e \rangle$ with T_s for $\Theta_i = 45^\circ$.

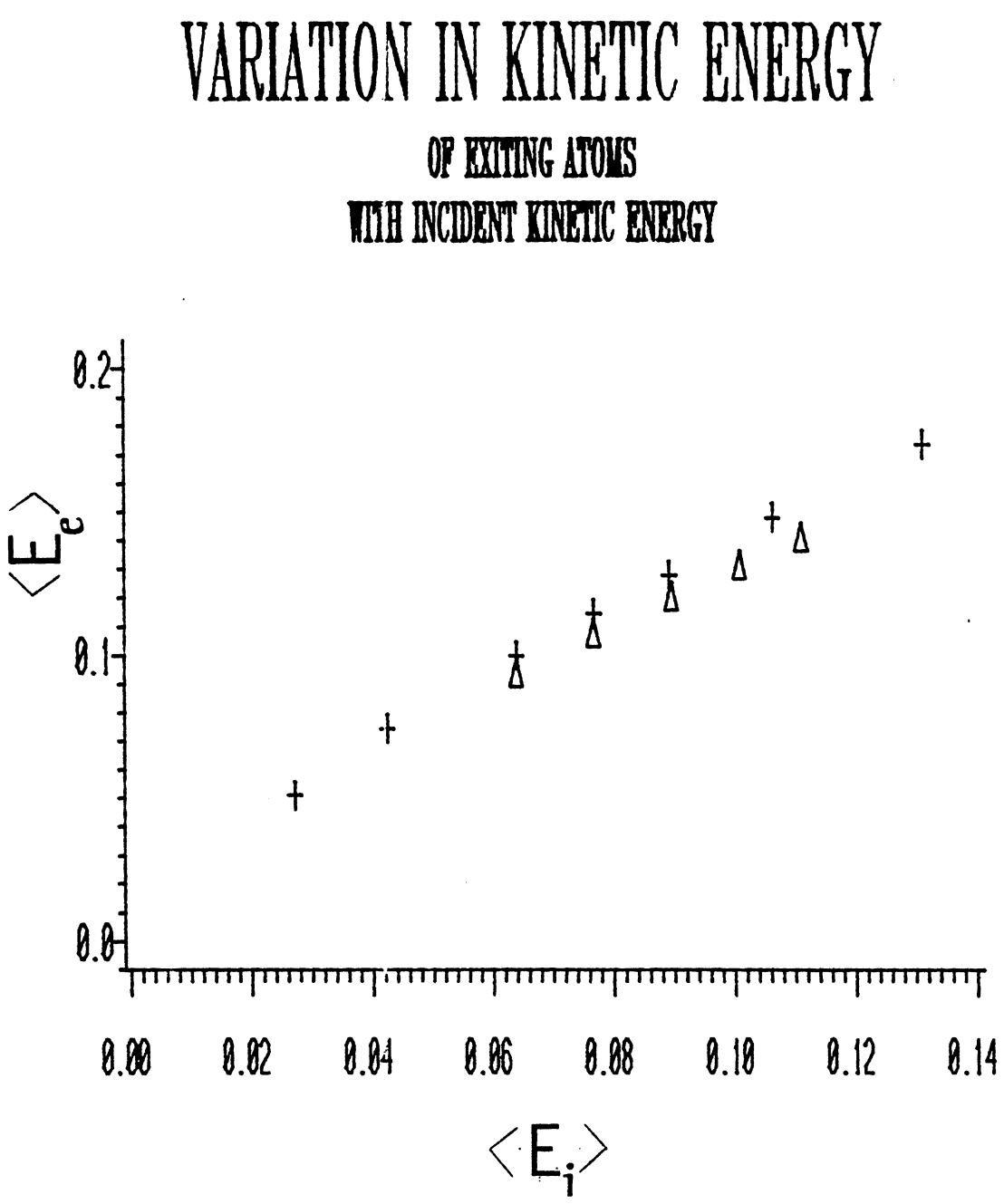

Figure 19. Variation of $\langle E_e \rangle$ with $\langle E_i \rangle$ for $T = 1500$ K and $\Theta_i = 0^\circ$.

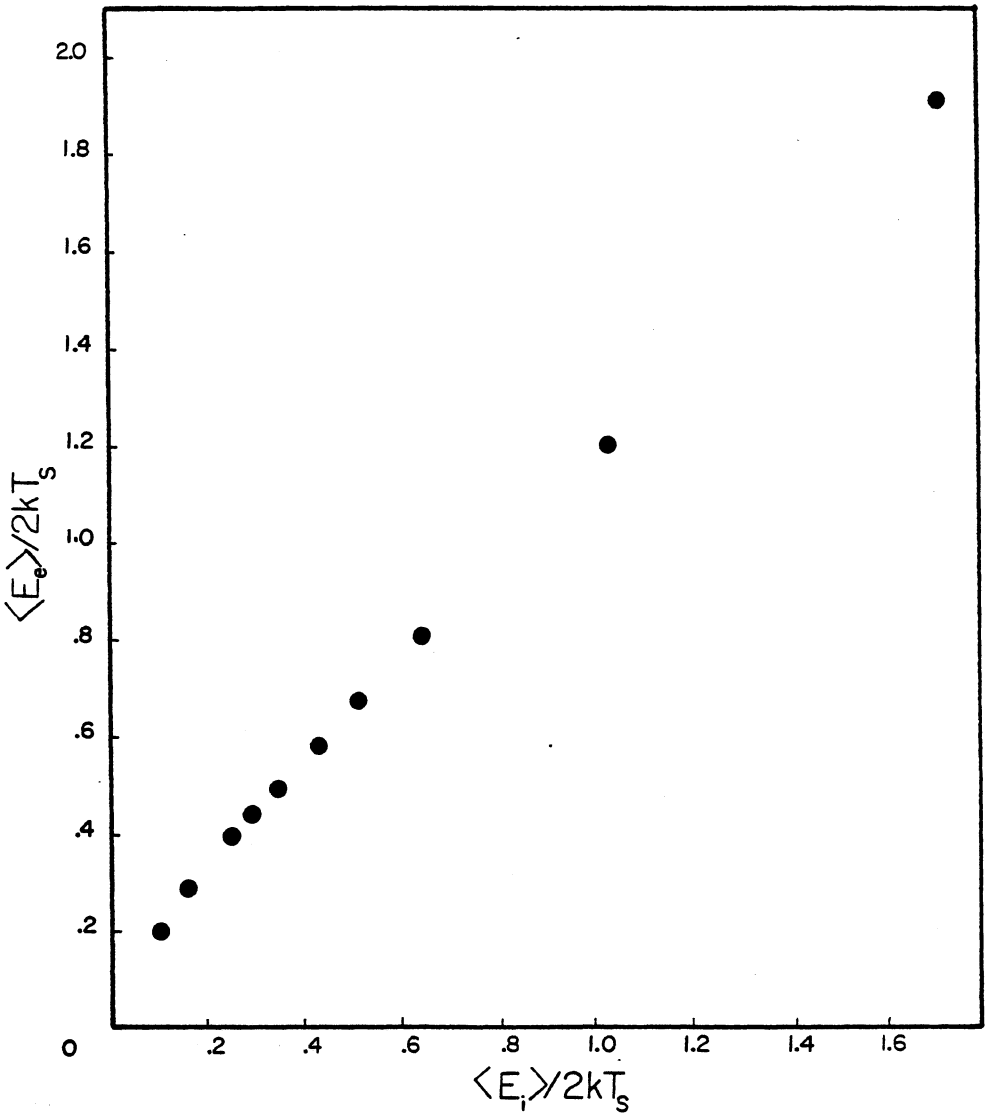

Figure 20. Variation of $\langle E_e \rangle / 2k_b T_s$ with $\langle E_i \rangle / 2k_b T_s$

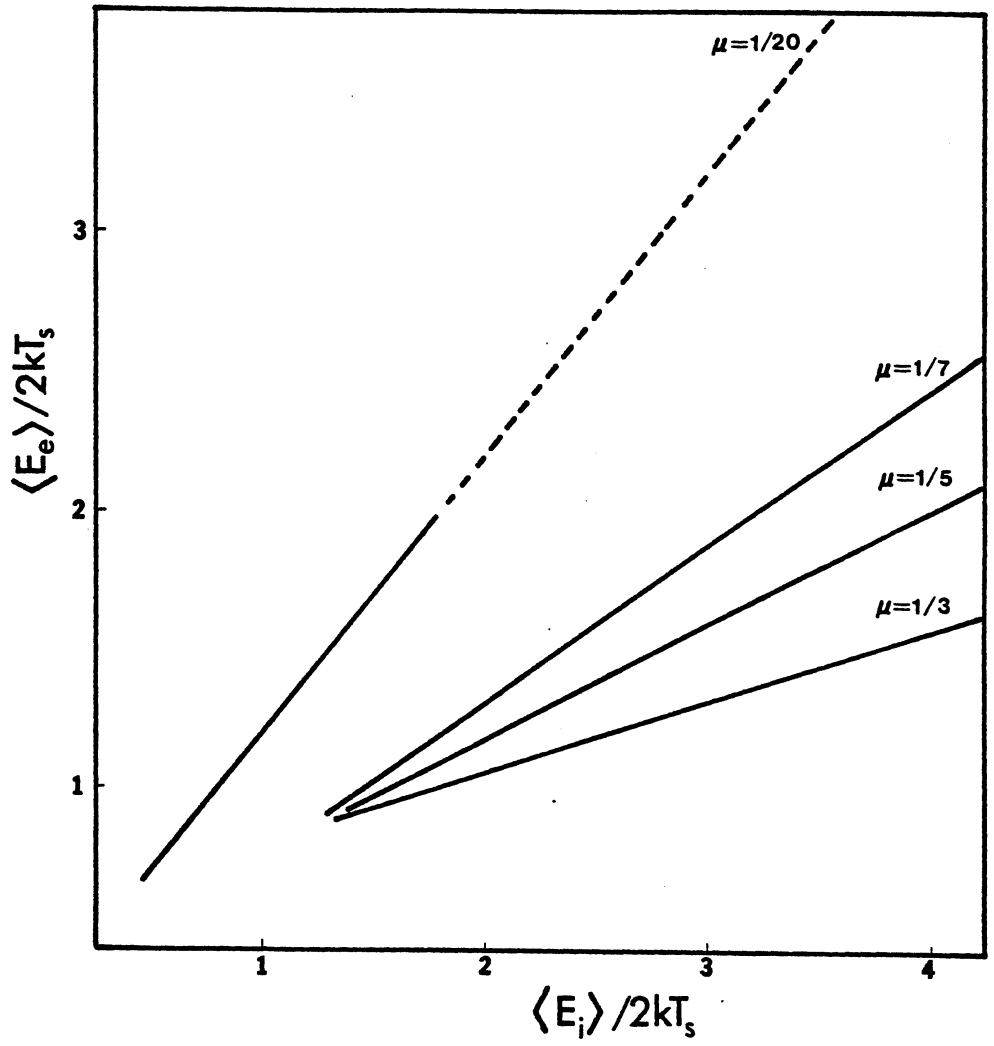

Figure 21. Comparison of Variations of $\langle E_e \rangle / 2kT_s$ with $\langle E_i \rangle / 2kT_s$ for Different Reduced Mass Values as Predicted by the "Hard Cube" Model.

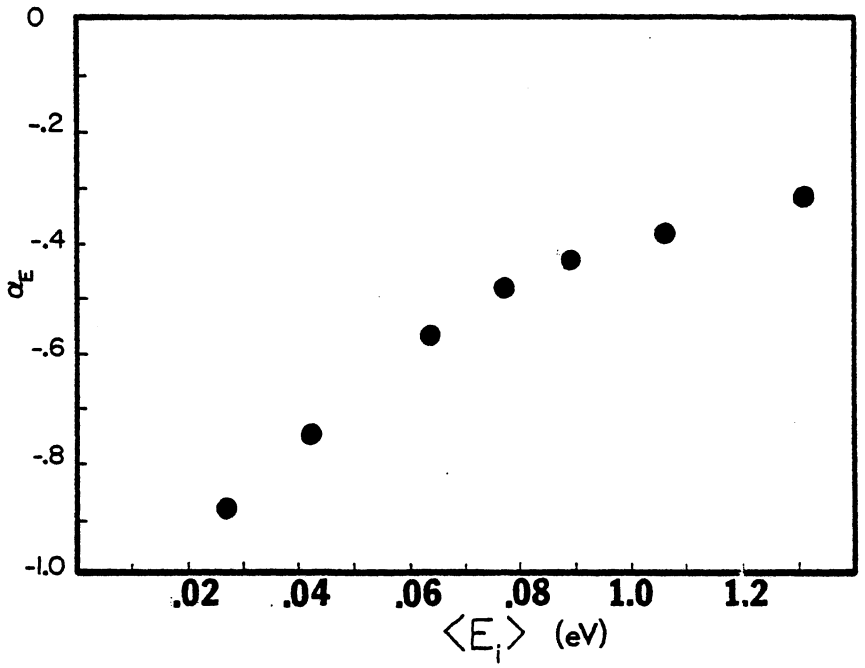

Figure 22. Computed Variation of α_E with $\langle E_i \rangle$ for T_S = 1500K and Θ_i = 0°.

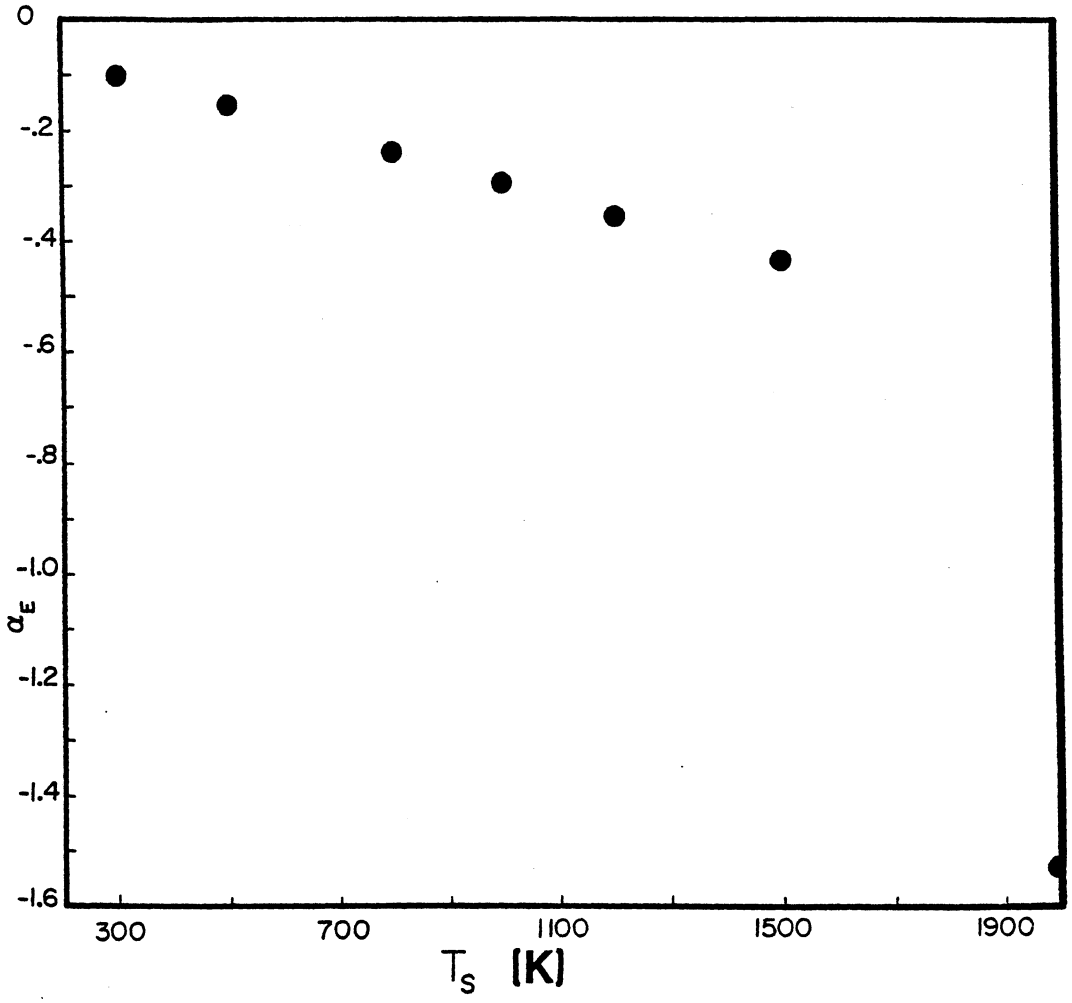

Figure 23. Computed Variation of α_E with T_S for $\langle E_i \rangle$ = .089 eV.

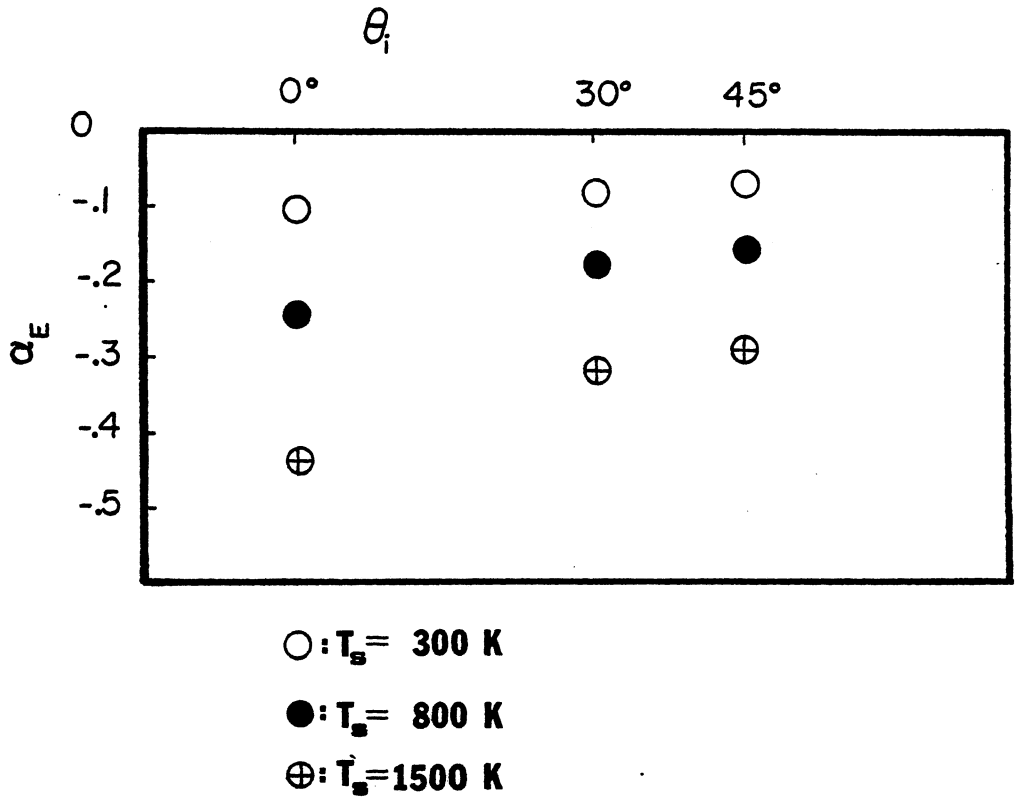

Figure 24 Variation of α_E with Θ_i for T_S = 300,800, and 1500 K.

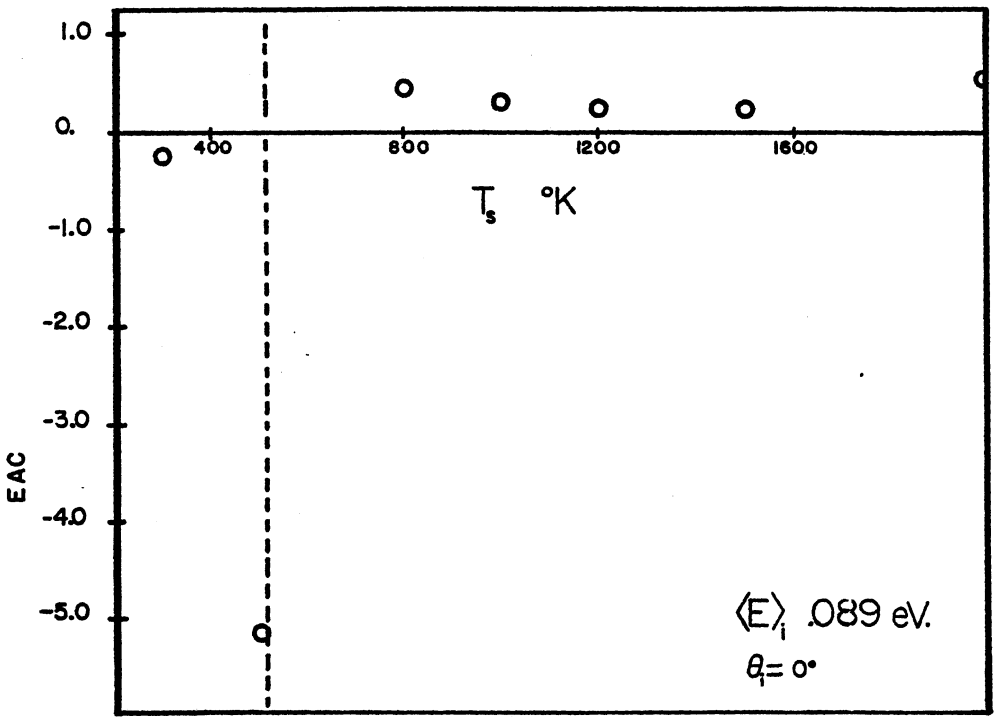

Figure 25. Calculated Variation of the EAC with T_s.

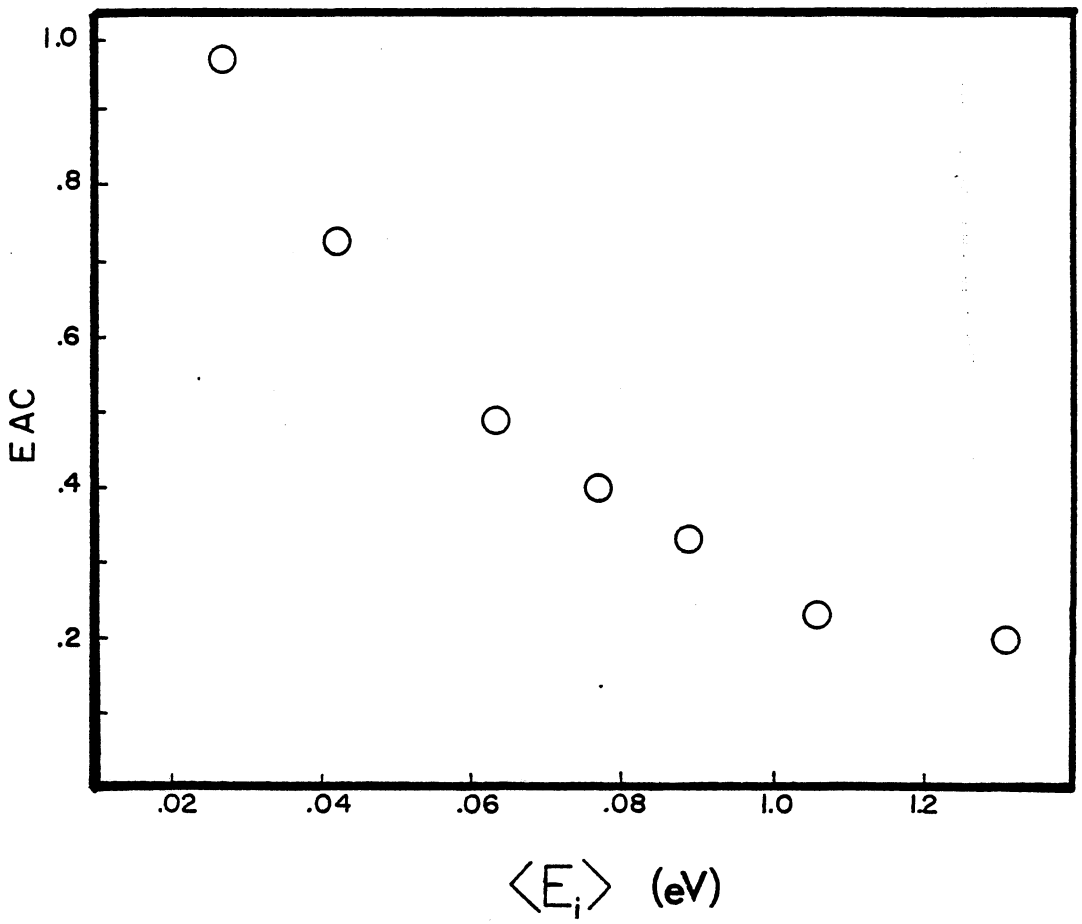

Figure 26. Calculated Variation of the EAC with $\langle E_i \rangle$ for T_s = 1500K and $\Theta_i = 0^\circ$.

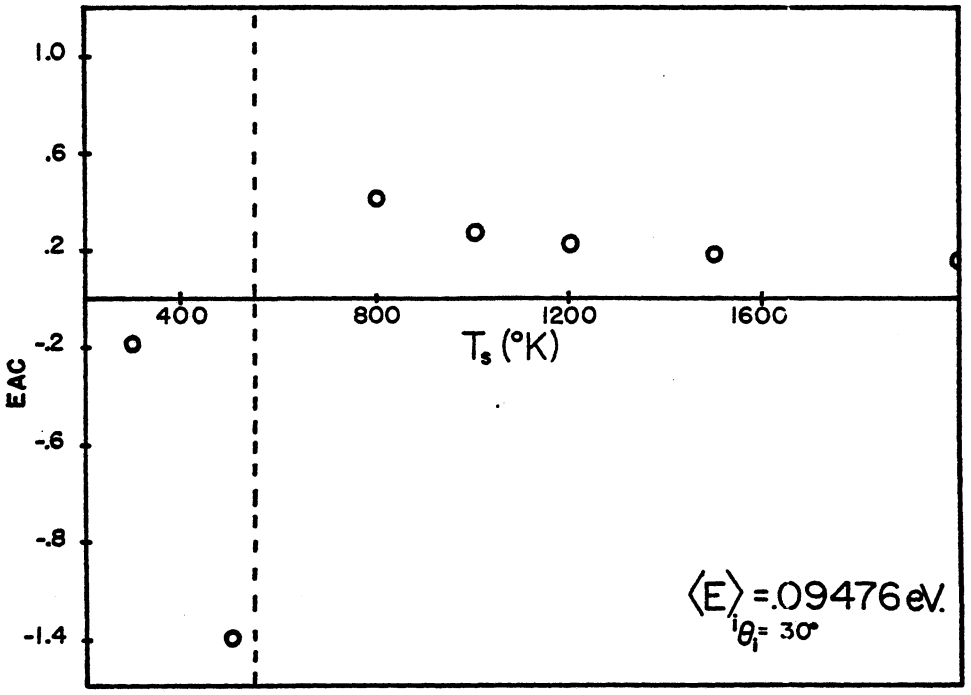

Figure 27. Calculated Variation of the EAC with T_s for $\Theta_i = 30°$.

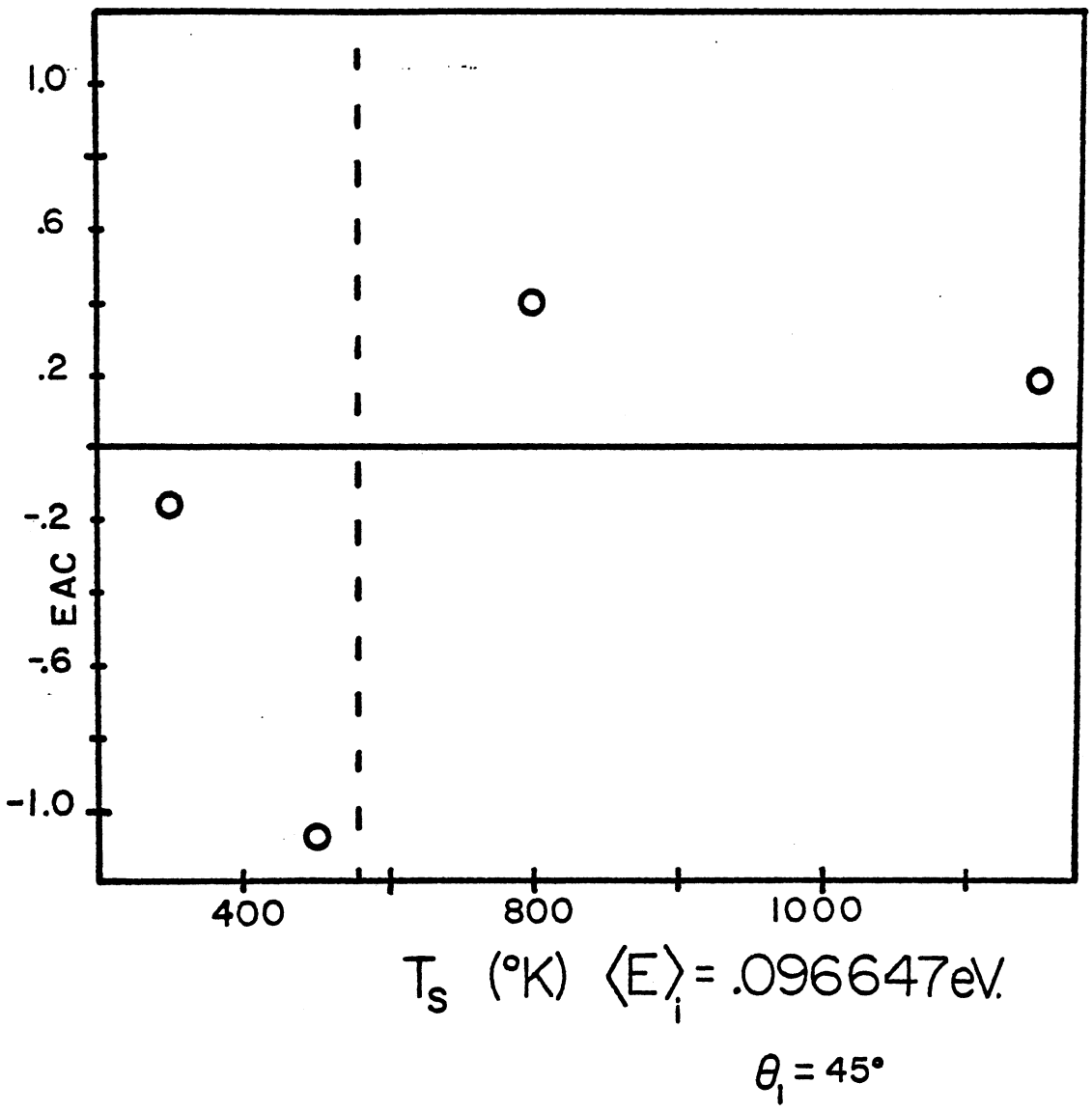

Figure 28. Variation of the EAC with T_S for Θ_i= 45°.

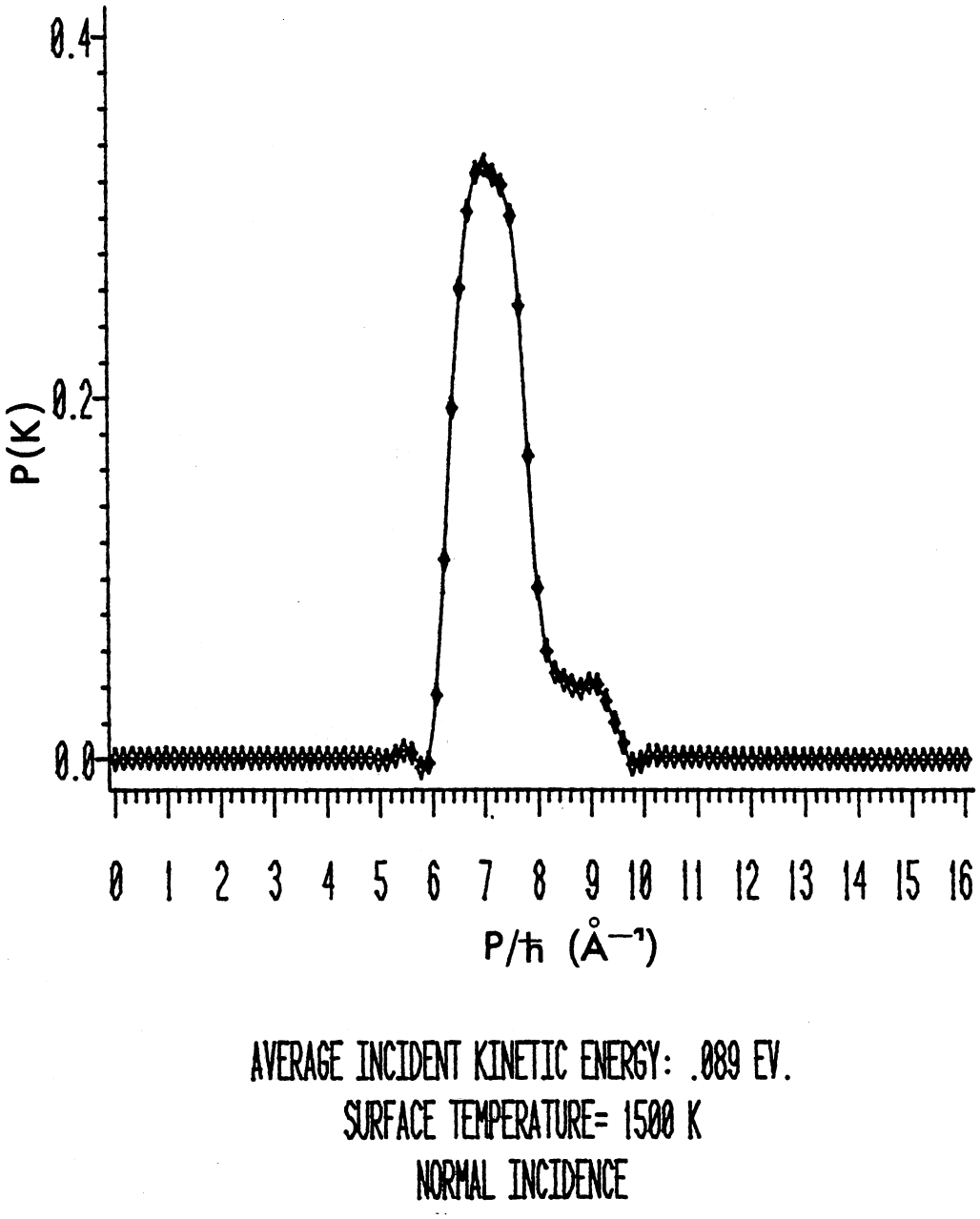

Figure 29. Initial Momentum Distribution for Normal Incidence and $\langle E_i \rangle$ = .089 eV.

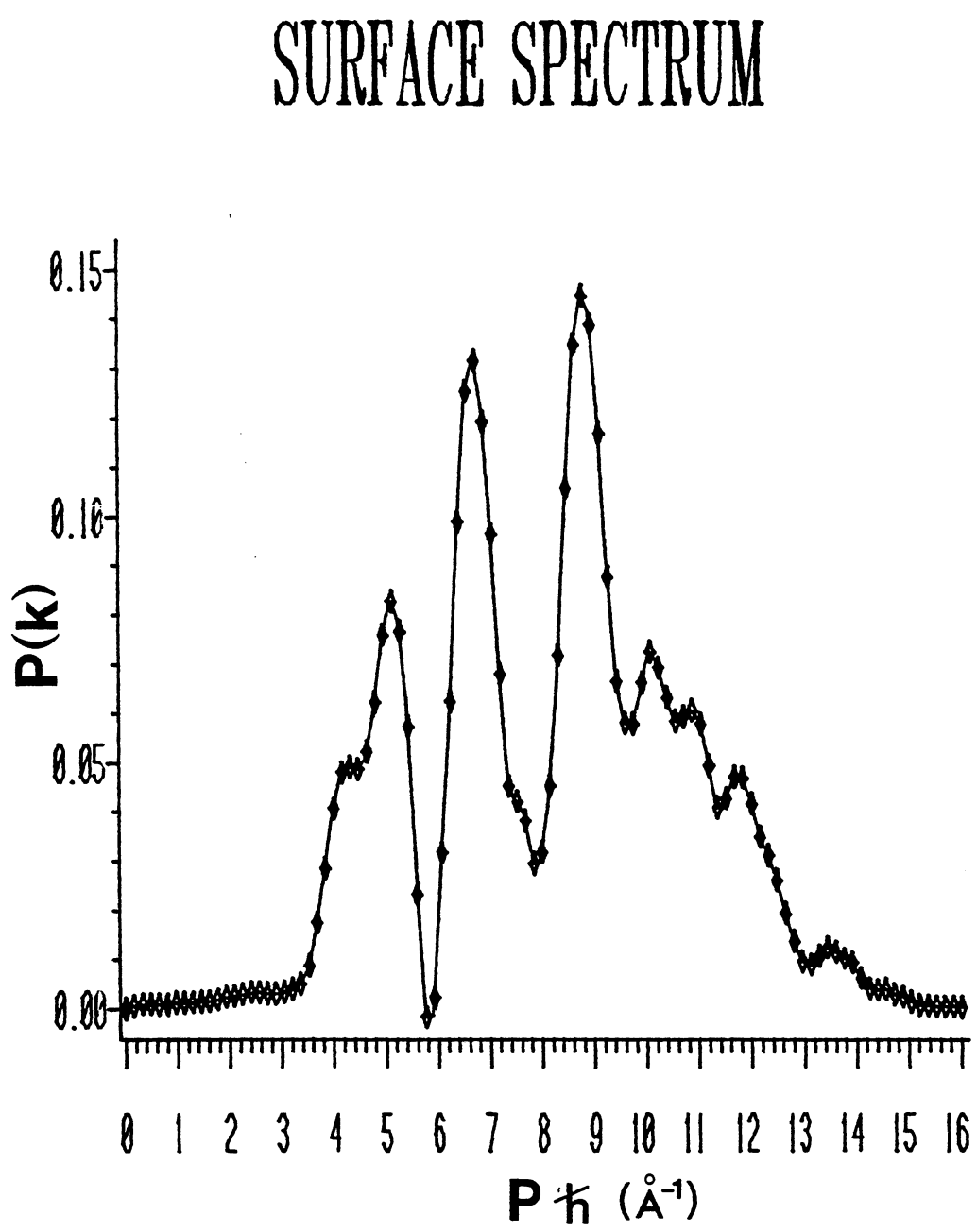

Figure 30. Final-State Momentum Distribution for $\Theta_i = 0°$, $\langle E_i \rangle = .089$ eV, and $T_S = 1500$ K.

ENERGY DISTRIBUTION

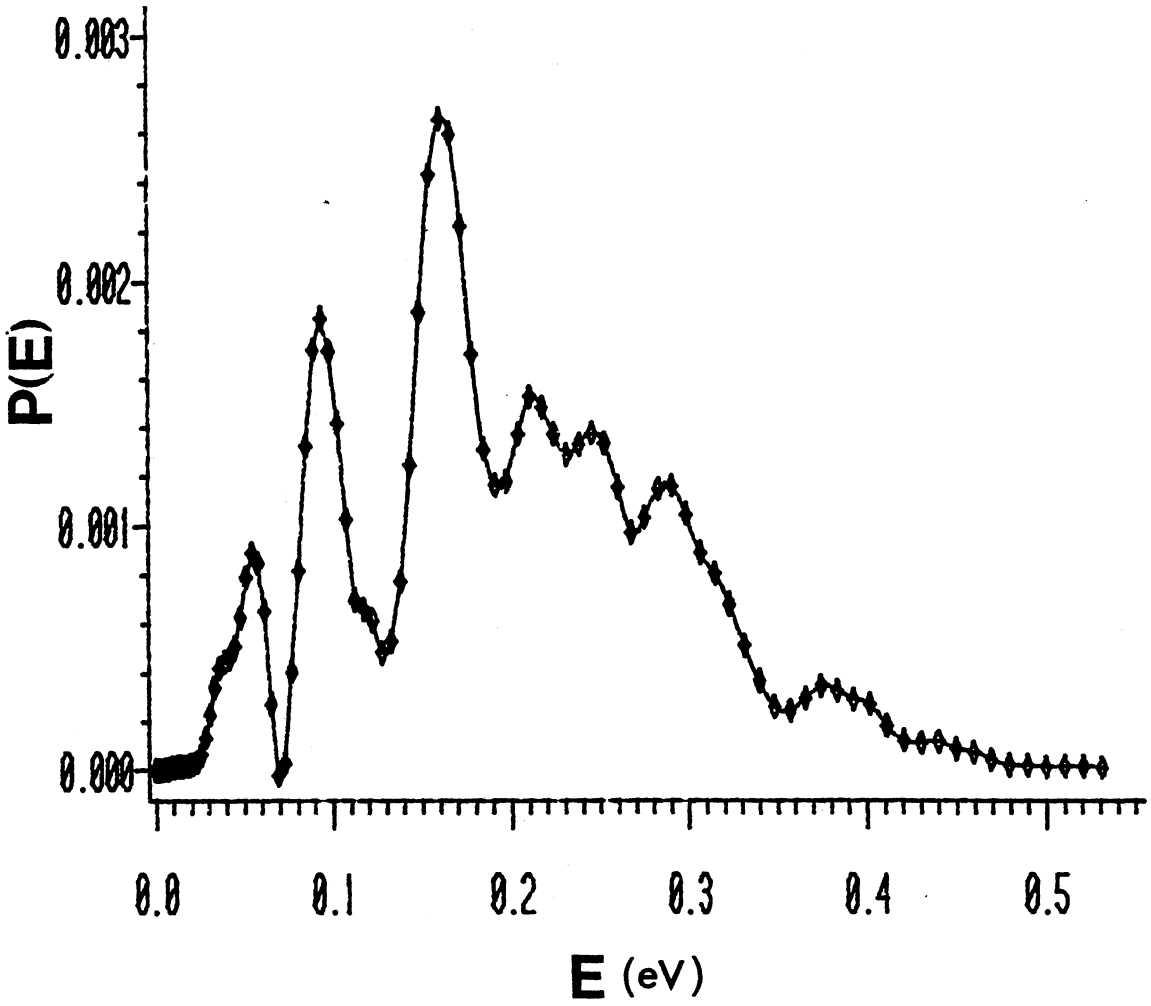

Figure 31. Energy Distribution for $\langle E_i \rangle$ = .089 eV and T_s = 1500 K.

POWER SPECTRUM

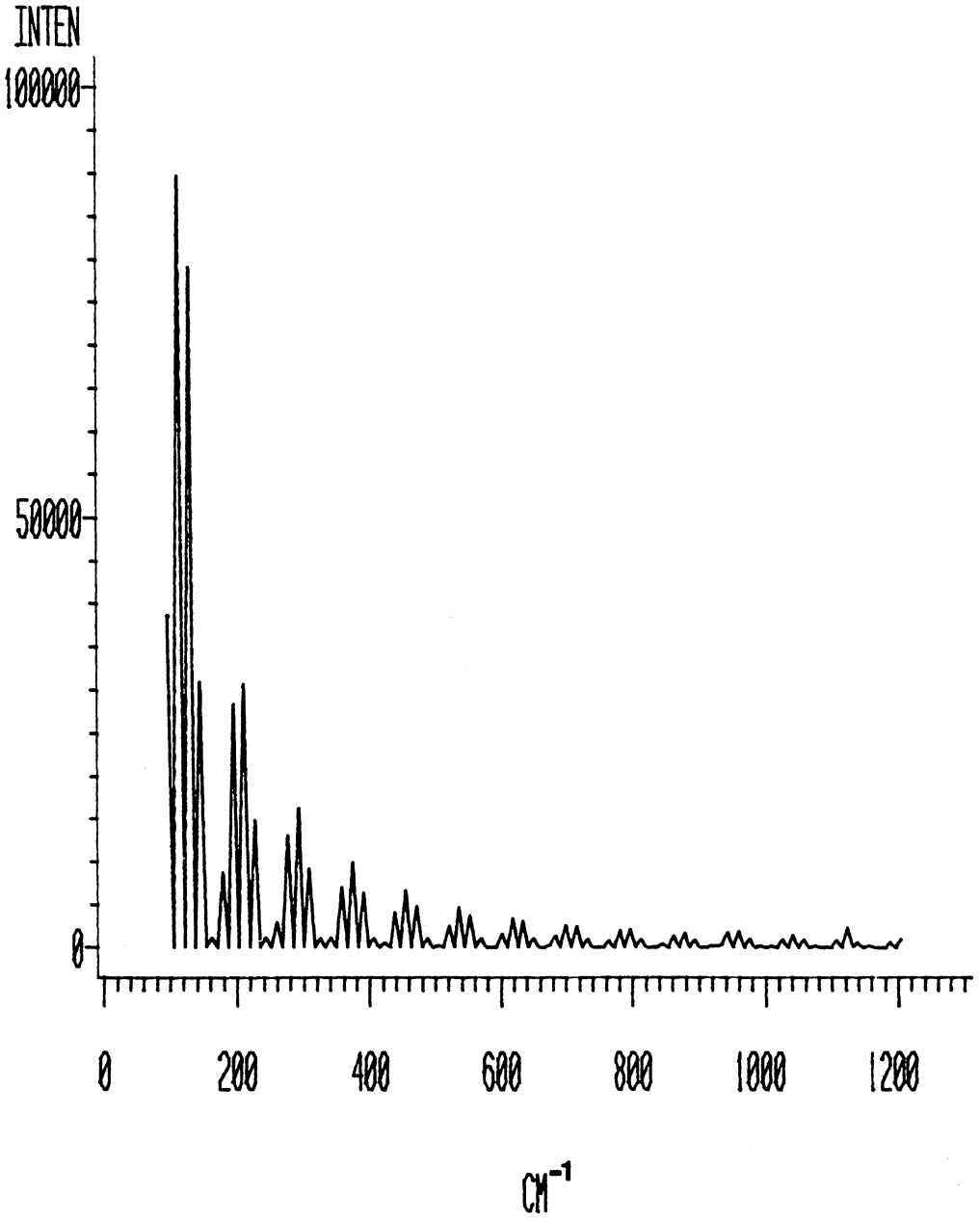

Figure 32. Power Spectrum for One Lattice Bond for T_s = 1500 K.

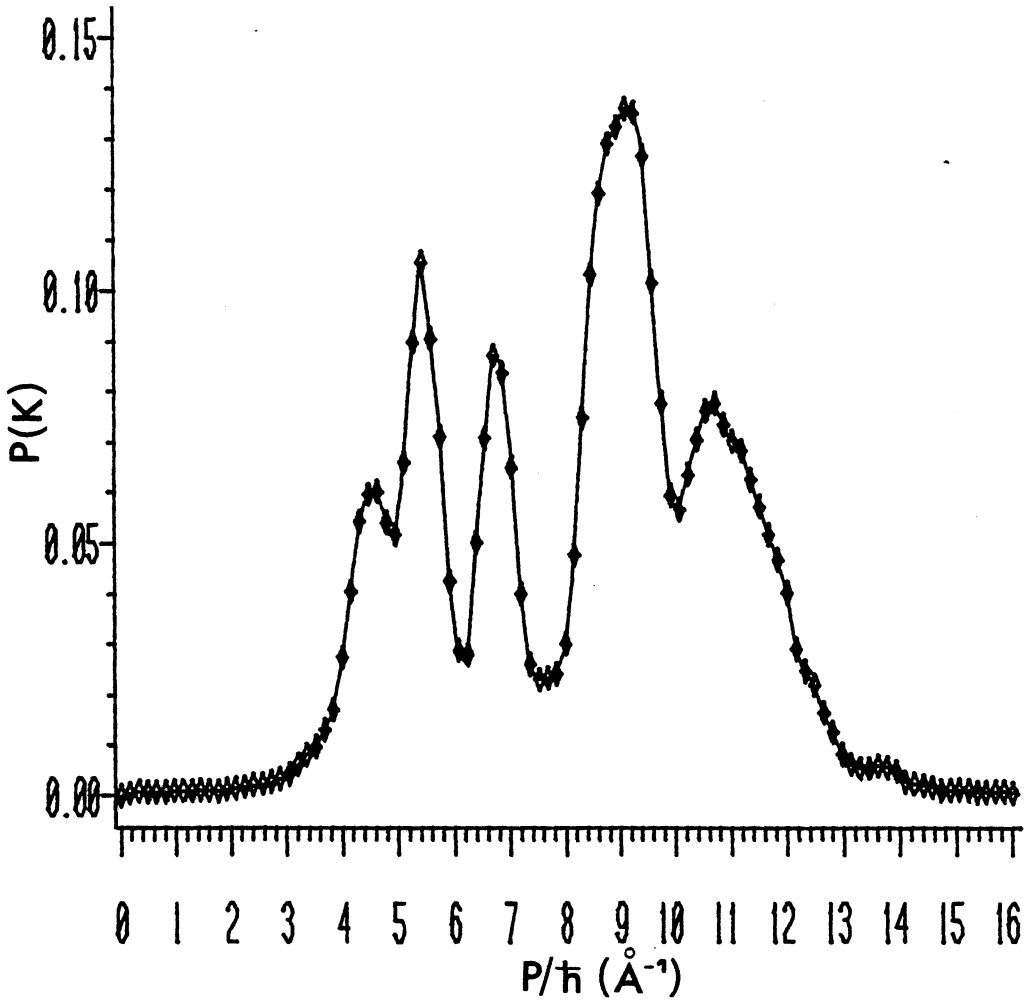

Figure 33. Final-State Momentum Distribution for $\langle E_i \rangle$ = 0.094764 eV, T_S = 1500 K, and Θ_i = 30°.

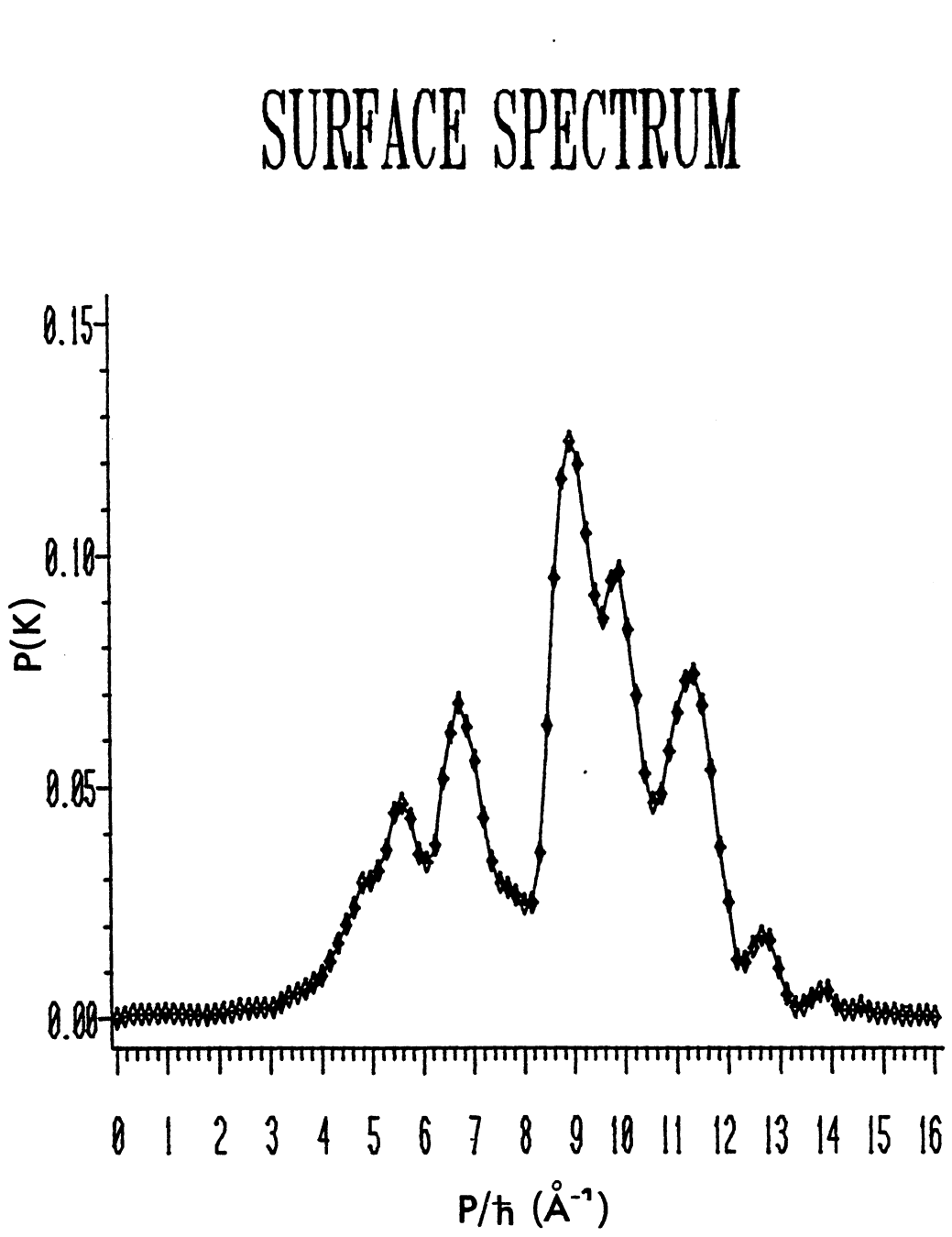

Figure 34. Final Momentum Distribution for $\langle E_i \rangle$ = 0.096647 eV, T_S = 1500 K, and Θ_i = 45°.

MOMENTUM DISTRIBUTION

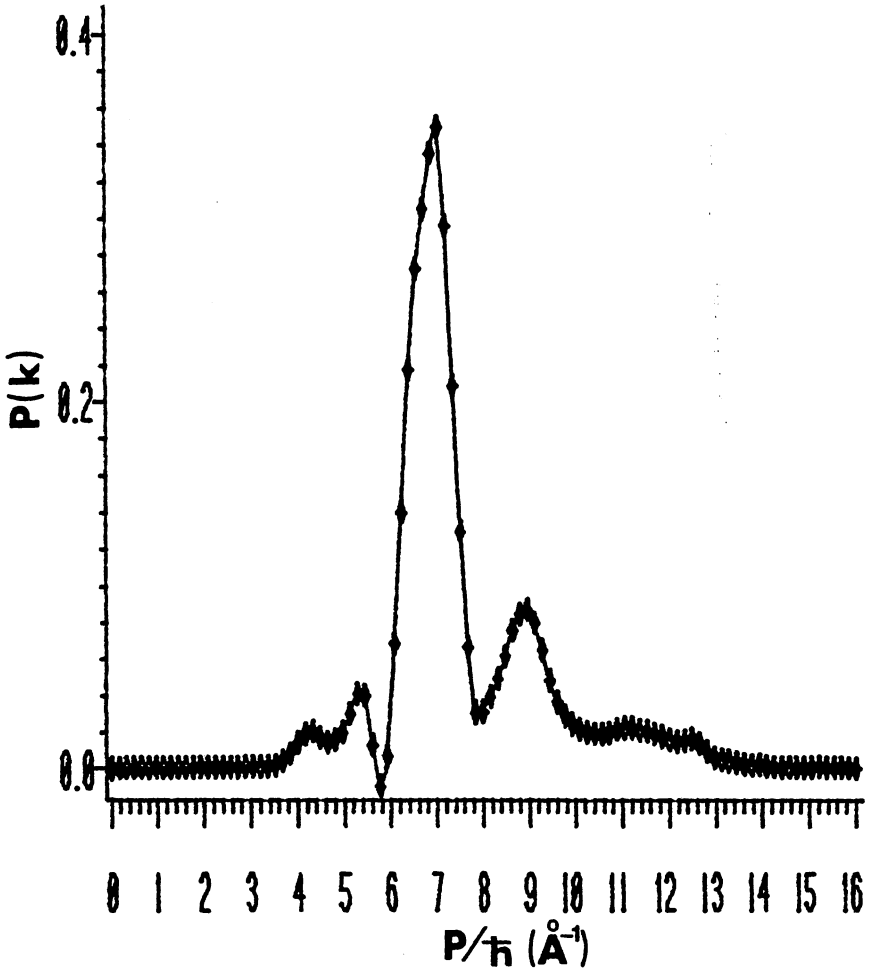

AVERAGE INCIDENT KINETIC ENERGY: .089 eV
SURFACE TEMPERATURE= 300 K
NORMAL INCIDENCE

Figure 35. Final Momentum Distribution for $\langle E_i \rangle$ = 0.089 eV, T_S = 300 K, and $\Theta_i = 0^\circ$.

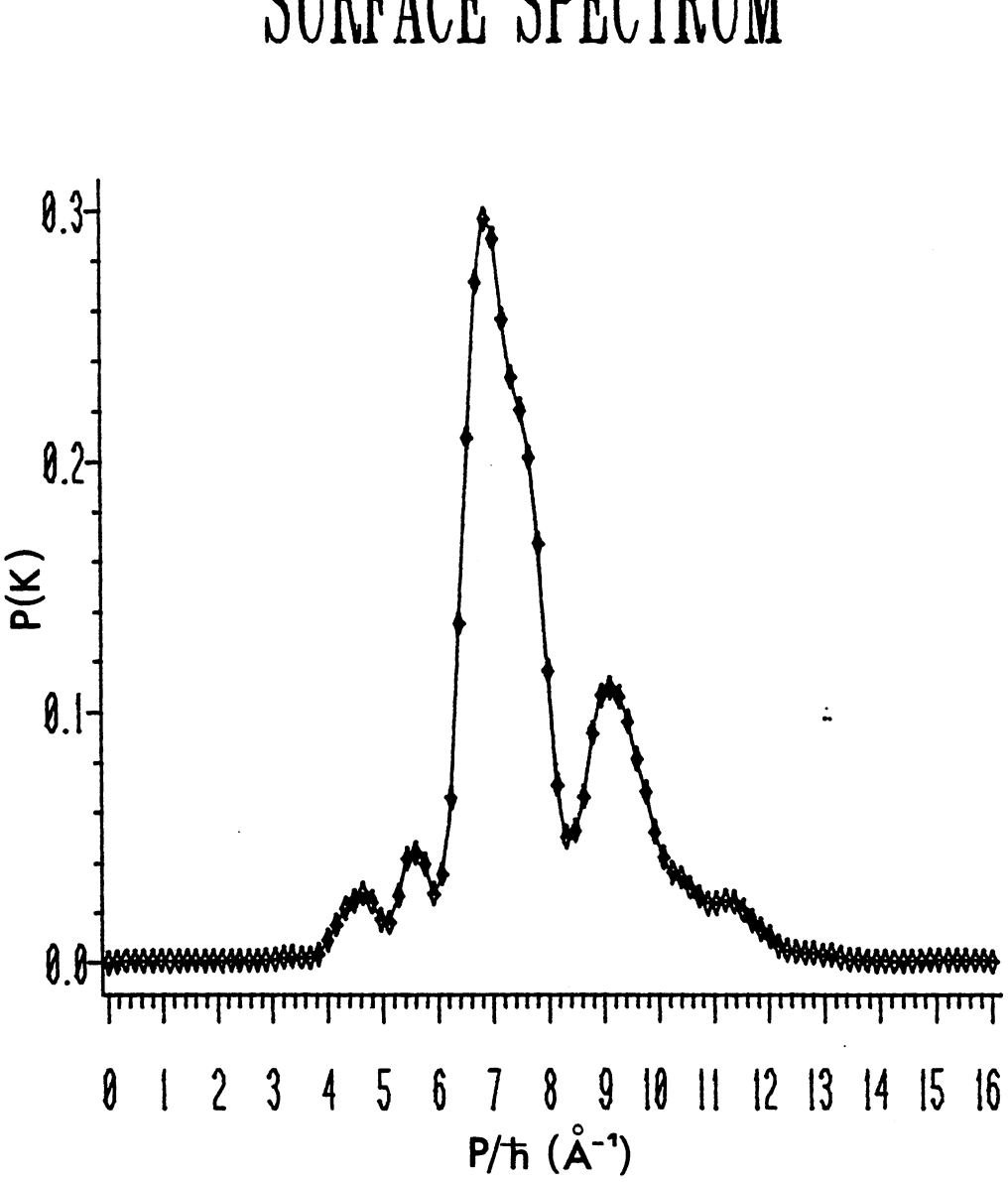

Figure 36. Final Momentum Distribution for $\langle E_i \rangle$ = 0.094764 eV, T_S = 300 K, and Θ_i = 30°

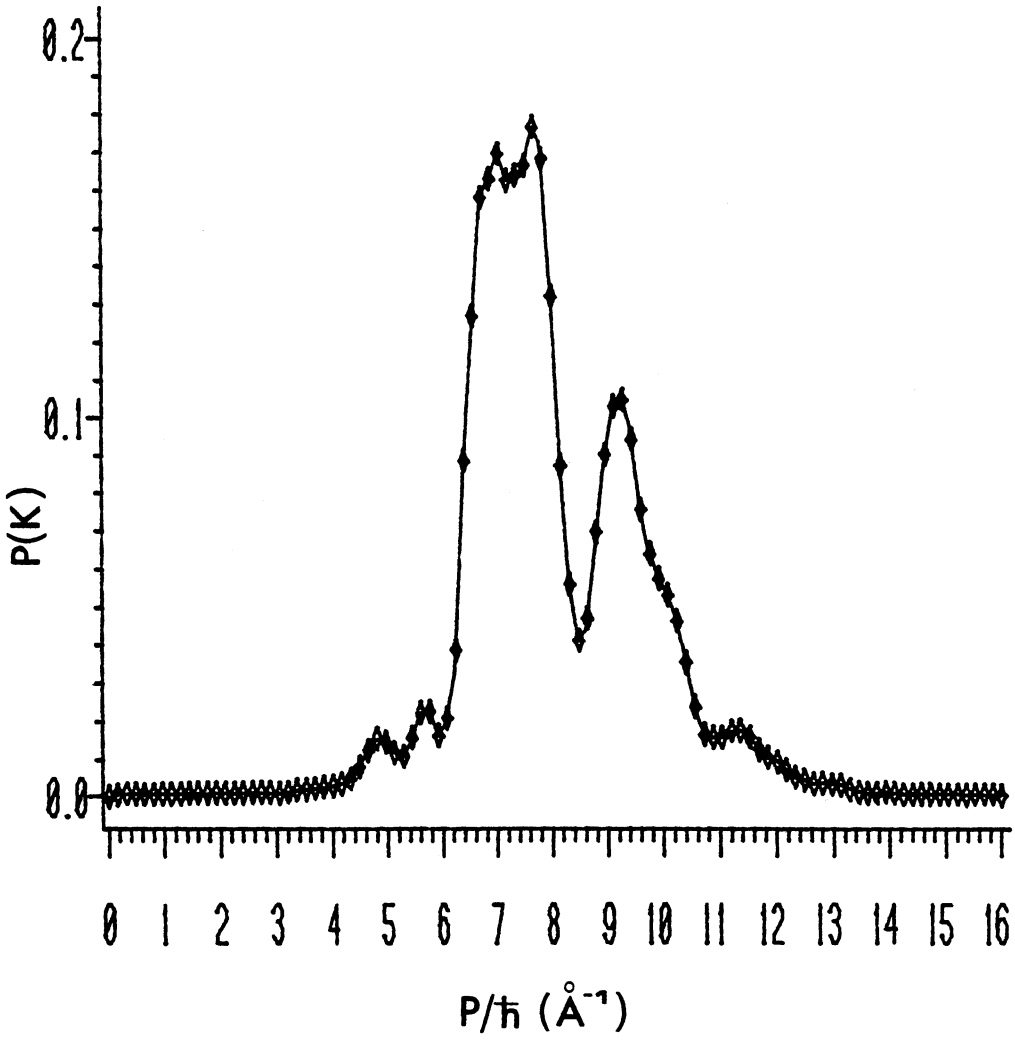

Figure 37. Final Momentum Distribution for $\langle E_i \rangle$ = 0.096647 eV, T_s = 300 K, and $\Theta_i = 45^\circ$.

E. Current Density

Figures 38-43 show the variation of the calculated scattered intensity with scattered angle for incident angles of 0°, 30°, and 45°, at surface temperatures of 300 K and 1500 K. These data were obtained from the probability current density as was described in equation (74). On each of the upper curves, the range θ_j to $\theta_j + \Delta\theta$ is 5°. The lower structure represents the values obtained from a procedure that accounts for a distribution of initial momenta and the Bragg criterion for constructive interference. The data points on the upper curve are the net square amplitudes obtained directly from the current densities and are represented by the small circles, oooo . The line connecting these points was determined using a spline routine.

The criterion necessary for constructive interference is given by

$$\Delta d = C \{ \sin(\theta_i) - \sin (\theta_i + \alpha) \} = n\lambda \qquad (89)$$

where Δd represents the path length difference of 2 parallel portions of the incident wave front. ' α ' is the specular angle and is the difference between the specular angle and a chosen scattered angle. 'C' is the distance between scattering centers on the surface. In order for constructive interference to occur, Δd must be an integral multiple of $n\lambda$, where λ is the wave length of the incident particle. In this model, a distribution of momenta

between 6 and 8 $\hbar$ momentum units was employed. The locations of the maxima on the intensity versus scattered angle plots was checked via the following procedure. A momentum distribution "envelope" was assumed to contain the scattered intensities. The scattered intensities were then recalculated using the envelope of intensities and assuming they were a function of the momentum. The presence of a distribution of momenta was incorporated into the determination of the new square amplitudes as a phase factor in the following expression:

$$I(\Delta\beta) = |A + A\sin(\Delta\beta)|^2 , \tag{90}$$

where is given by

$$\Delta\beta = \Delta d(2\pi/\lambda) . \tag{91}$$

The values of the amplitudes, "A", are those derived from the current densities. The momentum is given by

$$p = h/\lambda \quad \text{or} \quad 1/\lambda = p/\hbar . \tag{92}$$

Then $\Delta\beta$ is given by

$$\Delta\beta = 2\pi\,\Delta\, d(p/h) = \Delta d(p/\hbar) . \tag{93}$$

The momentum distribution employed was

$$P(p)dp = \begin{cases} 0 \text{ for } p/\hbar < 6\ \text{Å}^{-1} \text{ or } p/\hbar > 8\ \text{Å}^{-1} \\ \\ K \text{ for } 6\ \text{Å}^{-1} < p/\hbar < 8\ \text{Å}^{-1} . \end{cases} \tag{94}$$

This was transformed to a distribution of $\Delta\beta$ using

$$d(\Delta\beta) = (\Delta d/\hbar)dp , \tag{95}$$

and

$$p = (\hbar\,\Delta\beta)/\Delta d . \tag{96}$$

Then the distribution over $\Delta\beta$ is given by

$$g(\Delta\beta)d(\Delta\beta) = P(\hbar\Delta\beta/\Delta d)(\hbar/\Delta d)d(\Delta\beta) \ . \qquad (96)$$

The distribution of momenta was normalized using

$$\int_{p_{min}}^{p_{max}} P(p)dp = 1 = \int_{6\hbar}^{8\hbar} Kdp = 2\hbar K \ . \qquad (97)$$

Using this normalization constant, the $\Delta\beta$ distribution becomes

$$g(\Delta\beta)d(\Delta\beta) = \begin{cases} 0 \quad \text{for} \ \Delta\beta < 6\Delta d \ \text{or} \ \Delta\beta > 8\Delta d \\ (1/2\Delta d)(d\Delta\beta) \ \text{for} \ 6\Delta d \leq \Delta\beta \leq 8\Delta d \ . \end{cases} \qquad (98)$$

The new intensities, possessing the enhanced distribution of momenta, were then found by evaluating

$$I(\Theta) = \int_{\Delta\beta_{min}=6\Delta d}^{\Delta\beta_{max}=8\Delta d} (1/2\Delta d)I(\Delta\beta)\{1+\sin(\Delta\beta)\}^2 \, d(\Delta\beta). \qquad (99)$$

The integral can be solved analytically and gives the expression

$$I(\Theta) = (I(\Delta\beta)/2\Delta d)\{3\Delta d - 2[\cos(8\Delta d)-\cos(6\Delta d)] - (1/4)[\sin(16\Delta d)-\sin(12\Delta d)]\} \qquad (100)$$

The results obtained from the above procedure are included on the plots showing the variation of scattered intensity with scattered angle. The data points obtained by this procedure are represented by the small diamonds. The line connecting these data was obtained using a spline routine.

In Figures 38-43, the "envelope" of chosen amplitudes was taken directly from those calculated from current densities, including the structure. A second amplitude envelope containing no structure was also used so that the peak locations could be determined without a structural bias. The multiplicative factor, $I(\Delta\beta)$, in this case does not include Debye-Waller broadening due to surface motion. The result of this calculation is shown in Figure 44. The upper curve, represented by the small circles, -oooo-, is the envelope of chosen square amplitudes where no structural features are present. The lower curve, represented by the small diamonds, is the data obtained from Equations 90-100 using the structureless envelope. The actual intensities obtained directly from the probability current densities and the peak locations obtained using the structureless envelope are compared in Figure 45. The actual data and the values obtained by the structureless envelope are represented by the small circles —oooo— and the small diamonds, ♦♦♦ respectively. The lines connecting the data, in each case, are spline fits, and the results are scaled with multiplicative factors to allow simultaneous displayal on one plot. The peak positions are found to be in good

agreement. This tendency suggests that application of the model to real systems should produce good correlation between predicted diffraction structure and experiment. The intensities determined from the structureless envelope also exhibit less Debye-Waller broadening due to the neglect of surface motion.

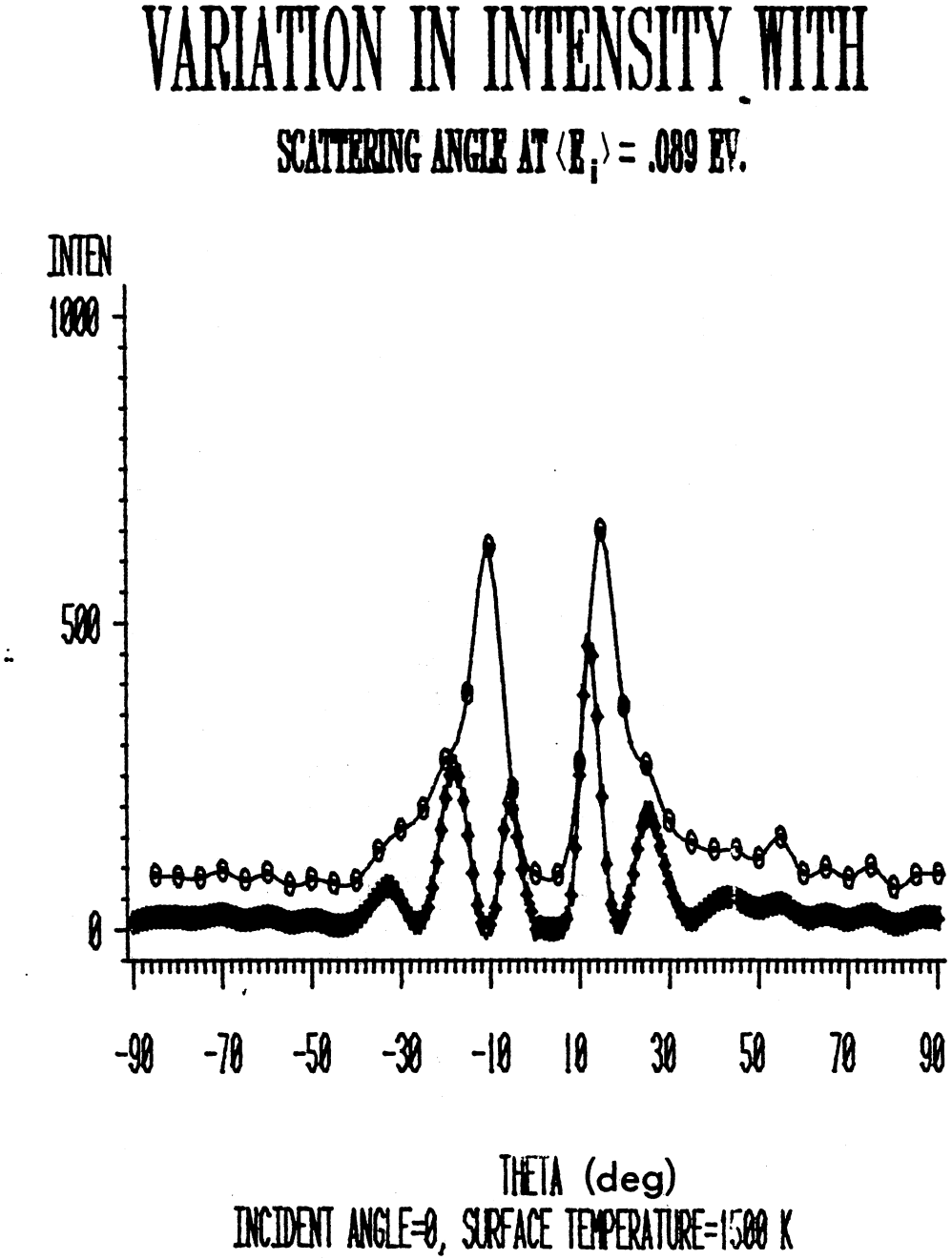

Figure 38. Variation of Scattered Intensity with Scattered Angle for Normal Incidence and T_s = 1500 K.

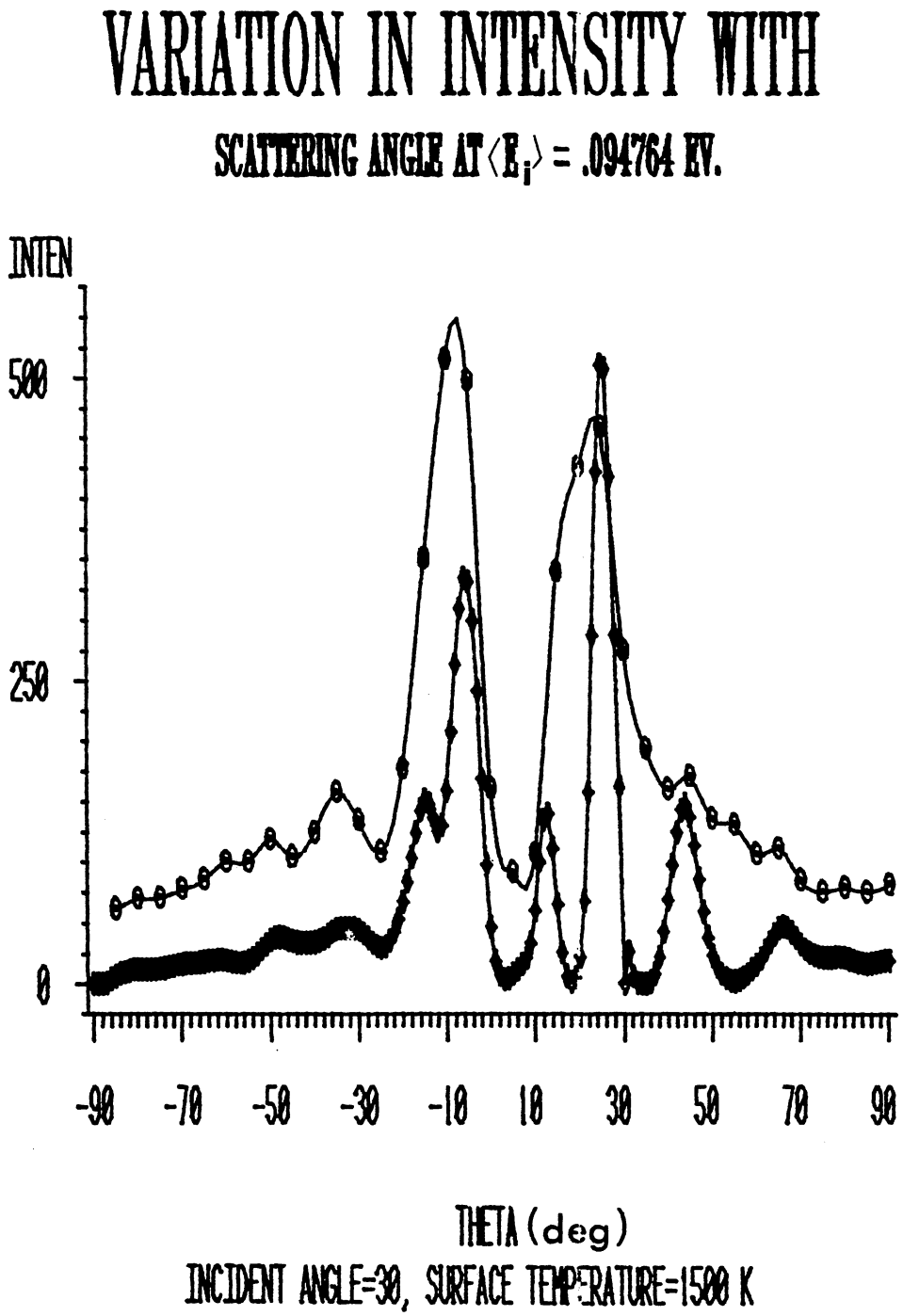

Figure 39. Variation of Scattered Intensity with Scattered Angle for $\Theta_i = 30^o$ and T_s = 1500 K.

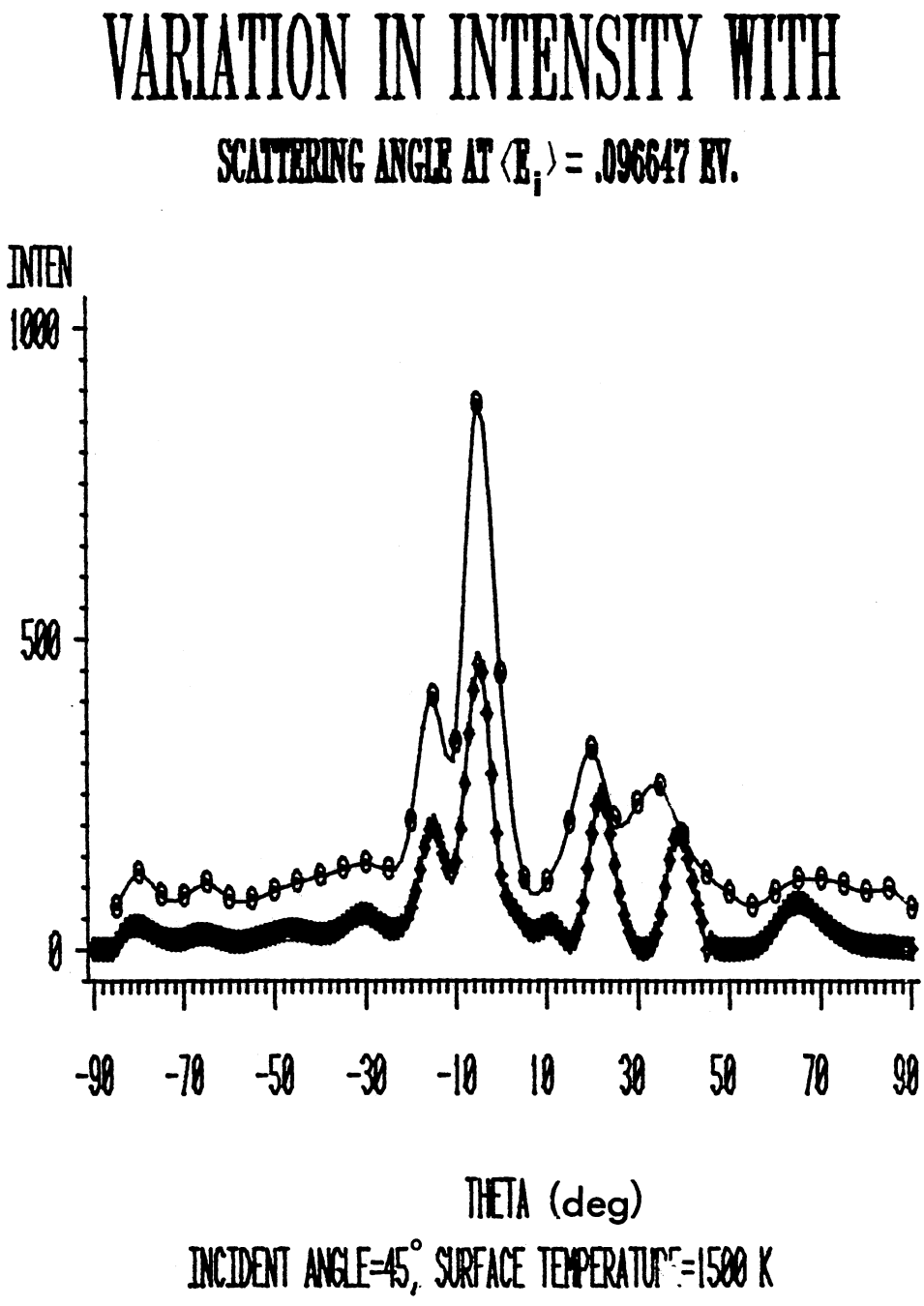

Figure 40. Variation of Scattered Intensity with Scattered Angle for $\Theta_i = 45°$ and $T_S = 1500$ K.

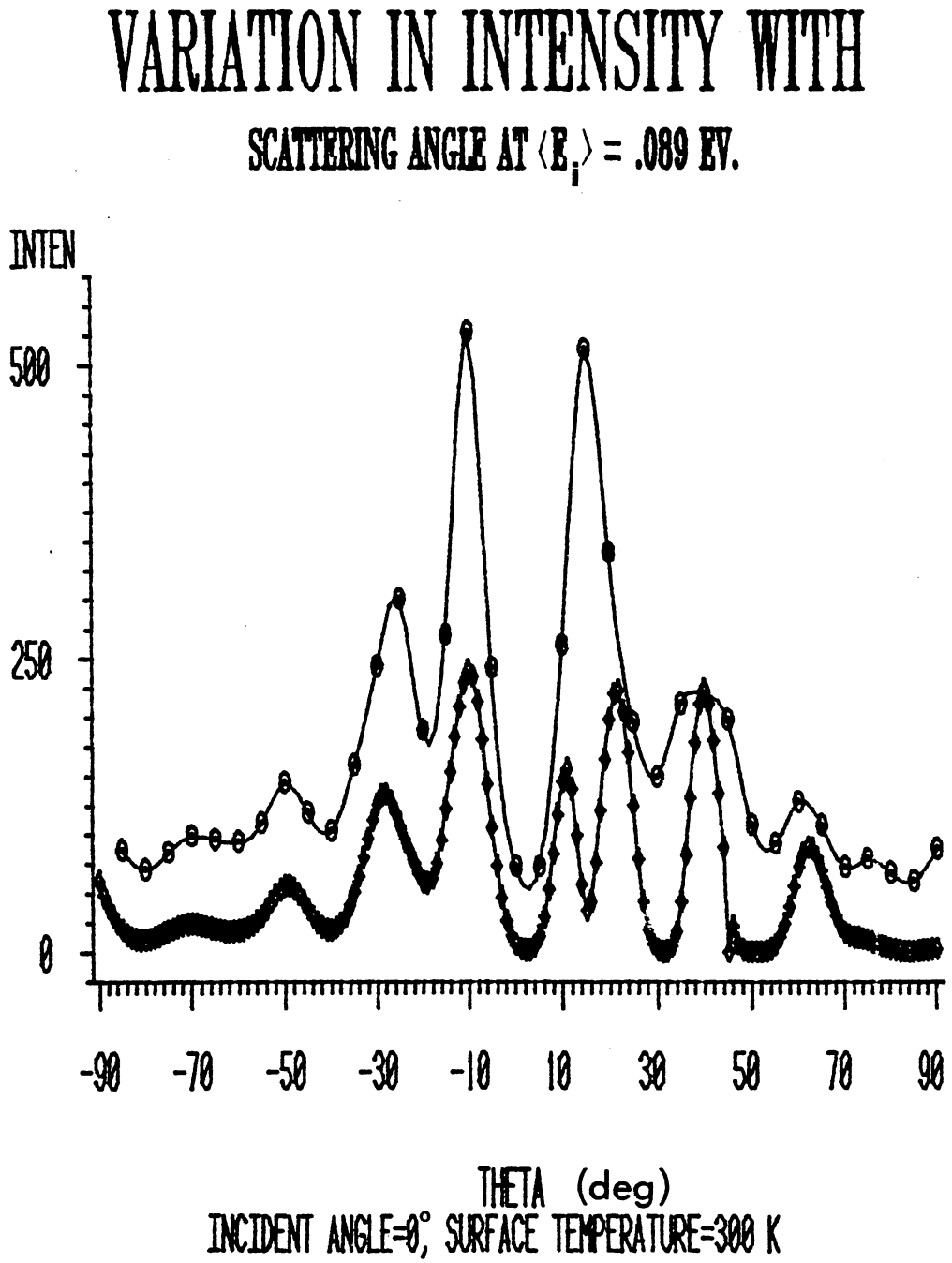

Figure 41. Variation of Scattered Intensity with Scattered Angle for Normal Incidence and T_S = 300 K.

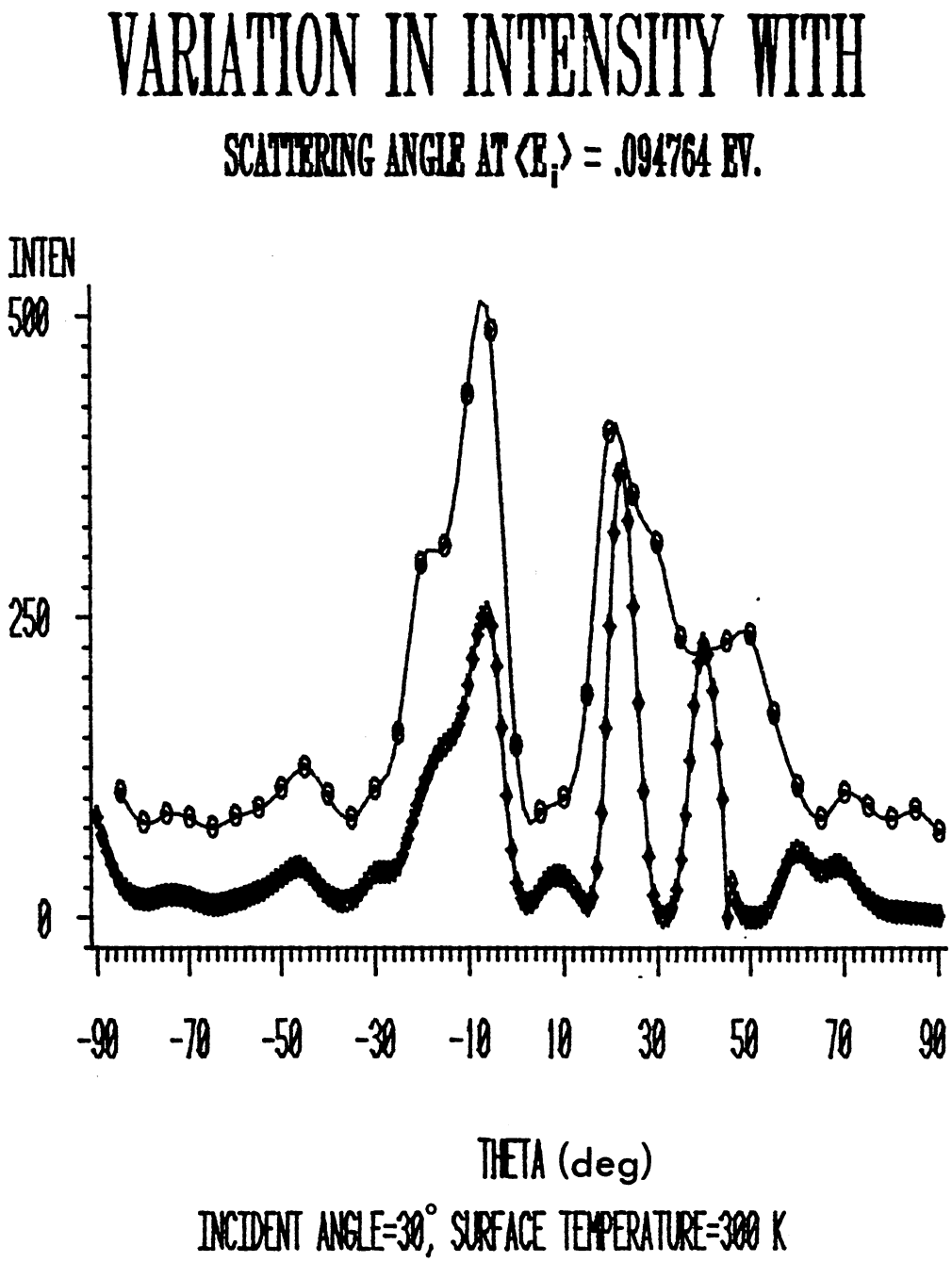

Figure 42. Variation of Scattered Intensity with Scattered Angle for $\Theta_i = 30°$ and $T_S = 300$ K.

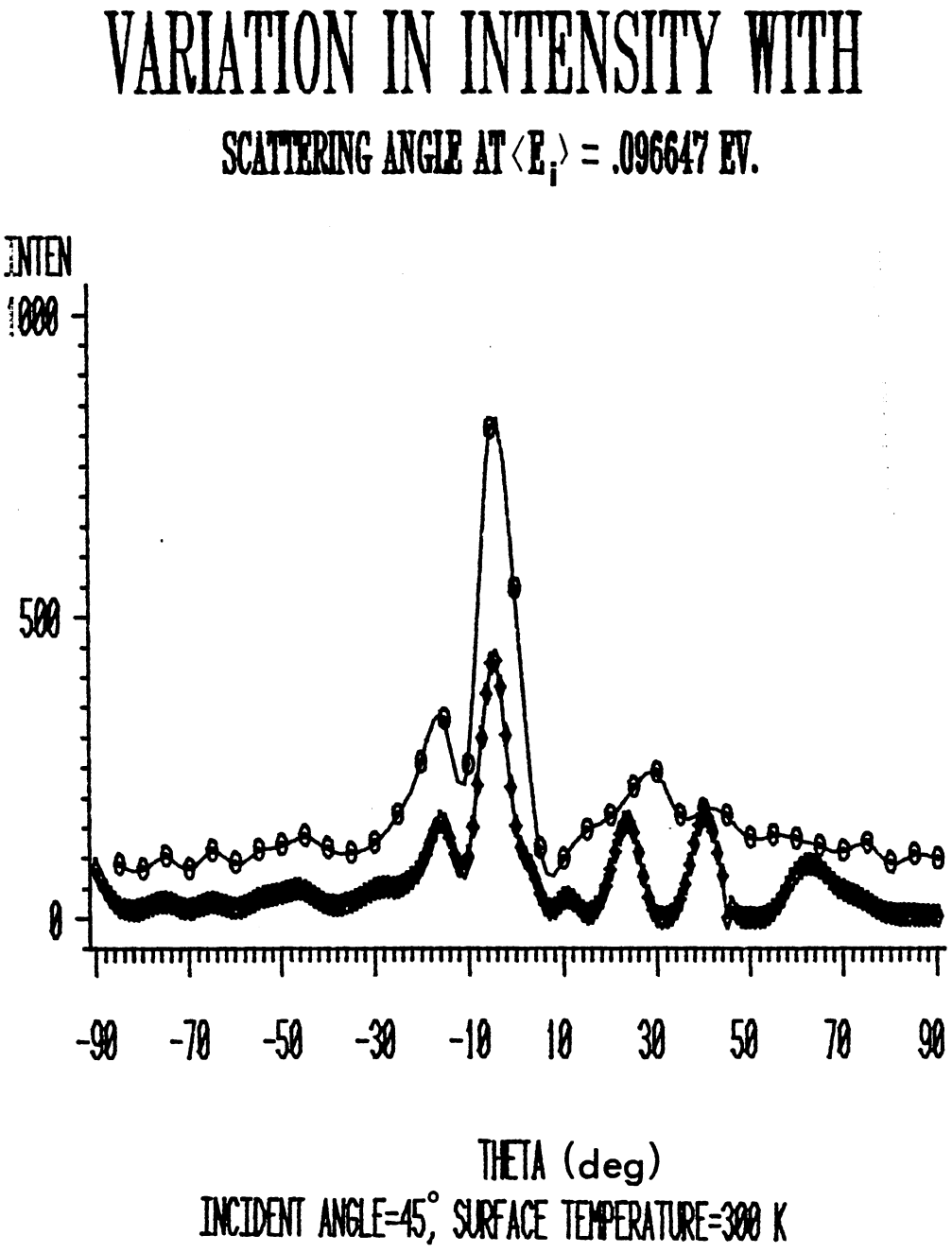

Figure 43. Variation of Scattered Intensity with Scattered Angle for Θ_i = 45° and T_S = 300 K.

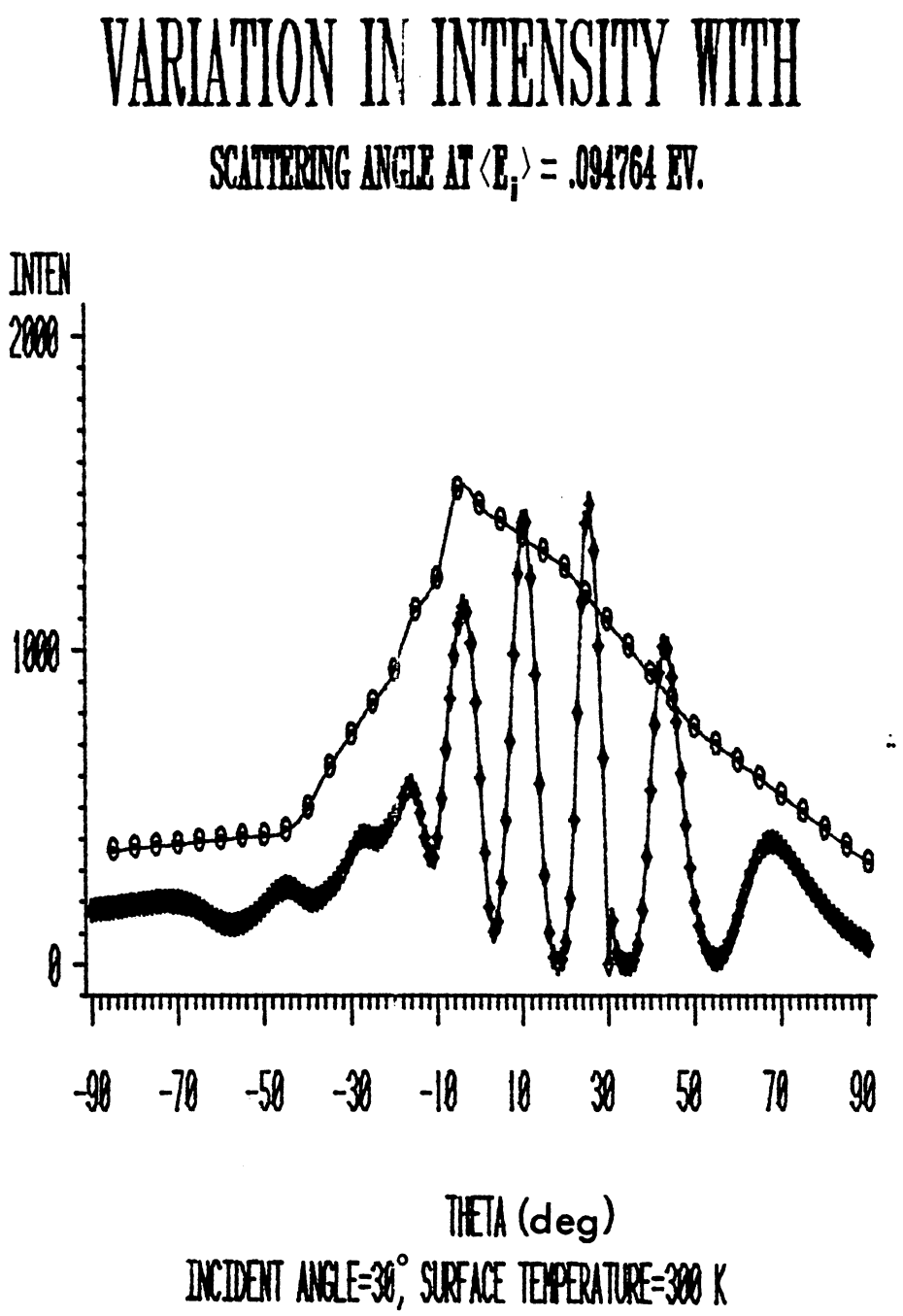

Figure 44. Variation of Scattered Intensity with Scattered Angle as Predicted by a Structureless Envelope of Intensities; for $\Theta_i = 30^\circ$ and $T_S = 300$ K.

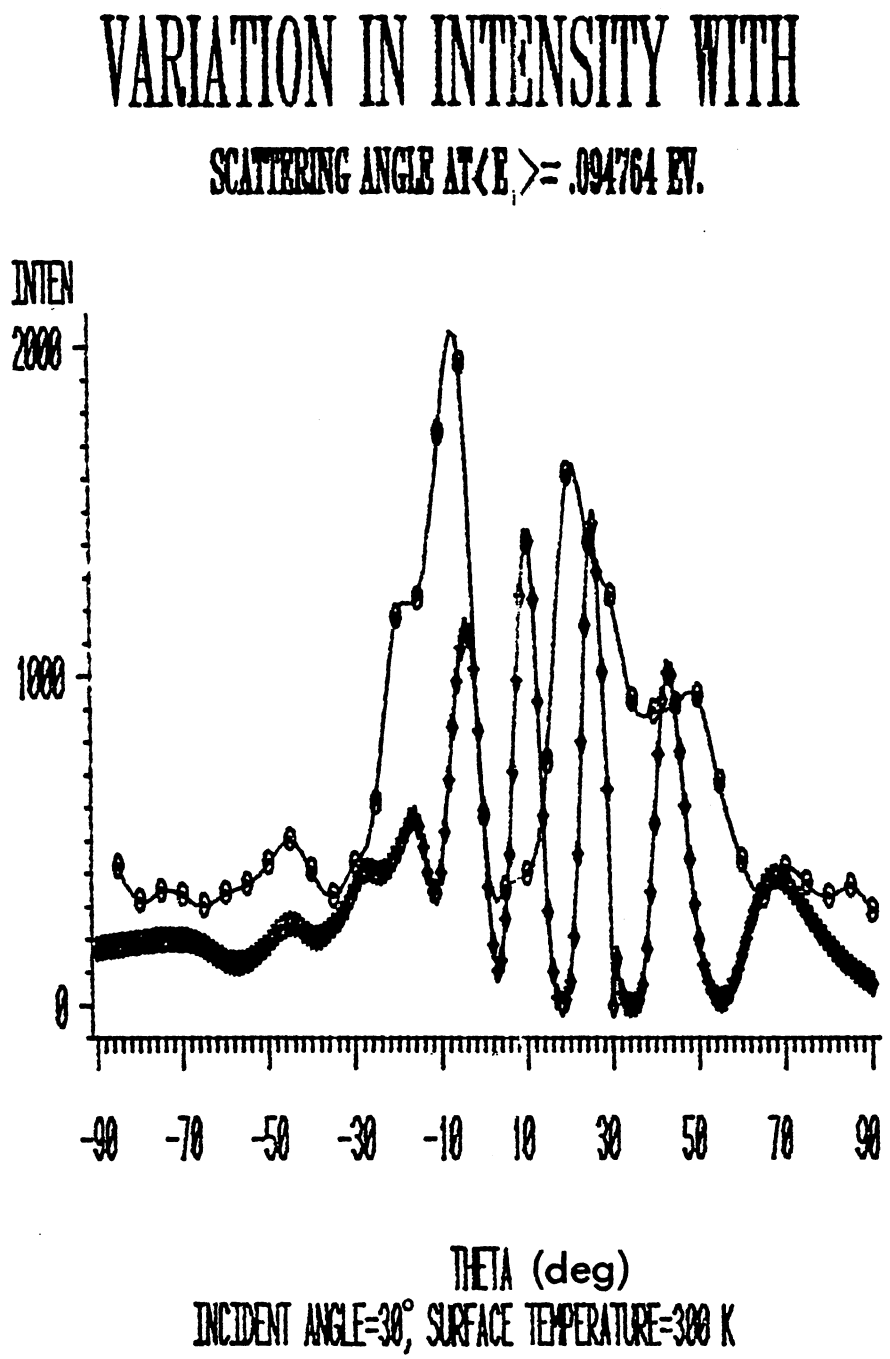

Figure 45 Comparison of the Variation of Scattered Intensities with scattered Angle as Predicted by Wave Packet Current Densities and by a Structureless Envelope; for $\Theta_i = 30^\circ$ and $T_S = 300$ K.

F. Debye-Waller Factor

The Debye-Waller Factor, DWF, was determined via Equations 76-79. The variation of the DWF with surface temperature is shown in Figure 46. The Debye-Waller Factor is a measure of the elastic scattering intensity, and should be large when the surface atoms are stationary. As the surface temperature increases, the DWF should decrease. As the surface temperature increases, the motion of the surface atoms increases and the scattering becomes less and less elastic; the scattering distributions become broader. A decrease in the DWF with increasing surface temperature is exactly what is predicted by the model. Weinberg (72) has determined the DWF for several experiments where helium was scattered from solid surfaces. Debye-Waller Factors were determined using

$$DWF = \exp(-24DT_S \mu^*/k\theta_{D,S}^2) \quad , \tag{101}$$

where the mass ratio, μ^* , is given by

$$\mu^* = m/M \quad , \tag{102}$$

and D, $\theta_{D,S}$, T_S , and k are the gas-surface potential well depth, the surface Debye temperature, the surface temperature, and the Boltzman constant, respectively. Debye-Waller factor values have been calculated, by Weinberg (72), via Equation (101) for systems that have been studied experimentally. Some of these are shown in Table III. Weinberg has also calculated the DWF for several metal surfaces at T_S = 375. Some of these are shown in Table IV.

TABLE III

CALCULATED DEBYE-WALLER FACTORS FOR SELECTED EXPERIMENTAL SYSTEMS

Surface	$\theta_{D,S}$(K)	T_S (K)	DWF
W(112)	180	1300-1900	0.043-0.010
W(110)-R(3x5)	1230	375-1300	0.78-0.43
Ni(111)	220	700	0.029
LiF(001)	508	300	= .24

TABLE IV

CALCULATED DEBYE-WALLER FACTORS FOR METAL SURFACES AT T_S = 375 K

Surface	$\theta_{D,S}$(K)	DWF
W	180	0.404
Ni	220	0.150
Au	102	0.071

A decrease in the value of the DWF with increasing surface temperature is clearly evident from the data shown for W(112) and W(110)-r(3x5) of Table III. From Figure 46, a value of .75 is obtained for the DWF at T_S = 375 K. This value is quite large compared to those of Table IV. This can be understood when the lattice force constant for the model calculation is considered. The surface Debye temperature is determined form the lattice force constant via

$$\theta_{D,S} = h\nu/k = (h/k)(k_F/\mu)^{1/2} , \qquad (103)$$

where k_F is the force constant of the bond. The force constant for the model system was assumed to be 5.36 eV/Å^2. The surface Debye temperature was then found to be $\theta_{D,S} \cong 549$ K. The surface Debye temperature is therefore more than twice that of any of the surfaces noted in Table IV. Equation (101) shows that this difference will result in a significantly larger value for the DWF. In the model case, the high force constant, which leads to a similarly large DWF, indicates a rather stiff lattice.

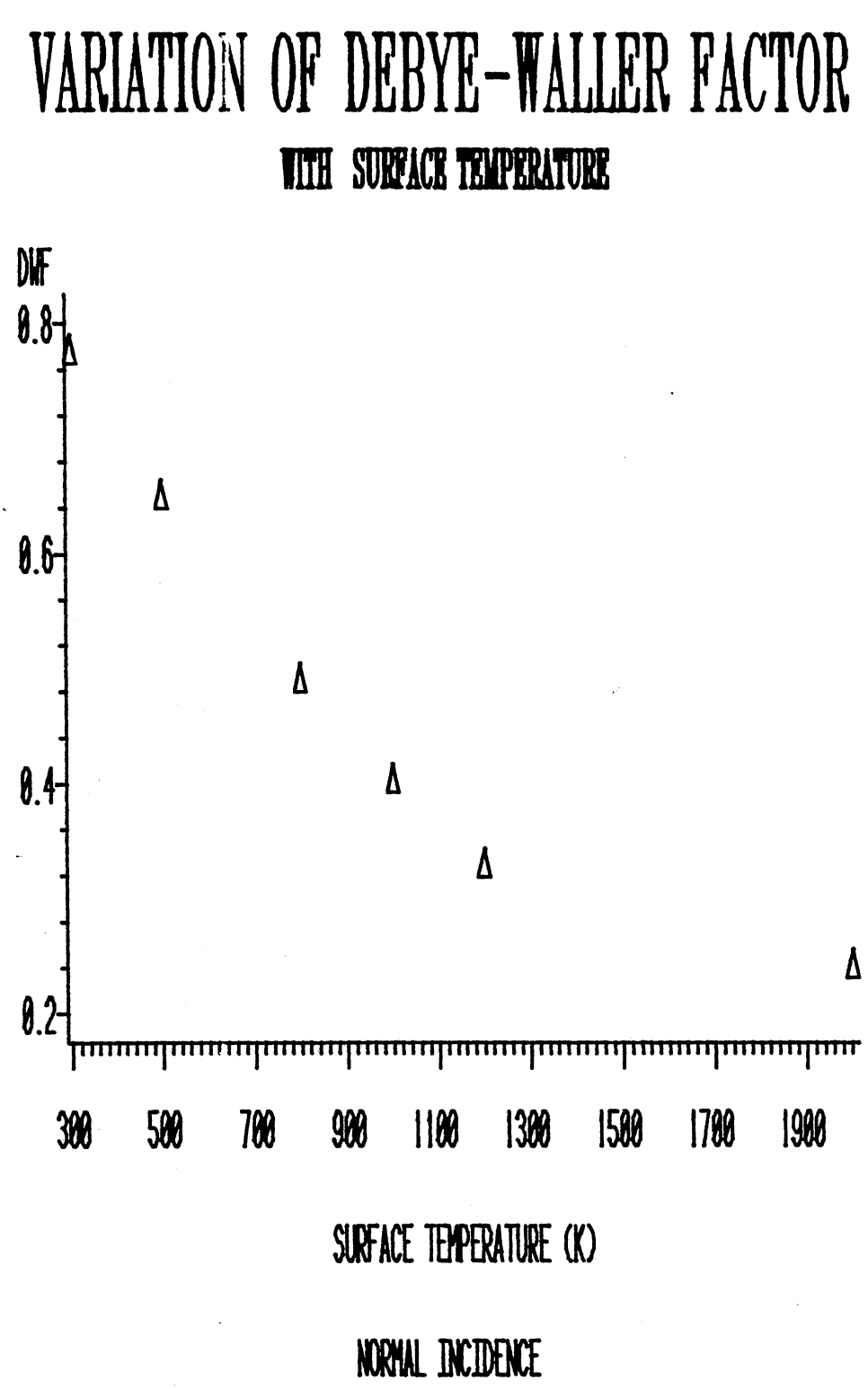

Figure 46. Variation of Debye-Waller Factor with T_s.

CHAPTER IV

He-LiF GAS-SURFACE STUDY

A. Introduction

In this chapter, application of the model developed in Chapter III will be made to the He-LiF system. Changes in the atomic masses and arrangement of atoms will be described. There will be a description and implementation of a previously tried Lennard-Jones potential. A slight variation in the incident beam energy will be invoked and the reasoning for this procedure will be given. Finally, results and comparisons with previous experimental and theoretical work will be described.

B. LiF Surface

The atomic arrangement of the LiF surface is shown in Figure 47. The lithium atoms are assigned a mass of 6.941 amu while the the fluorine atoms and are given a mass of 18.9984 amu. The nine movable atoms are arranged in the geometry of a small portion of a (001) face of a LiF crystal. The harmonic force constant between Li^+ and F^- ions was estimated from the frequency of the longitudinal optical phonons of thin films, 675 cm^{-1} , as per D. W. Berreman (80). The value obtained was 8.592 $eV/\mathring{A}^2$. The

positions of the lattice atoms as a function of time were then determined via Hamilton's Equations as was done in the model calculation.

C. He-LiF Potential

The interaction potential was assumed to be a sum of pairwise Lennard-Jones (6,12) potentials as given in Equations 45 and 46. The Lennard-Jones parameters for the pairs He and Li^+ , and He and F^- , have not been obtained. Therefore they were extimated by replacing Li^+ with He and F^- with Ne and using the combination rule as in Equations 80-81. The Lennard-Jones parameters for the system are given in Table V.

TABLE V.

LENNARD-JONES PARAMETERS for He-LiF SYSTEM

Molecule or Atom	σ(A)	ϵ/k (K)
He	2.88	10.8
Ne	3.09	35.8
He-Ne	2.985	19.66

The He and Ne parameters were obtained from second cluster integrals (81) and were employed previously by Tsuchida (49) in early He-LiF scattering studies. The potential energy contours for the He/LiF interaction are shown in Figure 48.

D. Evolution of the He Wave Packet

In order for the second order difference method to be stable, it was determined that the approximate grid spacing on an equally spaced mesh must be less than or equal to one fourth of the average particle wavelength. Hence the "average energy" of the wave packet was reduced to .0232 eV, a change by a factor of one fourth. This procedure then required a factor of 4 increase in the number of time steps necessary for scattering calculations. The remainder of the wave packet evolution was unchanged from the model calculation.

E. Results

The scattered probability distributions for $\langle E_i \rangle$ = .0232 eV, T_S = 1500 K, and normal incidence are given in Figures 49-51 for 3125,3750,and 5000 time steps. The buildup of a diffraction pattern is visible along both the y and the z directions, and is more evident than that predicted in the model calculation. The momentum distributions at time-step 4375 for T_S = 300 K and T_S = 1500 K at $\Theta_i = 0^\circ$ are shown in Figures 52 and 53. In both cases, the scattering appears to be very elastic. A broader, more

structured distribution for the higher surface temperature would be more consistent with the trends predicted by the model in Figures 29,30, and 33-37. The variations of $\langle E_e \rangle$ with T_S , α_E with T_S , and the EAC with T_S are shown in Figures 54-56, respectively. The trend suggested by Figures 54 and 55 is aphysical and hints of a breakdown in the capabilities of the model. The breakdown was first suggested by the unusual behavior of the momentum distribtuion and is attributed to near violation of the wavelength stipulation mentioned previously. The average exiting energy of the gas atom should increase with increasing surface temperature, in compliance with the behavior predicted by the model in Figures 16-18. Figure 54 predicts a decrease in $\langle E_e \rangle$ with increasing surface temperature. Similarly, the value of the energy transfer coefficient, α_E , should decrease with increasing surface temperature, as was predicted by the model in Figure 23. Figure 55 suggests an increase in α_E with T_S. Figure 56 shows that the behavior of the EAC is predicted to be much like that found in the model calculation, Figures 25, 27, and 28. The behavior of the $\langle E_e \rangle$ versus T_S and α_E versus T_S casts some doubt however, upon the reliability of the EAC plot. Figure 57 shows the variation of scattered intensity with scattered angle. The small circles, —oooo— , represent the raw data obtained from the wave packet calculation. The small diamonds represent the data obtained when a structureless envelope of square amplitudes was

treated via Equations 90-100. The resulting locations of the scattered peaks are internally consistent and are in relatively good accord with the scattering data of Boato, Cantini, and Mattera (82).

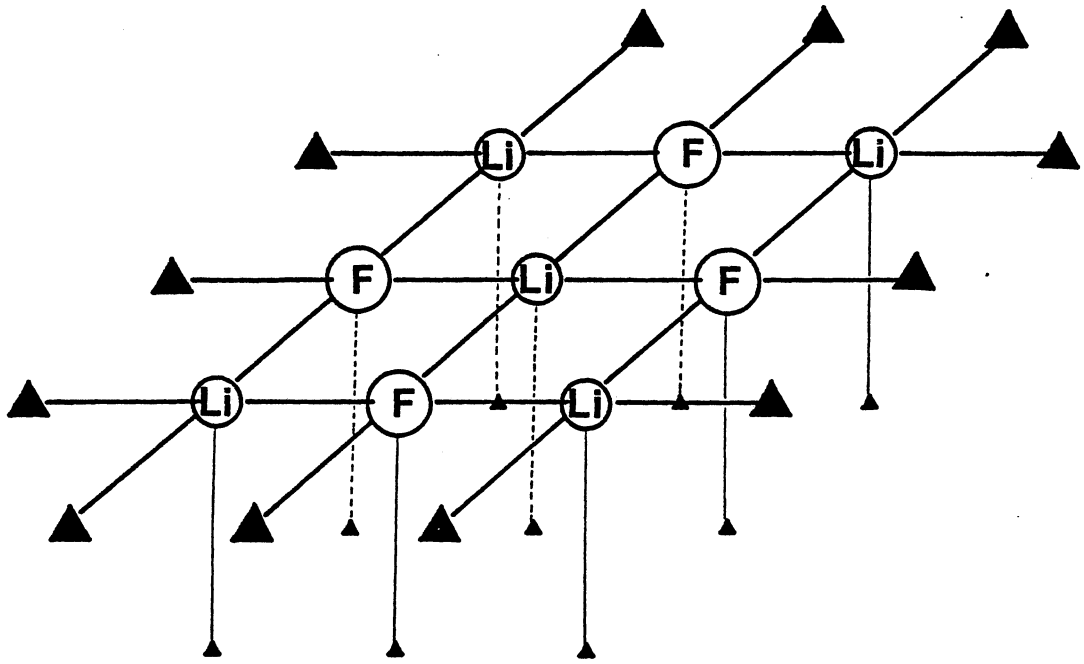

Figure 47 LiF Atomic Arrangement

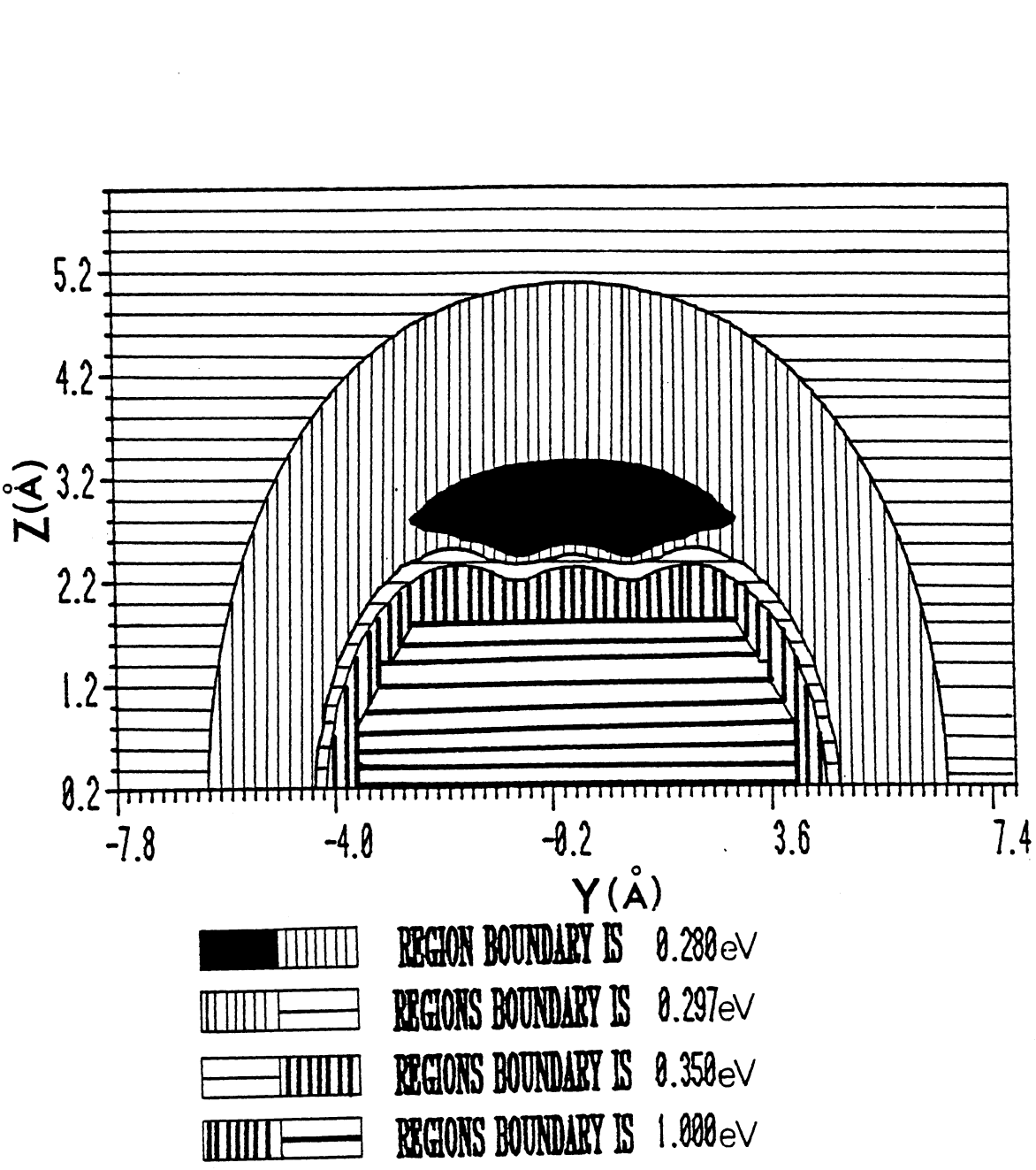

Figure 48. He/LiF Potential Energy Surface.

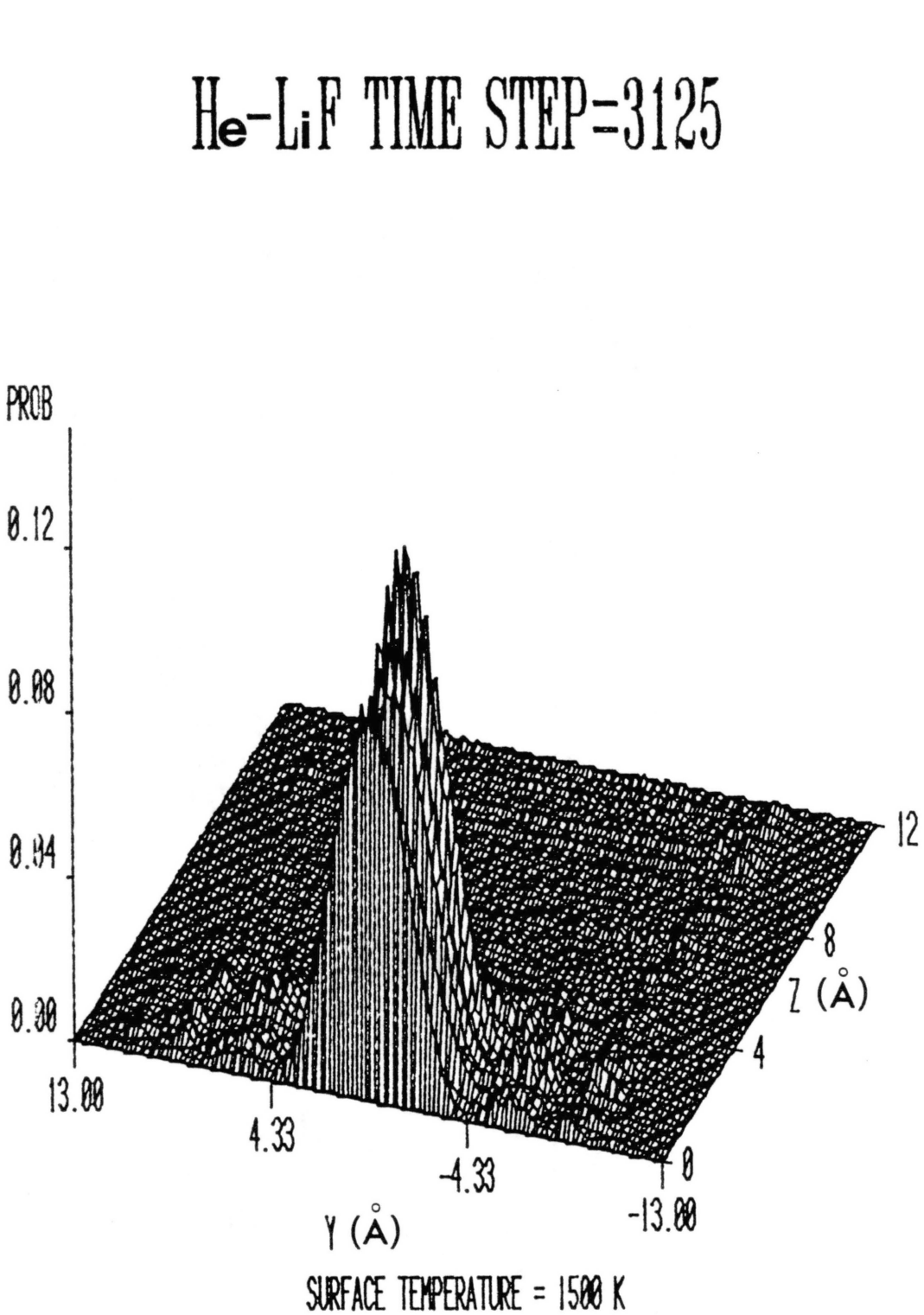

Figure 49. Final-State Probability Density for $\Theta_i = 0^\circ$, T_S = 1500 K and Time Step 3125.

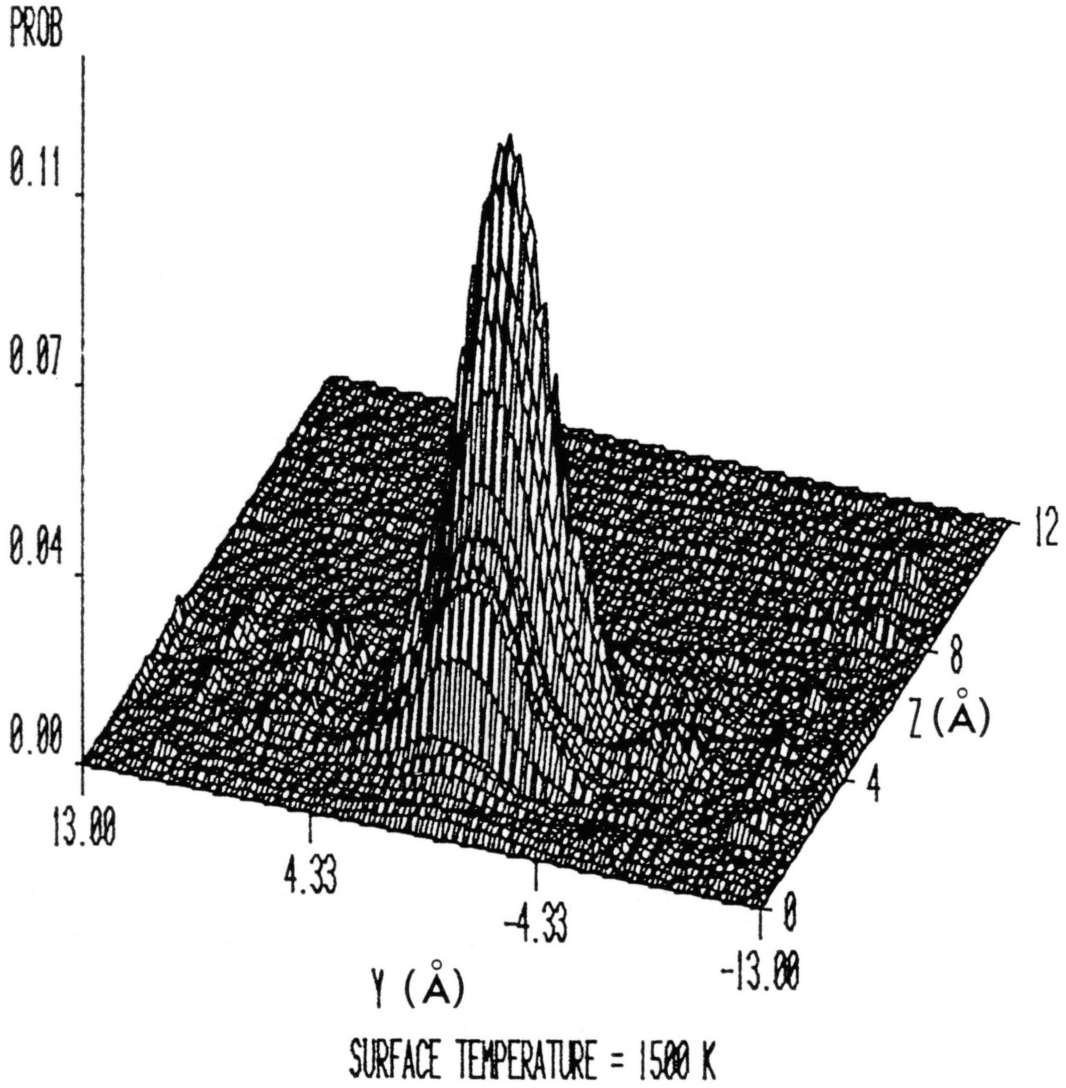

Figure 50. Final State Probability Density for $\Theta_i = 0^\circ$, T_S = 1500 K and Time Step 3750.

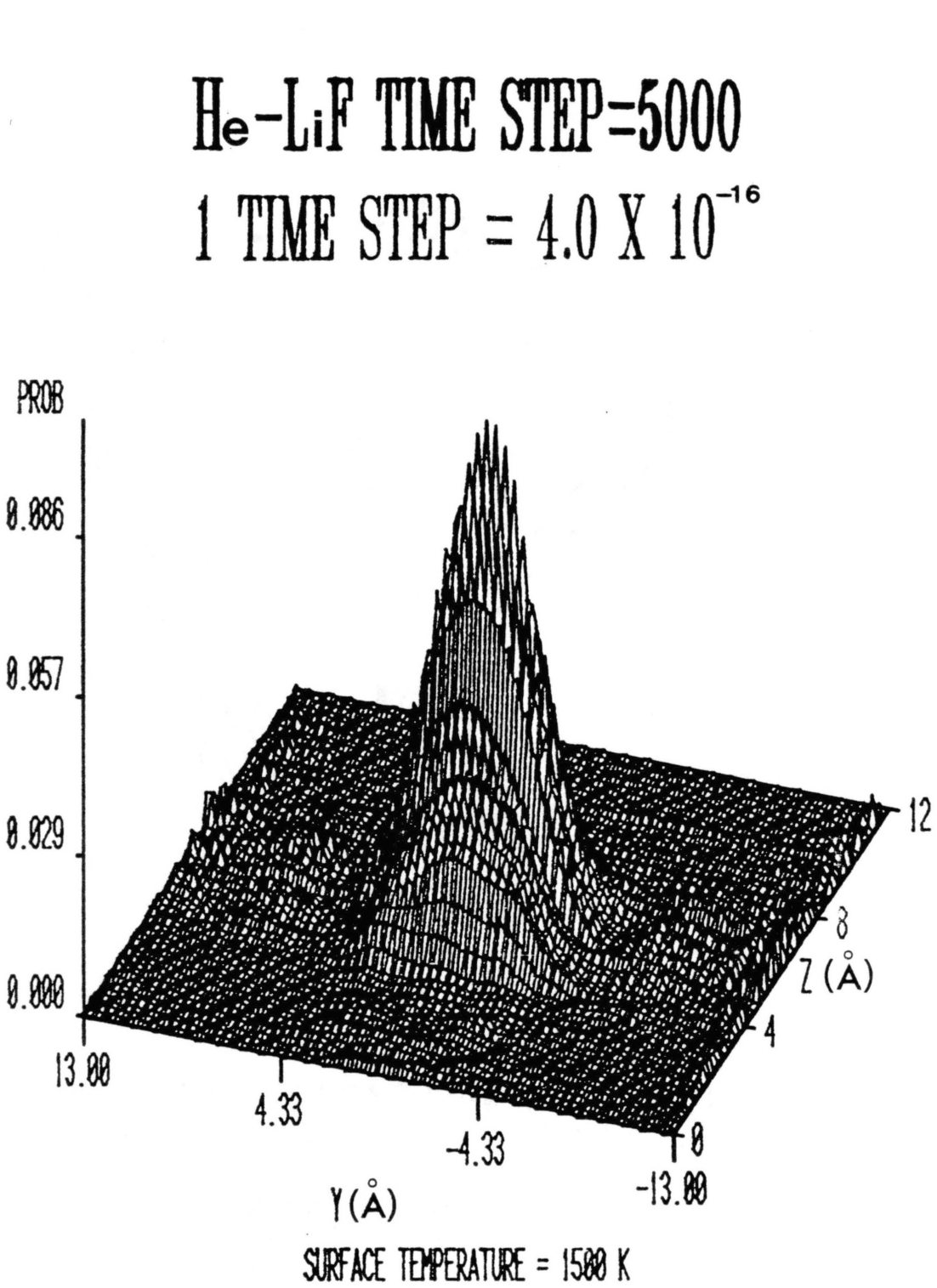

Figure 51. Final State Probability Density for $\Theta_i = 0°$, T_s = 1500 K and Time Step 5000.

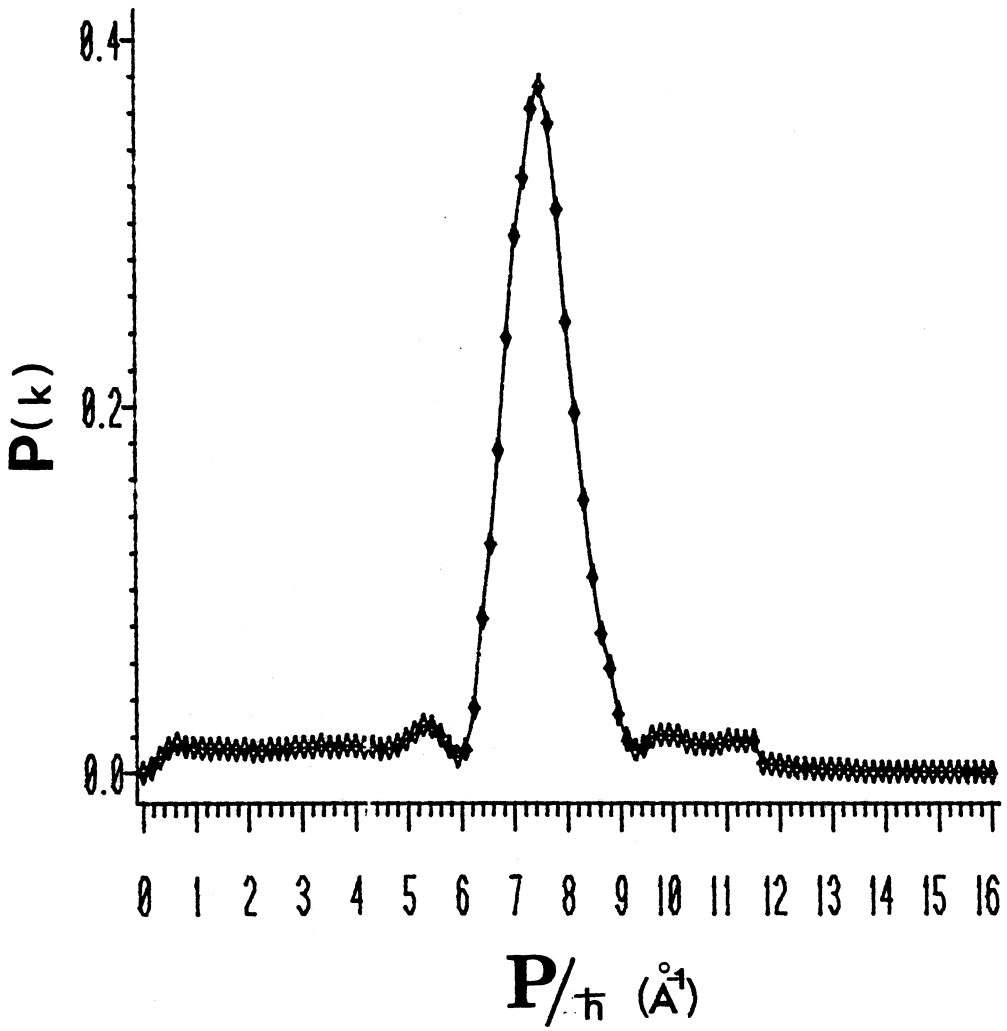

Figure 52. Momentum Distribution for $\Theta_i = 0°$, $\langle E_i \rangle = .0232$ eV, $T_S = 1500$ K, and Time Step 4375.

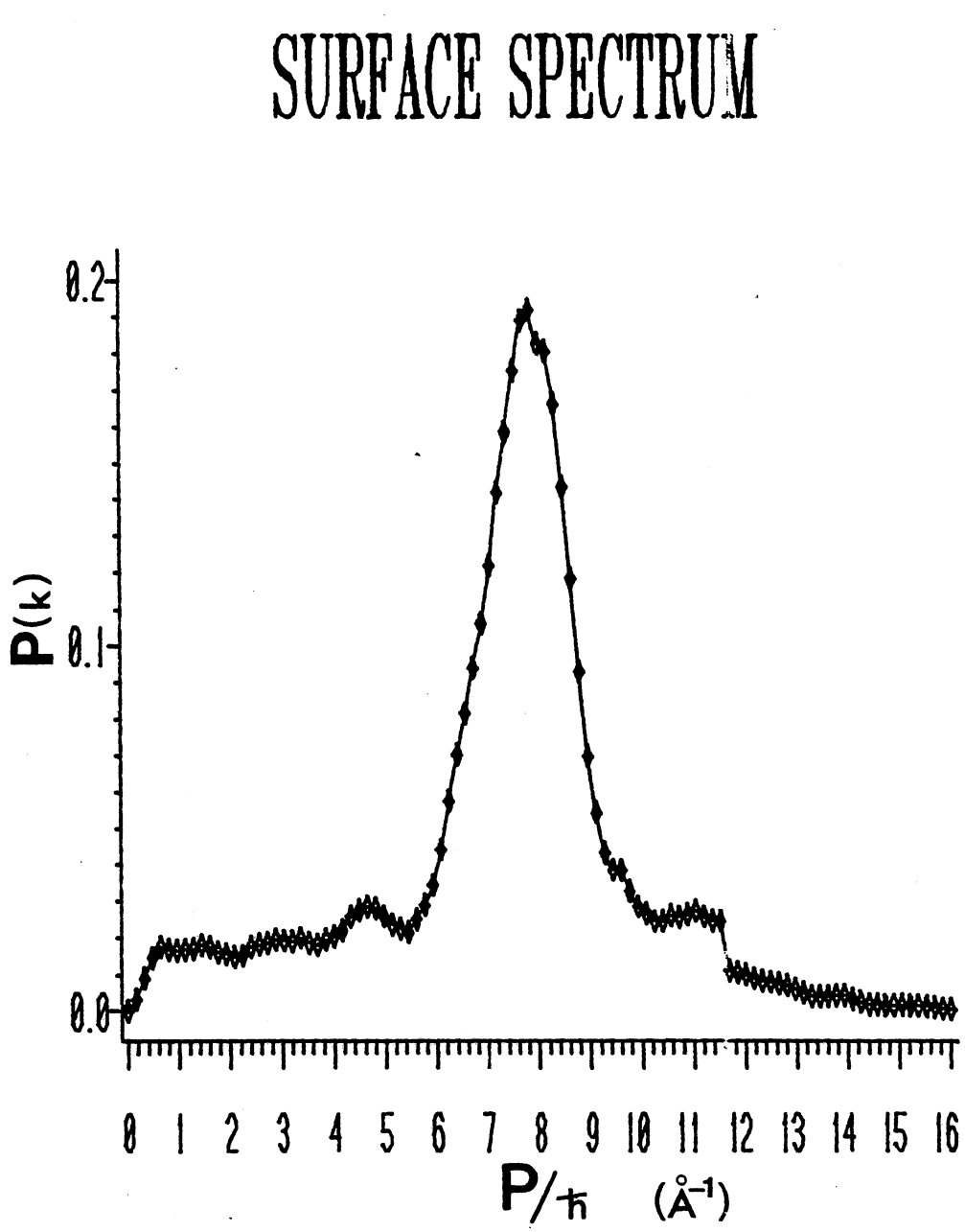

Figure 53. Momentum Distribution for $\Theta_i = 0°$, $\langle E_i \rangle = .0232$ eV, $T_S = 300$ K, and Time Step 4375.

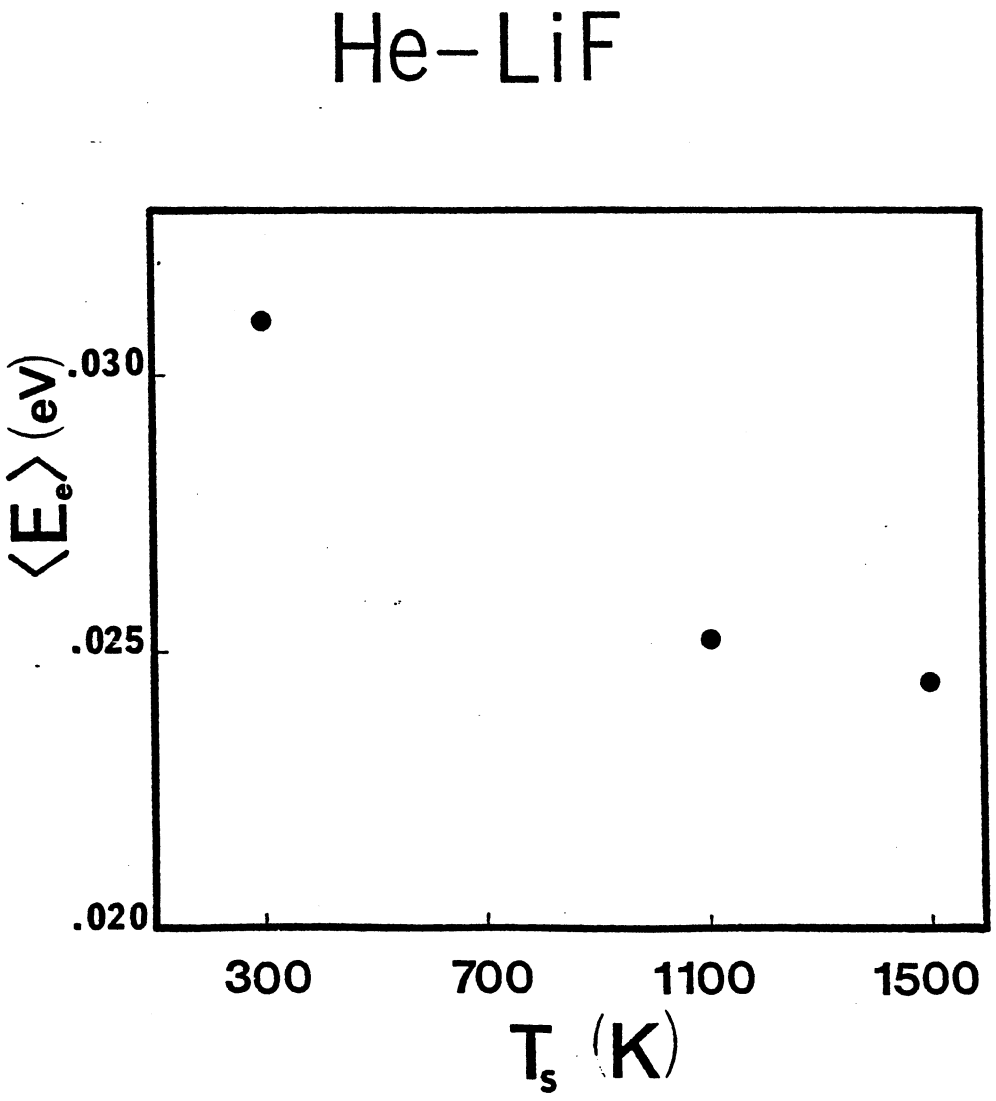

Figure 54. Variation of $\langle E_e \rangle$ with T_s for $\Theta_i = 0°$.

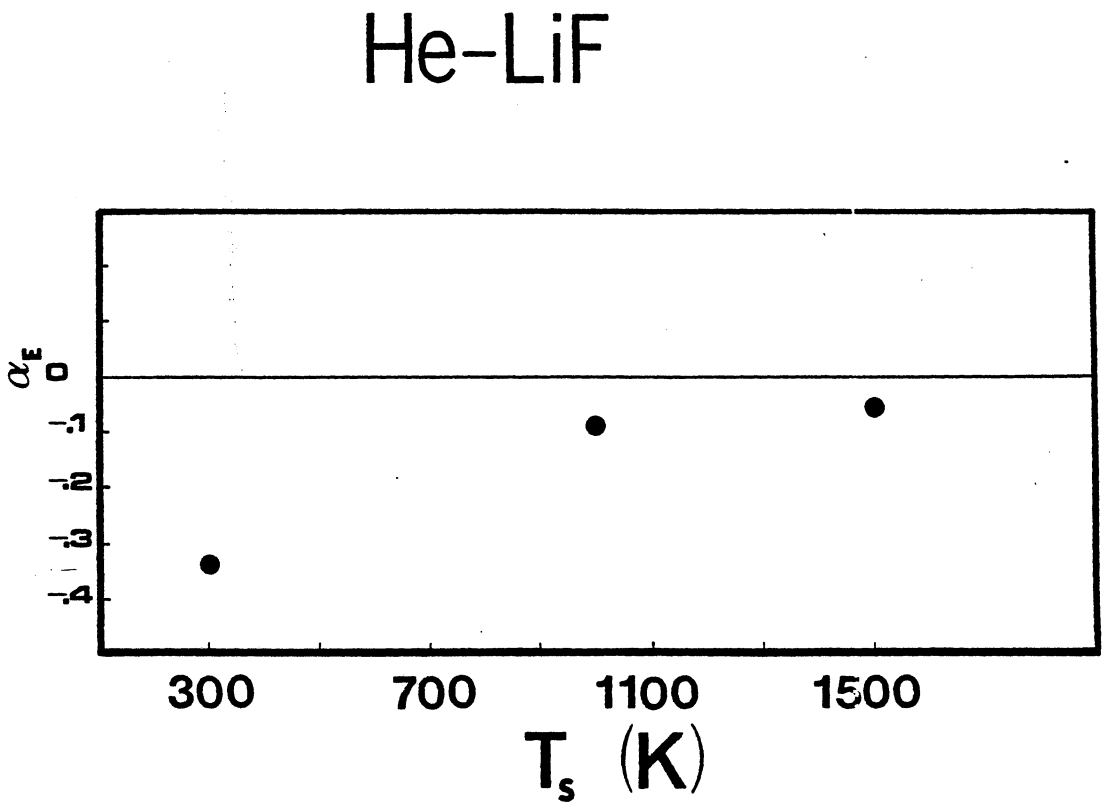

Figure 55. Variation in α_E with T_S for $\theta_i = 0°$.

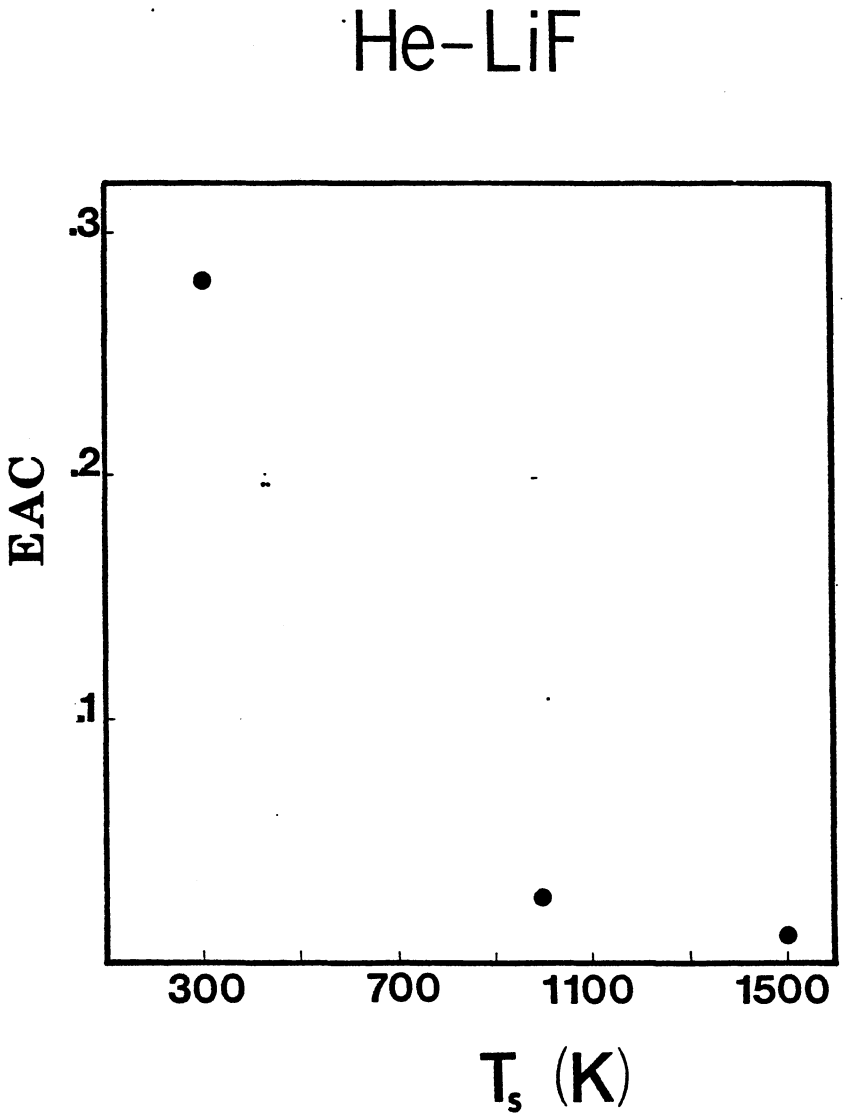

Figure 56. Variation in EAC with T_S for $\Theta_i = 0°$.

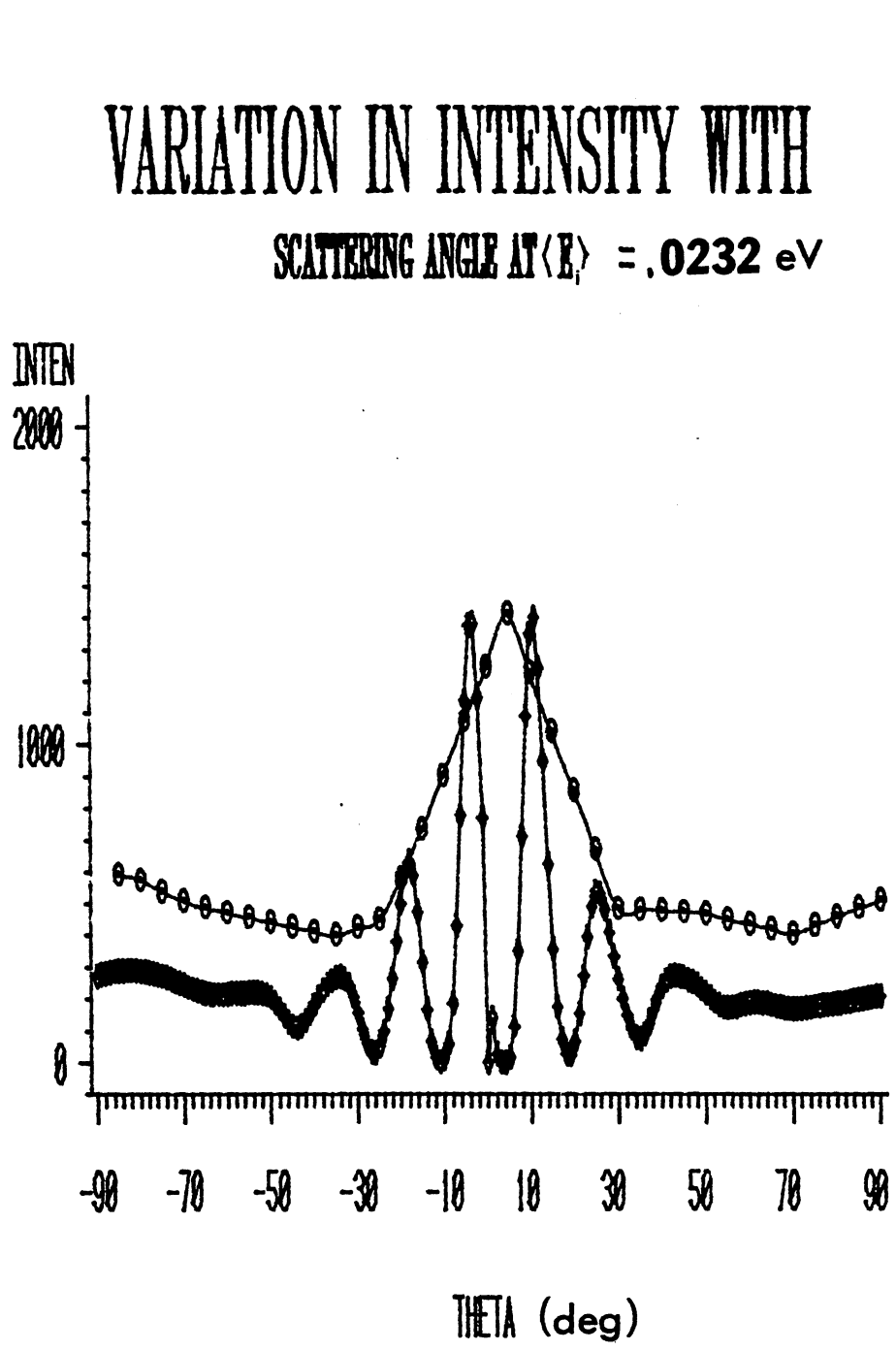

Figure 57. Variation of Scattered Intensity with Scattered Angle for $\Theta = C^{\circ}$, and T_S = 300 K.

CHAPTER V

CONCLUSIONS

A. Summary of Model Results

The phenomena occurring at a gas-surface interface have been studied with a semiclassical 3D model. The crystal lattice was assumed to consist of nine movable lattice sites. In a model case, the lattice was assumed to have masses of 20 amu while the incident gas atom was assumed to have a mass of 1 amu. The lattice sites were assumed to be subject to harmonic potentials, as if springs connected the adjacent sites. In an applied case, the lattice was assumed to be that of a face of a LiF crystal and the incident gas atom was assumed to be a He atom. Lennard-Jones potentials were assumed to exist between the incident gas atom and the lattice sites.

The motion of the lattice atoms was determined from the classical equations of motion. The incident gas atom was assumed to be a wave packet having an almost square distribution in the momentum space parallel to the direction of propagation. The wave packet was evolved through the time-varying potential field set up by the motion of the lattice sites. Energy transfer coefficients, energy accommodation coefficients, angular scattering

distributions, final-state momentum and energy distributions, and Debye-Waller factors were determined. The results for the model were found to be relatively consistent with those of previous totally classical studies (79) and with experimental data (76). In general, the results predicted for the model case are the following:

1. The energy transfer coefficient decreases with increasing surface temperature. From the definition of the energy transfer coefficient, Equation (86), this suggests that the $\langle E_e \rangle$ transferred increases with T_s.

2. The energy transfer coefficient increases with increasing incident angle.

3. The EAC decreases with increasing incident energy. The incident velocity is directly related to the incident energy and provides a measure of the length of time that an incident gas atom will spend in the vicinity of the surface.

4. Final-state momentum distributions broaden with increasing surface temperature. This behavior is in accord with experimental data. Atomic beams scattered from surfaces produce broader peaks for higher surface temperatures. If an incident gas atom spends a larger amount of time close to a surface, it then has more time to accommodate with the surface temperature.

5. Final-state energy distributions predict that energy is transferred when the frequency of the gas-surface interaction matches a two-phonon surface mode. Fourier transformed bond distances show quartets of peaks having

intervals of 81 cm^{-1} corresponding to half the gas-surface interaction frequency.

6. The behavior of the Debye-Waller Factor was found to be in good agreement with experimental trends and with previous calculations (72).

Upon application of the model calculation to the He/LiF system, the predicted results are:

1. The energy transfer coefficient was found to increase with surface temperature. This behavior suggests that $\langle E_e \rangle$ approaches $\langle E_i \rangle$ with increasing surface temperature. Such a trend would mean less energy is transferred for higher surface temperatures. Experimental results (76) do not support such a trend.

2. Predicted angular scattering distributions are qualitatively similar to the experimental data of Boato, Cantini, and Mattera (82).

B. Inadequacies of the Model

The main problem discovered upon employment of the semiclassical 3D model became apparent when the data produced aphysical trends in energy transfer. This anomaly was particularly noticeable in the He/LiF system. The and EAC were predicted to have incorrect behavior with surface temperature. This problem can be rectified by changing the grid spacing from even to odd spacings. As it stands, correct calculations of energy are made very difficult by the fact that a particle possessing wavelength

'λ' cannot be differentiated from one having twice that wavelength. This situation creates havoc in any matters related to the energy due to the energy momentum duality and the De Broglie relationship.

C. Suggestions for Future Work

The overall successes of treatment of gas surface interactions with the 3D semiclassical approach implies that this type of investigation should be continued. Improvements and areas of further work are given as follows:

1. The foremost item is the implementation of an integration scheme in which an unevenly spaced mesh is used. Such a procedure would eliminate problems where incident particles have large masses or relatively large energies. In the treatment of the He/LiF system, the incident energy was decreased in an attempt diminish the inaccuracies incurred when masses are large. This procedure forced an increase in the number of time steps necessary for evolution of the wave packet to and from the surface. If an integration scheme is developed where this effect is removed, then the He/LiF system could be restudied using less computer time, and producing better average energy values. This would allow greater confidence in the calculated energy transfer coefficients, EAC's, etc. Also, any other attempted applications would be accomplished with less computer time.

2. The model can be applied to many experimental

systems having lower surface temperatures. Scattering data has already been obtained for the He/LiF system at T_s = 10 K by Boato, Cantini, and Mattera (82). There are several systems to which the model can be readily applied, with a change in the identity of the surface. For instance, H/LiF and H/graphite could be studied.

3. It is, in principal, possible to determine sticking coefficients. The final-state probability densities are known as a function of time. A criterion could easily be established that would determine the amount of probability density near the surface as a function of time From this data, sticking coefficients could be determined.

4. Many scattering experiments have employed incident beams having a Boltzman distribution. A wave packet having a Boltzman distribution could be easily employed instead of the present square wave packet, and the results compared with those experiments.

5. Eventually, the model must be expanded to consideration of the scattering of diatomic molecules. Such expansion might allow study of vibrationally excited gas molecules incident upon a surface.

BIBLIOGRAPHY

1. H. Y. Wachman, J. Am. Rocket Soc. 32 , 2(1962).

2. K. Moe, AIAA J., 6 , 1375(1968).

3. S. J. Hruska, Conference on Current and Future Problems in High Temperature Chemistry, National Accademy of Sciences, Washington, L967, p.67.

4. K. Toba, Phys. Fluids, 11 , 507(1968).

5. M. Epstein, AIAA J., 6 , 972(1968).

6. J. S. Ward, R. N. Mulford, and R. Kahn, J. Chem. Phys., 47 , 1710(1967).

7. M. J. Cardillo and G. E. Becker, Phys. Rev. Lett. 40 , 1148(1978).

8. M. J. Cardillo and G. E. Becker, Phys. Rev. Lett. 42 , 508(1979).

9. G. Boato, P. Cantini, and R. Colella, Phys. Rev. Lett. 42 , 1635(1979).

10. G. Boato, P. Cantini, and R. Colella, Physica 99B , 59(1980).

11. K. H. Rieder and T. Engel, Phys. Rev. Lett. 43 , 373(1979).

12. G. Derry, D. Wesner, W. Carlos, and D. R. Frankl, Surf. Sci. 87 , 629(1979).

13. G. Boato, P. Cantini, C. Guidi, and R. Tatarek, Phys. Rev. B 20 , 3957(1979).

14. E. Ghio, L. Mattera, C. Slavo, F. Tommasini, and J. Chem. Phys. U. Valbusa, J. Chem. Phys. 73 , 556(1980).

15. J. M. Horne and D. R. Miller, Phys. Rev. Lett. 41 , 511(1978).

16. G. Brusdeylins, R. B. Doak, and J. P. Toennies, Phys. Rev. Lett. 44 , 1417(1980).

17. G. Brusdeylins, R. B. Doak, and J. P. Toennies, Phys. Rev. Lett. 46 , 437(1981).

18. F. O. Goodman and H. Y. Wachman, "Dynamics of Gas-Surface Scattering", Academic Press: New York, (1976), Chapter 3.

19. N. Cabrera, Disc. Faraday Soc. 28 , 16(1959).

20. R. W. Zwanzig, J. Chem. Phys. 32 , 1173(1960).

21. F. O. Goodman, J. Phys. Chem. Solids 23 , 1269(1962).

22. C. M. Chambers and D. T. Kinzer, Surface Sci. 4 , 33(1966).

23. R. A. Oman, A. Bogan, C. H. Weiser, and C. H. Li, AIAA J. 2 ,1722(1964).

24. R. A. Oman, J. Chem. Phys. 48 , 3919(1968).

25. J. D. McClure, J. Chem. Phys. 52 , 2712(1970).

26. R. M. Logan and R. E. Stickney, J. Chem. Phys. 44 , 195(1966).

27. R. M. Logan and R. E. Stickney, J. Chem. Phys. 49 , 860(1968).

28. S. A. Adelman and J. D. Doll, J. Chem. Phys. 61 , 4242(1974).

29. R. Kubo, Rep. Prog. Theor. Phys. 29 , 255(1966).

30. H. Mori, Prog. Theor. Phys. 33 , 423(1965).

31. W. Stelle, Surface Sci. 38 , 1(1973).

32. F. O. Goodman, J. Phys. Chem. Solids 26 , 85(1965).

33. A. G. Stoll, D. L. Smith, and R. P. Merrilly J. Chem. Phys. 54 , 1163(1971).

34. R. M. Logan, J. C. Keck, and R. E. Stickney, "Rarefied Gas Dynamics: (C. L. Brudin, Ed.), p. 47. Academic Press, New York, 1967.

35. R. M. Logan, "Solid State Surface Science" (M. Green, Ed.), Vol. Marcel Dekker, New York, 1967.

36. S. A. Adelman and J. D. Doll, J. Chem. Phys. 64 , 2375(1976).

37. M. Shugard, J. C. Tully, and A. Nitzan, J. Chem. Phys. 66 , 2534(1977).

38. J. E. Lennard-Jones and C. Strachan, Proc. Roy. Soc. A150 , 442(1935).

39. J. M. Jackson, Proc. Camb. Phil. Soc. 28 , 136(1932).

40. C. Zener, Phys. Rev. 40 , 335(1932).

41. C. Zener, Phys. Rev. 40 , 1016(1932).

42. J. M. Jackson and N. F. Mott, Proc. Roy. Soc. A156 , 703(1932).

43. J. M. Jackson and A. Howarth, Proc. Roy. Soc. A142 , 447(1933).

44. A. F. Devonshire, Proc. Roy. Soc. A156 , 37(1933).

45. J. C. Lennard-Jones and A. F. Devonshire, Proc. Roy. Soc. A156 , 29(1936).

46. J. E. Lennard-Jones and A. F. Devonshire, Proc. Roy. Soc. A158 , 253(1937).

47. A. F. Devonshire, Proc. Roy. Soc. A158 , 269(1937).

48. N. Cabrera, V. Celli, F. O. Goodman, and J. R. Manson, Surface Sci. 19 , 67(1970).

49. A. Tsuchida, Surface Sci. 14 , 375(1969).

50. G. Wolken, J. Chem. Phys. 58 , 3047(1973).

51. F. O. Goodman and W. K. Tan, J. Chem. Phys. 59 , 1805(1973).

52. F. O. Goodman, Surface Sci. 30 , 1(1972).

53. R. B. Subbarao and D. R. Miller, J. Vac. Sci. Technol. 9 , 808(1972)

54. F. O. Goodman, J. Chem. Phys. 53 , 2281(1970).

55. J. D. Doll, Chemical Physics 3 , 257(1974).

56. J. D. Doll, J. Chem. Phys. 61 , 954(1974).

57. D. Kumamoto and R. Silbey, J. Chem. Phys. 75 , 5164(1981).

58. R. I. Masel, R. P. Merrill, and W. H. Miller, J. Chem. Phys. 64 , 45(1976).

59. G. Drolshagen and E. J. Heller, Surf. Sci. 139 , 260(1984).

60. R. F. Grote and A. E. Depristo, Surf. Sci. 131 , 491(1983).

61. L. M. Raff and P. M. Agrawal, J. Chem. Phys. 77 , 3946(1982).

62. F. O. Goodman, Critical Reviews in Solid State and Materials Sciences, 7 , 33(1977).

63. M. W. Cole and D. R. Frankl, Surf. Sci. 20 , 585(1978).

64. V. Celli, Proc. of the 12-th Intern. Rarefied Gas Dynamics Conf,. AIAA, 50(1980).

65. H. Hoinkes, Rev. Mod. Phys. 52 , 1933(1980).

66. J. C. Tully, Ann. Rev. Phys. Chem. 31 , 319(1980).

67. M. W. Cole and D. R. Frankl, Rev. Mod. Phys. 53 , 199(1981).

68. M. J. Cardillo, Annual Rev. of Phys. Chem. 32 , 331(1981).

69. "Dynamics of Gas-Surface Scattering", G. Benedek and U. Valbusa (Eds.), Springer-Verlag: Berlin, (1982).

70. A. Askar and A. S. Cakmak, J. Chem. Phys. 68 , 2794(1978).

71. H. Harmuth, J. Math and Phys. 36 , 269(1957).

72. W. H. Weinberg J. Phys. C: Solid St. Phys. 5 , 2098(1972).

73. K. Heinz, K. Muller, T. Engel, K. Rieder, "Stuctural Studies of Surfaces", Springer-Verlag: Berlin, (1982), Chapter 4.

74. A. Ralston, Mathematics of Computation 16 , 431(1962).

75. R. A. Svehla, NASA Tech. Rep. TRR-132 (1962).

76. K. C. Janda, J. E. Hurst, C. A. Becker, J. P. Cowin, D. J. Auerbach, and L. Wharton, J. Chem. Phys. 72 , 2403(1980).

77. J. A. Barker and D. J. Auerbach, Chem. Phys. Lett. 67 , 393(1979).

78. E. K. Grimmelman, J. C. Tully, and M. J. Cardillo, J. Chem. Phys. 72 , 1039(1980).

79. J. Lorenzen and L. M. Raff, J. Chem. Phys. 49 , 1165(1968).

80. D. W. Berreman, Phys. Rev. 130 , 2193(1963).

81. T. Kihara, Advan. Chem. Phys. 1 , 292(1958).

82. G. Boato, P. Cantini, and L. Mattera, Surf. Sci. 55 , 141(1976).

VITA

Charles Bryan Smith

Candidate for the Degree of

Doctor of Philosophy

Thesis: A THEORETICAL INVESTIGATION OF GAS-SURFACE SCATTERING PHENOMENA VIA A SEMICLASSICAL APPROACH

Major Field: Chemistry

Biographical:

Personal Data: Born in Austin, Texas, on April 16, 1953.

Education: Graduated from Canyon High School, in May, 1971; received Bachelor of Science degree in Chemistry from West Texas State University, Canyon, Texas, in August, 1975; received Master of Science degree in Chemistry from Wext Texas State University, Canyon, Texas, in August, 1978; completed requirements fro the Doctor of Philosophy degree at Oklahoma State University, December, 1984.

Professional Experience: Graduate Teaching Assistant, Oklahoma State University, August, 1978-May, 1979; CONOCO Fellow, May, 1979; Graduate Teaching Assistant, 1979-July, 1980; National Science Foundation Research Assistant, August, 1980-July, 1981; Graduate Teaching Assistant, August, 1981-May, 1984; CONOCO Fellow, May, 1984-July, 1984.

Membership in Honorary and Professional Societies: Member of the American chemical Society; member of Phi Lambda Upsilon, Honorary Chemical Society; member of Pi Mu Epsilon, Honorary Mathematics Fraternity; member of Alpha Chi, schoolastics honorary.